CONTRACTOR REPORT

SAND84-8190
UC-62c
Unlimited Release

Analysis and Design of the Volumetric Air Heating Receiver

Pacific Northwest Laboratory
Richland, Washington

Prepared by Sandia National Laboratories, Albuquerque, New Mexico 87185 and Livermore, California 94550 for the United States Department of Energy under Contract DE-AC04-76DP00789.

Printed July 1985

Printed in the United States of America
Available from
National Technical Information Service
5285 Port Royal Road
Springfield, VA 22161

NTIS price codes
Printed copy: A05
Microfiche copy: A01

FOREWORD

The research and development described in this report was conducted within the U.S. Department of Energy's (DOE) Solar Thermal Technology Program. The Solar Thermal Technology Program directs efforts to advance solar thermal technologies through research and development of solar thermal materials, components, and subsystems, and through testing and evaluation of solar thermal systems. These efforts are carried out through DOE and its network of national laboratories who work with private industry. Together they have established a goal-directed program for providing technically proven and economically competitve options for incorporation into the Nation's energy supply.

There are two primary solar thermal technologies: central receivers and distributed receivers. These two technologies use various point and line-focus optics to concentrate sunlight onto receivers where the solar energy is absorbed as heat and converted to electricity or used as process heat. In central receiver systems, which this report considers, fields of heliostats (two-axis tracking mirrors) focus sunlight onto a single receiver mounted on a tower. The radiant energy is absorbed by a working fluid circulating within the receiver and is transformed into high temperature thermal energy. Temperatures in central receivers may exceed $1500^{o}C$.

SUMMARY

Under the sponsorship of Sandia National Laboratories, Livermore, the Pacific Northwest Laboratory (PNL) performed an analysis and preconceptual design of the Volumetric Air Heating Receiver (VAHR), a concept for producing high-temperature air for process heat applications. Previous studies showed that the VAHR concept had potential as a high-efficiency, low-cost receiver for high-temperature operations. However, since the analyses in these past studies were preliminary, the VAHR needed further development and analysis before a detailed evaluation of the feasibility of the concept could be made.

To this end, several models were developed to simulate the thermal processes occurring in the VAHR. Two models, both using the Monte Carlo technique, were developed to simulate the complex radiation heat transfer in the receiver. One model calculates the distribution of energy from the heliostat field absorbed in the receiver. The other calculates exchange factors to allow yet a different model to simulate radiation exchange within the receiver. Models were also developed to analyze the complex air flow through the receiver, to calculate velocities for evaluating convective heat transfer coefficients, and to determine the air flow distribution and pressure drop. Finally, a thermal performance model was developed to tie the various processes together and estimate the thermal performance of the receiver.

These models were applied in several studies aimed at developing a simple, high-efficiency receiver design. The studies centered around three main aspects of the VAHR: 1) selecting an absorbing array; 2) enhancing convective heat transfer; and 3) geometrically reducing reflection and reradiation losses. In the absorbing array study, we looked at two fin designs and one fiber design. Both fin designs, the original staggered fin concept and the radial fin concept, developed into extremely large receivers. Each required an open arrangement and had characteristically low heat transfer coefficients. The fiber design, using 0.6-mm ceramic fibers, demonstrated better heat transfer and optical characteristics than the fin designs, but it also resulted in a large receiver. Of the three absorbing array designs, the fiber array was the preferred.

In an attempt to reduce the receiver size, we analyzed two methods of enhancing convective heat transfer. One method called for rotating the fiber absorbing array to increase the relative velocity between the fibers and the air. The other relied on inducing a swirl in the air at the receiver perimeter and allowing conservation of angular momentum to increase the air rotational velocity as the air moves into the receiver. This method would also increase the relative velocity between the fibers and the air. While the study showed that both methods performed comparably, we felt that the "preswirl" technique possibly offered fewer technical obstacles.

To reduce thermal losses from the receiver due to reflection and reradiation, two techniques were evaluated. The original concept was to use a "light-valve," a row of reflecting wedges aligned around the perimeter to allow solar energy to penetrate the receiver while preventing radiant energy from leaving the receiver. An in-depth analysis proved this technique to be infeasible. Because the wedges absorbed a significant amount of energy and the heat transfer coefficients were very low, they operated at temperatures at or above their material limits. Without any safety factor, the receiver integrity could not be assured if there were maldistribution of airflow or insolation. The second technique considered for reducing geometric losses was the use of a cavity-type shroud, where the absorbing core is housed in a "protective" shell. This method was effective in reducing losses.

From these studies a final preconceptual VAHR design was developed, consisting of an array of absorbing ceramic fibers, a row of slotted pipes arranged along the perimeter to induce the air swirl, and a shroud to house the core. Performance and cost estimates showed that this design operated with a receiver efficiency of 82% at a capital cost of $6.1 M. A levelized energy cost for a process heat application was estimated to be on the order of $29/MBtu.

During the course of our work, we identified several major areas of uncertainty that impact the attractiveness of the VAHR concept. These areas center around fiber integrity, preswirl generation, and the shroud performance. The ceramic fibers in this design are subjected to a harsh environment. Without an experimental evaluation of the fiber's mechanical and thermal

properties under such conditions, their survivability is in question. For the preswirl generation, the primary question pertains to the performance of the technique. Since the theory of slotted jets in series does not exist, only a cursory analysis with many simplifying assumptions was made. One critical assumption is that a uniform preswirl velocity can be induced. While our original concept consisted of slotted pipes uniformly spaced around the receiver's perimeter, our experience with the reflecting rows suggested that the pipes should be placed in areas blocked from the direct flux. Such a placement would not be uniform, and might affect the ability to generate a uniform preswirl. A significant experimental effort would be required to adequately assess the feasibility of this enhancement technique. Finally, tools were not available to adequately address the complete performance of the shroud design. We did not have the capability to predict spillage or convection losses, and we did not rigorously evaluate the distribution of absorbed insolation. As a result of these latter factors, the overall performance estimate of the VAHR contains a significant degree of uncertainty.

Through the design evolution of the VAHR, several qualitative advantages that at one time made the concept very attractive were lost. What was once a compact, simple receiver with passive operation is now a much larger, more complicated design that relies on active operation to provide convective enhancement. Furthermore, a receiver that once was predicted to have a thermal efficiency of 97.3% (including convection losses) is now predicted to have an efficiency of 82% (neglecting convection losses). These qualitative aspects, plus the major uncertainties discussed above, cast a shadow over the attractiveness of the VAHR concept. Any further work on the concept will require a major new initiative to address the remaining technical issues that currently cloud the VAHR feasibility. PNL feels that the probability of success in resolving these issues with such an initiative is low, and therefore recommends that the VAHR project be discontinued.

CONTENTS

SUMMARY iii

NOMENCLATURE xiii

ACKNOWLEDGMENTS xviii

1.0 INTRODUCTION 1.1

1.1 CONCEPT DESCRIPTION 1.2

1.2 PREVIOUS STUDIES 1.4

1.3 PROJECT OBJECTIVES AND SCOPE 1.6

2.0 CONCLUSIONS AND RECOMMENDATION 2.1

3.0 DESIGN EVOLUTION 3.1

3.1 STAGE 1 - ABSORBING ARRAY 3.1

3.2 STAGE 2 - AUGMENTING CONVECTIVE HEAT TRANSFER 3.4

3.3 STAGE 3 - GEOMETRIC LOSS REDUCER 3.5

4.0 VOLUMETRIC RECEIVER THERMAL PROCESSES 4.1

4.1 RADIATION HEAT TRANSFER 4.1

4.1.1 Properties of Insolation 4.1

4.1.2 Insolation Absorption 4.5

4.1.3 Internal Radiation Heat Transfer 4.6

4.2 AIR FLOW 4.6

4.3 CONVECTIVE HEAT TRANSFER 4.8

4.4 RECEIVER THERMAL PERFORMANCE MODELING 4.9

5.0 RADIATION HEAT TRANSFER MODELING 5.1

5.1 SELECTION OF MODELING APPROACH 5.1

5.1.1 Problem 5.2

5.1.2 Applicability of Analysis Methods to the VAHR 5.2

5.2 MONTE CARLO MODELING..... 5.4
5.3 EXCHANGE FACTOR CALCULATION..... 5.6
5.4 INSOLATION DISTRIBUTION CALCULATION..... 5.8
5.5 MODEL VERIFICATION..... 5.8
5.6 SAMPLE SIZE CONSIDERATIONS..... 5.11
6.0 AIR FLOW MODELING..... 6.1
6.1 MANIFOLD ORIFICING AND RECEIVER PRESSURE DROP..... 6.1
6.1.1 Orifice Distribution Calculation Method..... 6.1
6.1.2 Air Flow Distribution TEMPEST Model..... 6.3
6.2 TANGENTIAL AIR FLOW ANALYSIS..... 6.7
6.3 RECEIVER CONVECTIVE LOSS..... 6.10
7.0 CONVECTIVE HEAT TRANSFER MODELING..... 7.1
7.1 CONVECTIVE HEAT TRANSFER FROM FIN SURFACES..... 7.1
7.1.1 Forced Convection Heat Transfer..... 7.2
7.1.2 Natural Convection..... 7.3
7.1.3 Mixed-Mode Heat Transfer..... 7.4
7.2 ENHANCED HEAT TRANSFER FROM FINS..... 7.4
7.3 CONVECTIVE HEAT TRANSFER FROM CYLINDERS..... 7.6
7.3.1 Forced Convective Heat Transfer..... 7.6
7.3.2 Natural Convection..... 7.7
7.3.3 Combined Forced and Natural Convection..... 7.7
8.0 THERMAL PERFORMANCE MODELING..... 8.1
8.1 RECEIVER ARRANGEMENT AND ASSUMPTIONS..... 8.1
8.2 GENERAL APPROACH..... 8.3
8.3 TRANSIENT MODEL..... 8.4
8.4 RADIATION HEAT TRANSFER..... 8.6

8.4.1 Definition of Exchange Factor..... 8.6
8.4.2 Exchange Factor Processing..... 8.7
8.4.3 Calculation of Radiation Heat Transfer..... 8.8
8.5 CONVECTIVE HEAT TRANSFER AND DRAG..... 8.9
8.5.1 Relative Velocity..... 8.9
8.5.2 Convective Heat Transfer From Fins..... 8.10
8.3.3 Convective Heat Transfer From Fibers..... 8.10
8.5.4 Drag..... 8.11
8.6 SHROUD MODEL..... 8.12
8.7 RESULTS OF THE PERFORMANCE MODEL..... 8.17
8.8 VERIFICATION..... 8.18
9.0 VOLUMETRIC RECEIVER DESIGN STUDIES..... 9.1
9.1 GROUND RULES AND ASSUMPTIONS..... 9.1
9.2 ABSORBING ARRAY SELECTION..... 9.2
9.2.1 Staggered Fin Array..... 9.3
9.2.2 Radial Fin Array..... 9.6
9.2.3 Fiber Array..... 9.10
9.3 CONVECTIVE HEAT TRANSFER ENHANCEMENT..... 9.14
9.3.1 Rotating Fiber Array..... 9.14
9.3.2 Preswirl..... 9.16
9.3.3 Comparison of Thermal Performances..... 9.17
9.4 GEMEOTRIC LOSS REDUCER..... 9.19
9.4.1 Reflecting Row..... 9.19
9.4.2 Shroud..... 9.31
9.5 FINAL VAHR DESIGN..... 9.44
9.6 PROBLEMS AND UNCERTAINTIES WITH THE VAHR..... 9.46

10.0 TRANSPORT SYSTEM DESIGN..... 10.1

10.1 DOWNCOMER..... 10.5

10.2 AIR-TO-AIR HEAT EXCHANGER..... 10.6

10.3 AIR MOVER..... 10.8

11.0 COST ANALYSIS..... 11.1

11.1 RECEIVER COSTS..... 11.1

11.2 BALANCE-OF-SYSTEM COSTS..... 11.8

11.3 SYSTEM ECONOMICS..... 11.11

12.0 REFERENCES..... 12.1

APPENDIX - DETAILS OF THE MONTE CARLO MODEL..... A.1

FIGURES

1.1	Central Receiver Concept - Example	1.1
1.2	Original Conception of the Volumetric Receiver	1.2
1.3	Schematic of Generic Volumetric Air Heating Receiver	1.4
3.1	Volumetric Receiver Designs Considered	3.2
3.2	Conceptual Sketch of a Shrouded Volumetric Receiver	3.6
4.1	Incident Angle and Heliostat Image Size for a Hypothetical 50-MWt Field	4.3
4.2	Impact of Incident Angle Distribution	4.4
5.1	Enclosure Used for Comparison with Analytical Results	5.9
5.2	Comparison with Experimental Results--Transmission Through First Reflecting Zone	5.11
5.3	Comparison with Experimental Results--Transmission Through First and Second Reflecting Zones	5.12
6.1	Volumetric Receiver Air Flow Distribution - TEMPEST Model	6.4
6.2	Volumetric Receiver Convective Loss - TEMPEST Model	6.12
8.1	Receiver Zone Arrangement	8.2
8.2	Schematic of Shroud Layout	8.13
8.3	Schematic of Shroud with Aperture Blocking	8.15
8.4	Shroud with Fiber Fill	8.16
9.1	Plan View of the Rotating Fiber Volumetric Receiver	9.15
9.2	Velocity Profiles for Rotating Fiber Receiver	9.16
9.3	Plan View of Preswirl Volumetric Receiver	9.17
9.4	Velocity Profiles for Preswirl Receiver	9.18
9.5	Distribution of Air Relative Velocity and Insolation Absorption	9.20
9.6	Parameters Which Characterize a Reflecting Row Zone	9.23

9.7 Impact of the Number of Reflecting Zones on Reflecting Zone Performance..... 9.25

9.8 Influence of Aspect Ratio and Wedge Angle on Reflecting Zone Performance..... 9.26

9.9 Impact of Cell Width on Reflecting Zone Performance..... 9.27

9.10 Details of the Shroud Design..... 9.35

9.11 Temperature Distributions for the Base Case Shrouded Fiber Design..... 9.37

9.12 Shroud With Packing..... 9.40

9.13 Shroud With Aperture Blocking..... 9.41

10.1 Transport System With Checker Stove and Two Air Movers..... 10.2

10.2 Transport System With Checker Stove, Intercooler, and One Air Mover..... 10.3

10.3 Transport System With Recuperator and Two Air Movers..... 10.4

A.1 Receiver Geometric Arrangement and Definition of Cell Parameters..... A.2

A.2 Monte Carlo Model for Calculating Incident Radiation Absorption..... A.3

A.3 Monte Carlo Model for Calculating Exchange Factors..... A.3

A.4 Cell Angle Definitions..... A.6

TABLES

5.1	Analytical Results Versus VORRUM Prediction.....	5.10
7.1	Summary of Enhancement Techniques for Fin Designs.....	7.5
8.1	Material Properties.....	8.3
8.2	Impact of Shroud Emissivity on Receiver Performance.....	8.14
9.1	Staggered Fin Base Case Design.....	9.4
9.2	Staggered Fin Base Case Design Performance.....	9.5
9.3	Staggered Fin Array Sensitivity Study Results.....	9.6
9.4	Insolation Distribution for the Radial Fin Array.....	9.7
9.5	Radial Fin Base Case Design.....	9.9
9.6	Radial Fin Base Case Performance.....	9.10
9.7	Radial Fin Sensitivity Study Results.....	9.11
9.8	Base Case Fiber Design Characteristics.....	9.12
9.9	Fiber Array Design Performance Results.....	9.13
9.10	Results of Fiber Array Sensitivity Studies.....	9.14
9.11	Impact of Augmentation Technique on Thermal Performance.....	9.19
9.12	Reflecting Row Fiber Design Characteristics.....	9.29
9.13	Reflecting Row Fiber Design Performance Results.....	9.30
9.14	Reflecting Row Fiber Design Sensitivity Study Results.....	9.30
9.15	Core Designs With 2.5-Meter Radius.....	9.31
9.16	Core Designs With 3.75-Meter Radius.....	9.32
9.17	Core Designs With 5.0-Meter Radius.....	9.32
9.18	Shrouded Fiber Design Characteristics.....	9.34
9.19	Shrouded Fiber Design Performance Results.....	9.36
9.20	Swirl Velocity Sensitivity Study Results.....	9.38

9.21 Fiber Diameter Sensitivity Study Results..... 9.38
9.22 Impact of Fiber Packing on Receiver Performance..... 9.40
9.23 Impact of Aperture Blocking..... 9.42
9.24 Impact of Shroud Spacing..... 9.42
9.25 Impact of Product Temperature..... 9.43
9.26 Impact of Aperture Blocking and Core Radius..... 9.44
9.27 Thermal Performance of the 50-MWt VAHR Producing Air at 1367 K... 9.45
10.1 Downcomer Design and Thermal Performance..... 10.6
10.2 Checker Stove Design Conditions..... 10.7
10.3 Checker Stove Design..... 10.7
10.4 Transport System Pressure Loss..... 10.9
10.5 Fan Design and Performance Specifications..... 10.9
11.1 Volumetric Receiver Components..... 11.3
11.2 Fabrication, Assembly, and Installation Activities..... 11.4
11.3 Receiver Material and Labor Unit Costs..... 11.5
11.4 Volumetric Receiver Design Dimensions..... 11.6
11.5 Shrouded Preswirl Base Case Receiver Costs..... 11.7
11.6 Shrouded Preswirl Receiver Costs with Shroud Packing..... 11.8
11.7 Volumetric Receiver Downcomer Cost..... 11.9
11.8 Transport System Fan Costs..... 11.10
11.9 Volumetric Receiver System Capital Cost..... 11.11
11.10 Principal Economic Assumptions..... 11.12
11.11 System Capital and Levelized Energy Costs..... 11.13

NOMENCLATURE

ENGLISH SYMBOLS

a	total orifice area per unit length of manifold
A	area
A_f	cross sectional area of individual fiber
A_p	projected area
B	exchange factor
c	orifice coefficient for circular hole
C_p	constant pressure specific heat
C_D	fiber drag coefficient
D	manifold diameter
DF	drag factor
$\bar{f}$	fraction of total manifold surface area open to flow
F	view factor or exchange factor
g	gravitational constant
Gr	Grashof number
h	convective heat transfer coefficient
h_{fc}, h_f	forced convection heat transfer coefficient
h_{nc}, h_n	natural convection heat transfer coefficient
h_{mix}, h_m	mixed convection heat transfer coefficient
k	thermal conductivity
K	irreversible loss coefficient
L	manifold length
$\dot{m}$	air mass flow through manifold per unit length
N_f	number of fibers per zone
N_i	number of photons emitted by surface i
N_{i-j}	number of photons leaving surface i and arriving at surface j
NBATC	number of photon batches
NICRM	number of increments in an emitting surface
NPHOT	number of photons in a photon batch
Nu	Nusselt number

P	air dynamic pressure, power
P_{atm}	atmospheric pressure
Pr	Prandtl number
Q_i	net energy from zone i
Q_{ins}	rate of energy incident on a receiver surface
r	radial coordinate direction, radius of zone i
r, R	receiver radius
R	random number
Ra	Raleigh number
Re	Reynolds number
T	temperature
T_a	air temperature
$T\infty$	ambient temperature
T_{air}, T_{bulk}	bulk air temperature adjacent to wedge
T_{surf}, T_{zone}	surface temperature of plate or fiber
U	radial component of air velocity
V	free stream air inflow velocity
V_θ	tangential velocity
V_f	fiber tangential velocity
V_r	radial velocity
V_{rel}	relative velocity between fibers and air
V_t	tangential component of air velocity
V_z	volume of zone
w	air mass flow along downcomer
$\dot{\omega}$	rotation speed
w_f	angular velocity of fiber rotation
w_t	total receiver air mass flow rate
x	coordinate direction of manifold axis
y	vertical distance

GREEK SYMBOLS

α	incident angle of insolation striking receiver surface, emission angle
α_λ	specular absorptivity
β_r	maximum emission angle which allows photon to strike the right cell boundary
β_L	maximum emission angle which allows photon to strike the opposite cell boundary
Δ	incident angle of cell photon interaction
ΔV	relative tangential velocity between fibers and air
ϵ	emissivity
ϵ_λ	specular emissivity
μ	dynamic viscosity
υ	kinematic viscosity
ρ_λ	specular reflectivity
ρ	air density
σ	Stefan-Boltzmann constant
σ_α	standard deviation of incident angle
σ_{image}	standard deviation of image
Θ	cell boundary wedge half angle

SUBSCRIPTS

i	parameter for zone i
i-j	interaction from zone i to zone j
F	forced convection
fr	free convection
H	based on height
L	based on length
T	total quantity

ACKNOWLEDGMENTS

This work was supported by Sandia National Laboratories as part of the U.S. Department of Energy's Solar Thermal Central Receiver Program. The authors would like to acknowledge the guidance provided by J. Wright, W. Wilson, and W. Delameter of Sandia. Appreciation is also extended to S. Hauser, R. Skarda, K. Nomura, S. Montgomery, and M. K. Willis of PNL, and J. Welty of Oregon State University for their assistance in this work. Finally, the authors wish to thank S. Matsumoto and the graphics and word processing crews at PNL for assisting in the preparation of this final report.

1.0 INTRODUCTION

This report documents the results of an analysis and design of the Volumetric Air Heating Receiver (VAHR) for use in a solar central receiver facility. In such a facility, energy from the sun is concentrated and focused by a field of mirrors (heliostats) to a central point. At this central point lies a tower-mounted receiver, which absorbs the solar energy from the field and transfers it to a heat transfer "fluid". This heated fluid is then transported to ground level where it provides energy for power generation or process heat use. A drawing of a central receiver system is shown in Figure 1.1.

Preliminary analysis of the Volumetric Air Heating Receiver (VAHR) showed that the VAHR concept held promise as a low-cost, high-efficiency receiver, especially at high temperatures. In the interest of obtaining a detailed evaluation of the feasibility of the VAHR concept, Sandia National Laboratories, Livermore (SNLL) funded the Pacific Northwest Laboratory (PNL) to further develop the receiver and evaluate the feasibility of the VAHR concept in an industrial process heat application. The results of this effort are described here. Before delving into the results, we briefly describe the features of the VAHR concept, review previous studies dealing with the VAHR, and outline the objectives and scope of the project.

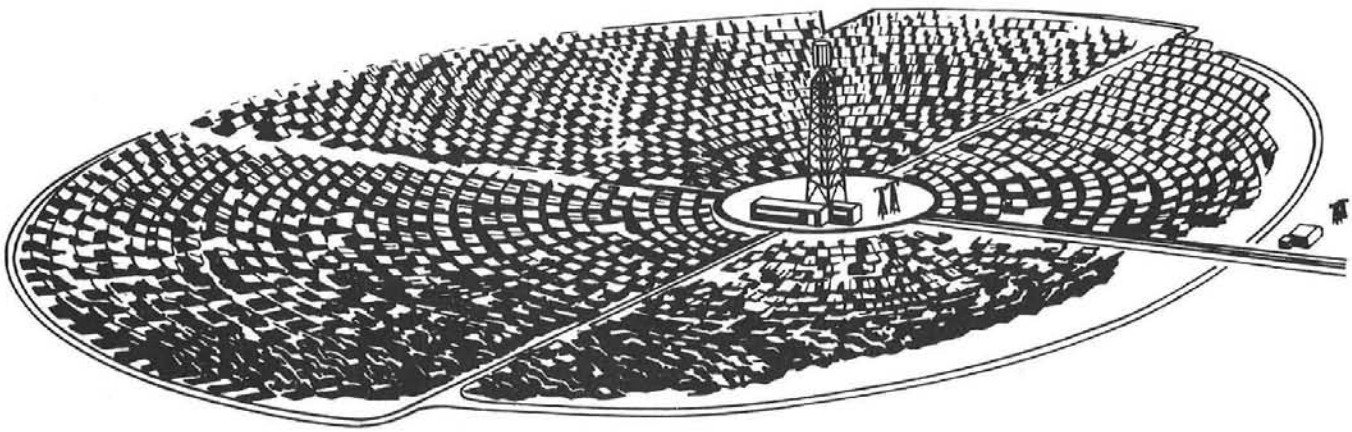

FIGURE 1.1. Central Receiver Concept - Example

1.1 CONCEPT DESCRIPTION

As originally conceived, the volumetric receiver consisted of an array of absorbing and reflecting surfaces arranged in concentric cylindrical rows around a manifold (Figure 1.2). The reflecting surfaces are wedge-shaped fins and form the outer row of the receiver. Solar energy striking the receiver is reflected into the interior of the receiver where it is absorbed on an array of pins. This energy is removed from the pins by convection as air is drawn through the array using an induced draft fan. After passing through the array, the high-temperature air enters the downcomer and is drawn to the bottom of the tower.

High performance projected for the VAHR was envisioned to be the result of the three inherent features of the volumetric concept:

- Volumetric Absorption - Solar energy from the heliostat field is absorbed throughout the volume occupied by the array.

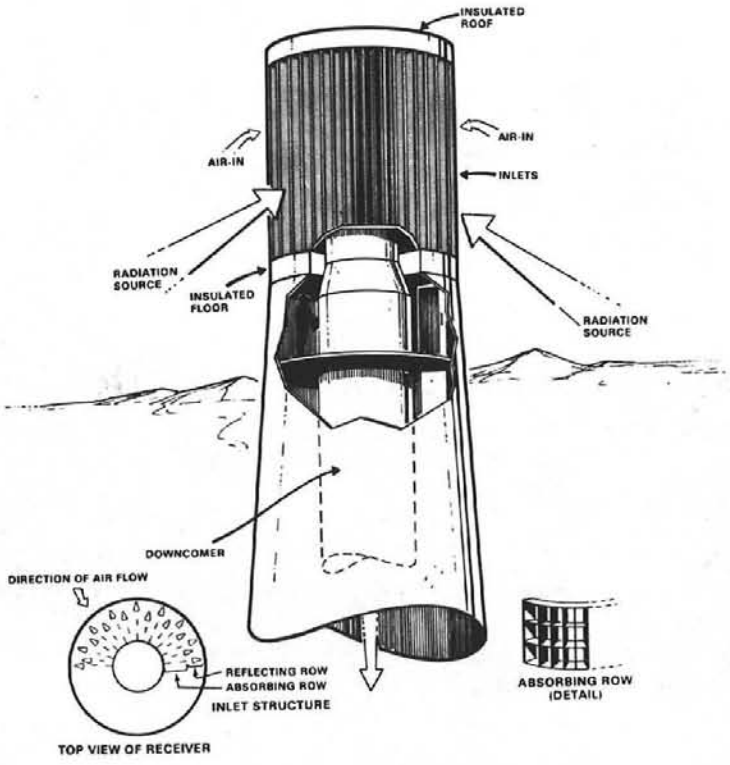

FIGURE 1.2. Original Conception of the Volumetric Receiver

- Reflecting Rows - Wedge-shaped fins with specularly reflecting surfaces act as a "light valve," allowing solar energy to enter the receiver but inhibiting thermal radiation and reflection from leaving the receiver.
- Heating Ambient Air - Ambient air is drawn through the array, leaving the outer most surfaces relatively cool and allowing the interior absorbing surfaces to reach the highest temperature.

These unique features enhance performance by inhibiting convection, reflection, and reradiation losses from the receiver.

Although modifications of the original concept have been made and are reported here, all volumetric receiver designs considered contain the following generic characteristics:

- Volumetric Absorbing Array - The volumetric absorbing array is the primary absorber in the receiver. The array is intended to absorb insolation and transfer the thermal energy to the air being drawn past the surfaces of the array with a minimum of pressure drop and reradiation losses. The absorbing array can consist of fin-shaped pins or small fibers arranged in a variety of configurations.
- Inlet Manifold/Terminal Absorber - The inlet manifold serves two purposes. First, it is designed to evenly distribute air flow (axially) through the receiver. Second, the inlet manifold also acts as the terminal absorber which absorbs any insolation that has passed through the volumetric absorbing array. The inlet manifold is located inside of the absorbing array.
- Geometric Loss Reducer - The reflection and reradiation losses from the absorbing array can be further reduced using a geometric loss reducer. The geometric loss reducer lets insolation enter the receiver while inhibiting the reradiation or reflection of energy from the receiver. This effect is obtained solely by the geometric arrangements of surfaces rather than any specific surface coating or

cover glass. One common geometric loss reducer is a cavity around the absorber. A second type considered in this study is a row of wedge-shaped reflecting pins as the external row in the receiver.

- Downcomer - The downcomer is the pipe or duct through which the hot air travels as it is drawn to ground level by an induced draft fan.

The arrangement of the primary components of the volumetric receiver is shown schematically in Figure 1.3.

1.2 PREVIOUS STUDIES

The Volumetric Air Heating Receiver was invented at the Pacific Northwest Laboratory (PNL), and the U.S. Department of Energy (DOE) holds the patent on the concept (U.S. Patent No. 4,394,859). The original evaluation of the volumetric receiver consisted of a brief internal review conducted at PNL. The results of this evaluation are documented by Drost and Eyler (1981). Based on these results, the VAHR was included in a comparison study with six other high-temperature air heating receivers (Bird et al. 1982). The results of the receiver comparisons were used by Sandia National Laboratories, Livermore in a

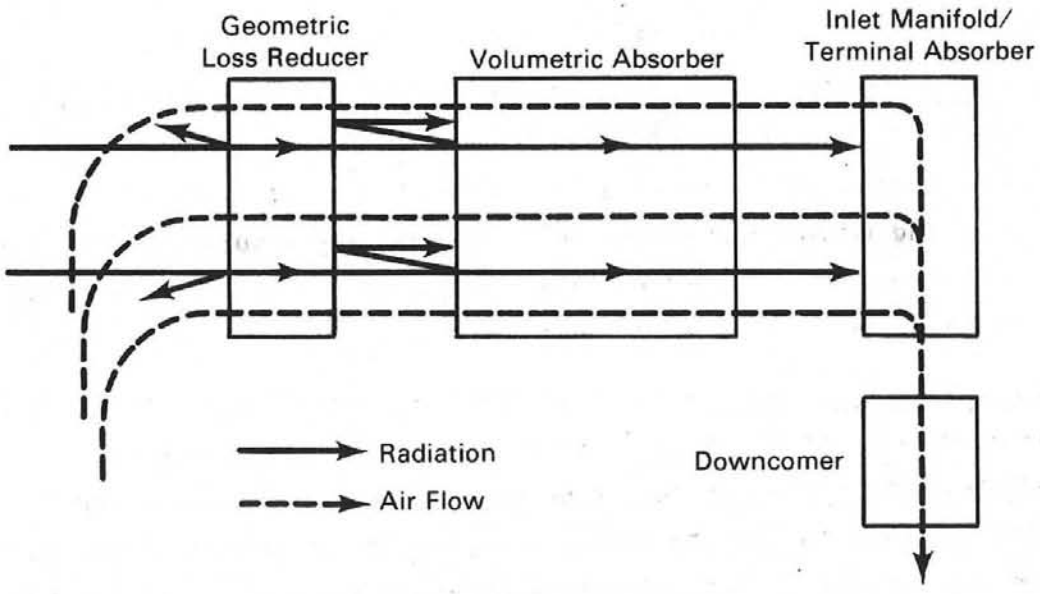

FIGURE 1.3. Schematic of Generic Volumetric Air Heating Receiver

cost and performance comparison of complete systems using the seven receivers studied by Bird et al. The results of this study are documented by De Laquil et al. (1983). These three studies are summarized below.

Preliminary evaluations of the VAHR at PNL involved developing a simple performance model for the receiver and then predicting receiver performance. The receiver was modeled as a series of concentric cylindrical zones. The insolation absorbed in each zone was calculated by modeling each zone as a semi-transparent material with a composite absorptivity, emissivity, and transmissivity. Using a method suggested by Viskanta et al. (1978), the distribution of absorbed insolation was determined. The equilibrium temperature distribution was calculated with no allowance for internal radiation heat transfer between zones. With the temperature distribution and view factors calculated for infinite concentric cylinders, it was possible to determine the reradiation losses. The results of the evaluations were extremely favorable, with projected receiver efficiencies above 95% for a receiver producing hot air at 1093°C. However, the report describing these results (Drost and Eyler 1981) indicated that many aspects of the receiver needed further analysis to verify the many simplifying assumptions made during the course of the preliminary evaluations. Air flow distribution, pin-to-air heat transfer, reflecting zone performance, distribution of absorbed energy, and impact of heliostat field characteristics were the more important aspects needing further analysis.

The air heating receiver comparison documented by Bird et al. (1982) consisted of developing preconceptual designs for seven advanced air heating receivers, including the VAHR. Designs were developed for a range of facility sizes, product air temperatures, and pressures. The performance and cost of each receiver design was estimated, and areas of technical concern were identified. The analytical model used to evaluate the VAHR in this study was essentially the same as that used in the preliminary evaluations. The main differences were in the correlations used in calculating the convective heat transfer coefficients between the pins and the air and in estimating convective losses from the entire receiver to the surroundings. The areas of technical uncertainty were expanded to include new problems identified during the study.

The results of this evaluation showed that the volumetric receiver would have excellent thermal performance, but that the receiver was more expensive than several other designs.

The scope of the comparison described above was limited to the receiver itself. The results of that study were used by Sandia National Laboratories in a comparison of solar central receiver systems for producing process heat. In Sandia's study, the system with the volumetric receiver was predicted to have the lowest levelized energy cost. However, all designs were expensive when compared to conventional sources, so Sandia concluded that air heating receivers in general may not be a particularly attractive technology (De Laquil et al. 1983).

1.3 PROJECT OBJECTIVES AND SCOPE

Since previous studies involving the VAHR concept dealt with preliminary performance and cost estimates resulting from a simplified analysis of the concept, two activities were necessary before an objective evaluation of the feasibility of the concept could be made. First, additional development work was required to bring the concept from the infant stage of development with many questions regarding design details to a more developed stage where most of the design characteristics are specified. Second, rigorous modeling of the thermal processes was needed to resolve areas of technical uncertainty and verify the assumptions used in the simplified analysis. This project aimed at providing the additional detail and accuracy needed to assess the VAHR feasibility.

The VAHR project comprises four tasks. The first task developed the tools necessary for rigorously analyzing the thermal processes within the receiver. Section 4 describes the thermal processes and presents an overview of the models developed under this task. Then Sections 5, 6, 7, and 8 provide details of the models: Section 5 describes the radiation heat transfer modeling; Section 6 deals with modeling the airflow through the receiver; Section 7 documents the treatment of convective heat transfer from the absorbing material to

the air; and Section 8 describes the overall thermal performance model used to treat the results derived from the other models and estimate thermal performance.

Tasks 2 and 3 dealt with screening possible volumetric receiver designs by use of the models developed in Task 1, identifying the significant characteristics of the most attractive VAHR design, and developing a preconceptual design of that most attractive design. These tasks are described in Sections 9 and 10.

Task 4 involved developing capital cost estimates of the VAHR preconceptual design and the balance of system components, and evaluating the levelized energy cost for a VAHR system design. Details of the cost analysis are treated in Section 11.

Following this introduction, Section 2 summarizes the project's conclusions and recommendation.

Before the models are discussed (in Sections 4-8), it is instructive to review the evolution of the volumetric air heating receiver design. Section 3 presents this evolution by first reviewing the original VAHR concept, and then discussing the factors and decisions that led to subsequent designs and finally to the preconceptual design presented in Section 9.

2.0 CONCLUSIONS AND RECOMMENDATION

Based on the results of this study, a final preconceptual design of the volumetric air heating receiver (VAHR) was developed in sufficient detail to evaluate the feasibility of the concept. The current design consists of an array of 0.6-mm-diameter ceramic fibers to absorb the insolation, a row of slotted pipes arranged along the perimeter to induce air rotation, and a shroud to house the array.

Although this design looks far different from the original version of the VAHR, it still retains the primary characteristics of the volumetric concept: volumetric absorbing array, ambient air heating, and a geometric loss reducer. In an attempt to reduce the receiver size, fin-type absorbing arrays were ruled out in preference of ceramic fibers. Although these small ceramic fibers demonstrated better heat transfer and optical characteristics than fin-type arrays, convective heat transfer enhancement was required. The current design accomplishes this by inducing a "preswirl" to the air at the receiver perimeter and allowing conservation of angular momentum to increase the air velocity (relative to the fibers) as the air moves into the receiver. Lastly, our study demonstrated that the reflective row "light-valve" concept is not technically feasible. The current design uses a cavity-type shroud to reduce reflection and reradiation losses.

Several major areas of uncertainty affect the attractiveness of the VAHR concept. These areas center around the primary features of the VAHR: fiber integrity, preswirl generation, and the shroud performance.

The ceramic fibers in the absorbing array are subjected to harsh conditions. Since data are not available on the fiber's mechanical and thermal properties under such conditions, experimental evaluation would be required to address the fiber's survivability.

A second major uncertainty exists in the preswirl technique for convective enhancement. Since the theory of slotted jets in series does not exist, only a cursory analysis with many assumptions was made. One critical assumption was that the technique will generate a uniform preswirl velocity. A uniform swirl velocity will help reduce hot spots in the receiver. By placing the slotted

pipes out of the direct flux from the heliostat field, it may be difficult, if not impossible, to generate a reasonably uniform preswirl. To address the feasibility of this technique, substantial experimental research and development will be required before reliable performance predictions can be made.

Finally, tools were not available to adequately address the spillage and convection losses with the shroud design. As a result, the overall performance estimate of the VAHR design is subject to question.

In addition to these major uncertainties clouding the attractiveness of the VAHR concept, several qualitative advantages were lost that at one time made the concept look very promising. Originally the receiver was compact, simple, and passively operated. The current design is much larger, more complicated, and relies on active operation to provide convective enhancement. Furthermore, a receiver that originally was projected to have a thermal efficiency of 97% (including convective losses) is now predicted to have an efficiency of 82% (neglecting convective losses).

In light of these problems and questions with the VAHR concept, any further work on the concept will require a major new initiative to resolve the remaining questions about the VAHR feasibility. PNL estimates that the chance of clearing these issues is low enough to recommend that no further work be performed on the VAHR concept.

3.0 DESIGN EVOLUTION

Beginning with the original version of the volumetric receiver as described in the previous section, the current VAHR design evolved by a three-stage process. The primary objective of the study, to develop a high-performance, technically sound VAHR, was the driving force behind this evolutionary process. Although the current design looks far different from the original version, it retains the primary characteristics of the volumetric receiver concept: volumetric absorbing array, ambient air heating, and a geometric loss reducer. To lend perspective to the following sections dealing with thermal performance modeling, we review the three-stage evolution of the volumetric receiver design. Details supporting the decisions described below are presented in Section 9.

3.1 STAGE 1 - ABSORBING ARRAY

A large part of this study centered around selecting the appropriate configuration for the absorbing surfaces. The absorbing array, since it impacts radiative and convective heat transfer and airflow, significantly influences the size, cost, and performance of the receiver. We sought an absorbing configuration that was simple but yet had favorable heat transfer characteristics.

The original absorbing array called for staggered fin-shaped plates arranged in concentric vertical and circumferential rows around the receiver (Figure 3.1a). These high-absorptivity plates, fabricated from either high-temperature metals or ceramics, were staggered to improve convective heat transfer from the plate surfaces. Analyzing the radiative and convective heat transfer characteristics of this configuration led to the following conclusions:

- The staggered array geometry is complex, which greatly complicates modeling the combined radiative/convective heat transfer within the receiver.

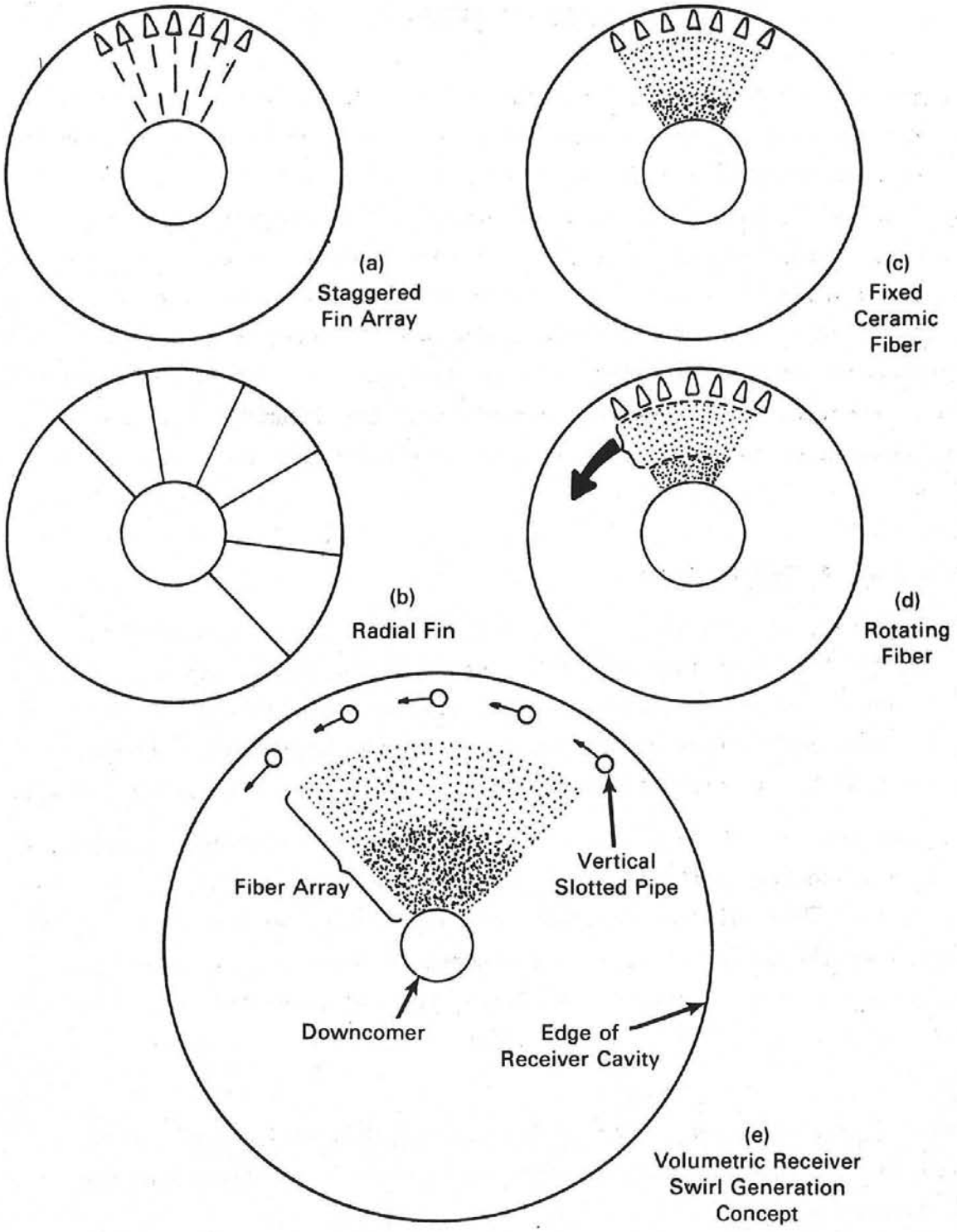

FIGURE 3.1. Volumetric Receiver Designs Considered

- To provide sufficient penetration of solar energy into the interior to disperse the absorption throughout the volume, a very open array is required.
- Despite the staggering of the plates, the convective heat transfer coefficients are low. This coupled with reduced surface area from an open array results in either excessive material temperatures or an extremely large receiver.

These results provided incentive to investigate two alternative configurations: radial fins and ceramic fibers.

The radial-fin configuration was initially pursued to provide a bounding assessment of the thermal radiation exchange for the staggered-fin configuration. This concept consists of vertical plate fins arranged radially around the receiver (Figure 3.1b). The uncomplicated geometry simplifies the radiation exchange calculation. This configuration in its simplest form (i.e., continuous radial fins) would lead to the development of a thick boundary layer for convective heat transfer. However, ways of tripping the boundary layer, and thus yielding convective heat transfer essentially equivalent to the staggered fins, could be incorporated into the surface configuration. Preliminary results showed that the distribution of incident flux in the radial direction can be controlled by the outer diameter of the receiver and the number of fins (i.e., the wedge angle formed by the fins), but a more detailed analysis revealed that a relatively large wedge angle was needed for proper flux penetration. So although the radial fin concept has advantages over the staggered fin idea (simpler construction and simpler analysis), it too suffered from inadequate convective heat transfer coefficients.

A ceramic fiber array, although not simple to analyze, has a marked potential for 1) increasing the rate of convective heat transfer, 2) eliminating concerns with angular variations in insolation, and 3) reducing the weight and cost of the receiver. This concept, using 0.6-mm ceramic fibers arranged vertically in an open packing, is shown schematically in Figure 3.1c.

Analysis of the fiber array showed that using small-diameter fibers significantly improved convective heat transfer compared to the fin designs. So

in many respects the fiber array outperformed the fin concepts, leading to the decision to select the fiber concept as the preferred absorbing array. However, though better than the fin designs, the fiber/air convective heat transfer coefficients were still relatively small. Combined with an open array requirement, this resulted in a very large receiver design.

3.2 STAGE 2 - AUGMENTING CONVECTIVE HEAT TRANSFER

Because the receiver size was so closely tied to the convective heat transfer coefficients, our study turned to investigating the potential for enhancing the convective heat transfer. Two primary approaches were considered; both deal with increasing the velocity of the air relative to the fibers.

The first method involves rotating a large portion of the array of fibers, which offers much higher convective heat transfer coefficients due to the increased relative velocities (Figure 3.1d). The result is a much smaller, but more complex and possibly less reliable receiver.

The second method entails inducing a swirl in the air by supplying angular momentum to the incoming air. Jets located around the periphery of the receiver would issue air tangentially, thereby imparting angular momentum to the incoming air stream (Figure 3.1e). By virtue of conservation of angular momentum, the angular (rotational) velocity of the air would increase as the air moves inward. This preswirl concept would also result in a much smaller receiver; yet it too would increase the complexity and uncertainty of the receiver concept.

The analyses of the two approaches were based primarily on performance; in addition, reliability, cost, and complexity associated with each approach were qualitatively assessed. According to this assessment, both methods performed comparably, and both added sufficient complexity and uncertainty to seriously jeopardize the technical feasibility of the volumetric receiver concept. We felt that the preswirl approach offered somewhat fewer technical problems, so it was included in the preconceptual design.

3.3 STAGE 3 - GEOMETRIC LOSS REDUCER

A high-performance central receiver must have some means of reducing thermal losses caused by reflection and reradiation. The receiver must admit solar energy from the heliostat field while blocking reflection and reradiation from the interior of the receiver. Two techniques were evaluated in this study to reduce radiative losses. The original "light-valve," described in Section 2 as a row of reflective wedges aligned vertically around the perimeter of the receiver, was initially thought to be an excellent means for reducing losses. However, an in-depth analysis of the reflective row technique proved otherwise.

Because 1) insolation from the field does not come in perpendicular to the receiver's outer surface, and 2) the aluminum reflecting material used for the wedges are not perfect reflectors, a significant amount of energy is absorbed in the reflective "zone." Since air velocities are low in this region, convective heat transfer is small. As a result, these aluminum wedges, regardless of their configuration and even with optimistic assumptions, operate at temperatures close to their material limits. Without a safety factor to allow for some maldistribution of airflow or absorption of insolation, this technique was not considered technically feasible.

The other geometric loss reduction technique was a shroud/cavity-type arrangement, where the absorbing array is housed in and protected by a shell (Figure 3.2). A cavity receiver is effective in reducing reflective and reradiative losses. However, this feature comes at a price. Since the aperture size is typically smaller for a cavity receiver, spillage losses are usually larger. In addition, a smaller aperture size poses problems with uniformly distributing the insolation throughout the absorbing volume. Several configurations were investigated; these are reported in Section 9.

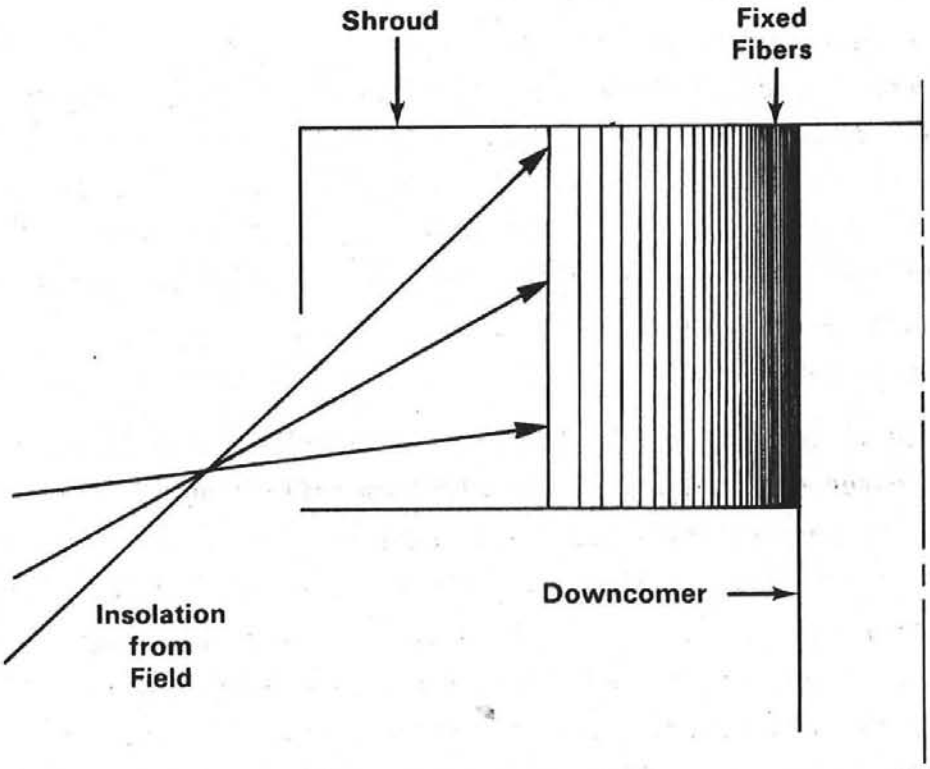

FIGURE 3.2. Conceptual Sketch of a Shrouded Volumetric Receiver

4.0 VOLUMETRIC RECEIVER THERMAL PROCESSES

The volumetric receiver is a unique design and consequently involves thermal processes and applications which are not encountered in more conventional receiver designs. This section will provide an overview of the thermal processes associated with the volumetric receiver and will provide the background for the discussion of the models described later in the report.

A variety of thermal processes take place during the operation of the VAHR. We categorize them into three main topics: 1) processes dealing with thermal radiation heat transfer; 2) processes involving the flow of air through the receiver, and 3) processes involving convective heat transfer between surfaces and air. Section 4.1 describes the radiation heat transfer processes occurring in the volumetric receiver and discusses the problems associated with distributing the insolation throughout the absorbing array and minimizing reflective and reradiative losses to the surroundings. Section 4.2 deals with the air flow through the receiver, problems associated with assuring proper flow distribution and pressure drop, and prevention of excessive convective flow out of the receiver. Section 4.3 pertains to the convective transfer of energy from the hot receiver surfaces to the cooler air. Finally, Section 4.4 discusses the need for modeling these thermal processes, presents an overview of the individual models developed to simulate the processes, and describes how these models fit together to characterize the thermal performance of the volumetric receiver.

4.1 RADIATION HEAT TRANSFER

Radiation heat transfer is involved in both the distribution of insolation from the heliostat field and the internal radiation exchange between surfaces. These are related but distinct problems and will be discussed separately, but first the characteristics of the insolation will be described.

4.1.1 Properties of Insolation

The insolation striking the receiver is composed of a large number of heliostat images. Each heliostat redirects the sun's radiant energy onto the receiver, forming an image. In a typical heliostat field, heliostats are

located over a large area. For a 50-MWt facility, the closest heliostat to the tower may be 80 m away from the centerline of the tower, while the most distant heliostat may be 500 m away, with the typical heliostat located approximately 400 m away. This produces a wide variety of image sizes and incident angles in the vertical direction on the receiver. Figure 4.1 shows the variations in incident angle and image size for a hypothetical 50-MWt field.

In characterizing the insolation for this study, we assumed that the heliostats are aimed to provide a uniform distribution of energy on the outer surface of the receiver. Although this aiming strategy increases the likelihood of spillage losses, it is necessary to properly distribute the energy throughout the receiver volume.

The volumetric receiver performance, particularly for designs with reflective wedges, is sensitive to the incident angle (θ) of the insolation in the circumferential direction. As Figure 4.2 shows, radiation entering a typical reflecting wedge cell will tend to be absorbed or reflected out to the surroundings if the incident angle is very large.

At any given point on the receiver's outer surface, the distribution of the incident angle can be assumed to be Gaussian. The standard deviation of the incident angle distribution is related to the standard deviation of the heliostat flux distribution in the image. Defining the image width as the image diameter which contains 95% of the image, one half of the image width equals the standard deviation of the image distribution. The standard deviation for the incident angle distribution is given by

$$\sigma_{\alpha} = \sin\left(\sigma_{image}/R\right)$$

By analyzing heliostat flux data from King (1982), we determined that the typical heliostat in a 50-MWt facility produced an image distribution with a 1.0-m standard deviation.

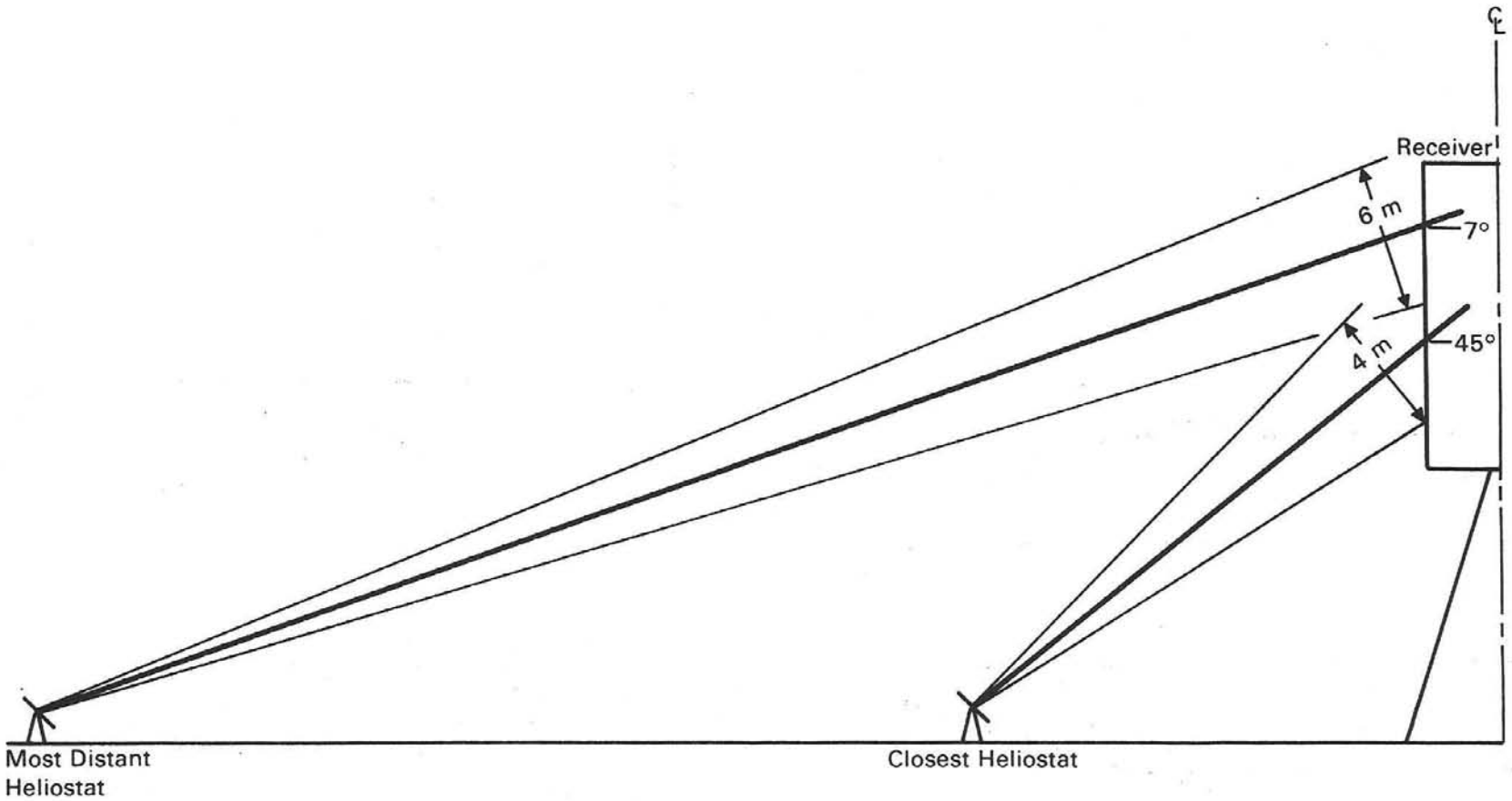

FIGURE 4.1. Incident Angle and Heliostat Image Size for a Hypothetical 50-MWt Field

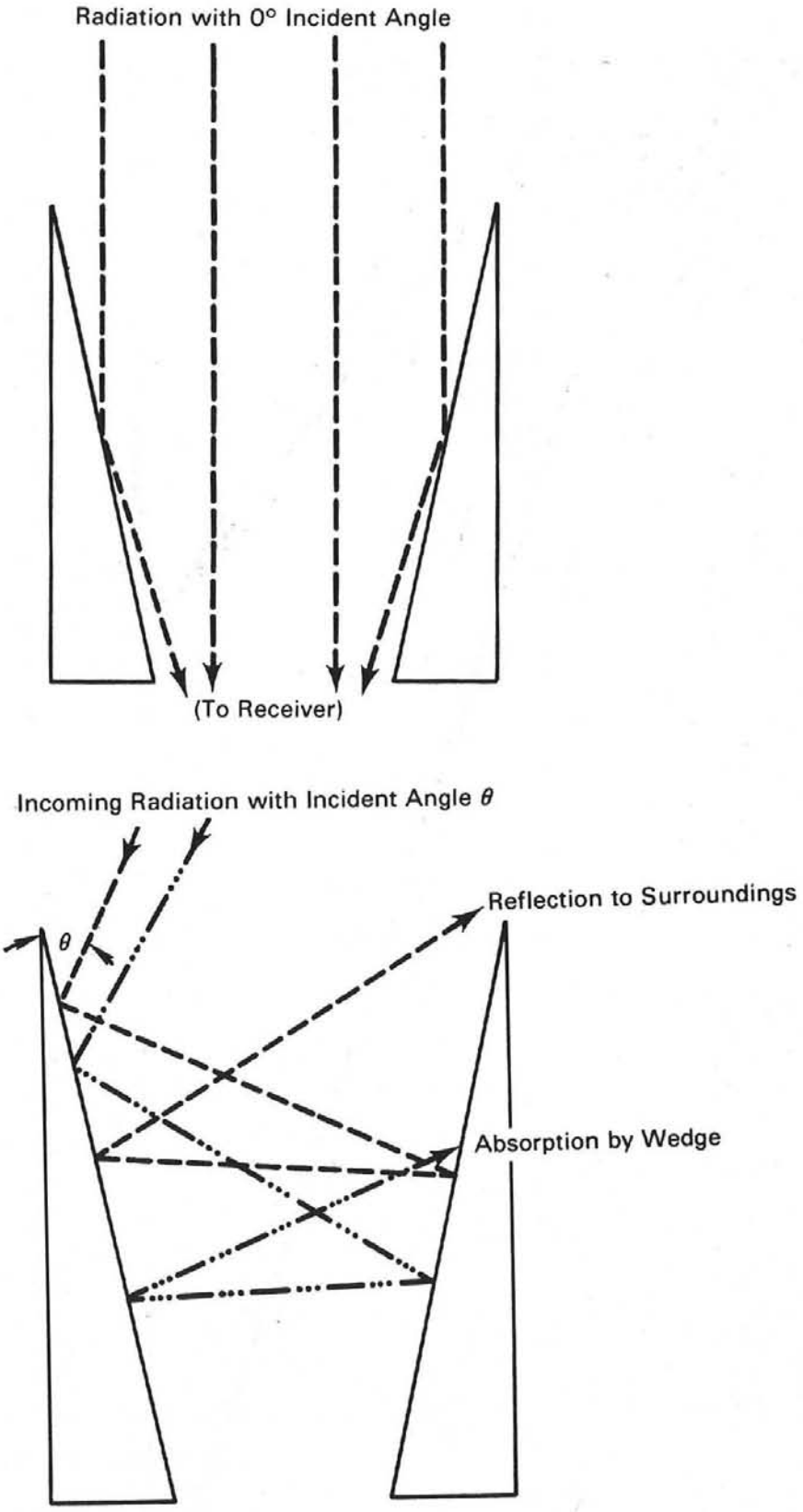

FIGURE 4.2. Impact of Incident Angle Distribution

4.1.2 Insolation Absorption

The factors affecting insolation absorption in a volumetric receiver can best be described by following a hypothetical photon as it interacts with the receiver surfaces. The photon enters the receiver and can either pass through the row of reflecting wedges without striking a surface or hit a reflecting surface. When the photon strikes the surface of the reflecting wedge, several results are possible. The photon may either be absorbed, specularly reflected, or diffusely reflected. The reflecting surface is selected to have a low absorptivity and high specularity, so we assume that the photon is reflected into the receiver. The photon moves into the receiver until it strikes a high-absorptivity surface, where the photon is most likely absorbed. If the photon is reflected, it may move deeper into the receiver, or it may move toward the outer surface of the receiver and may actually leave the receiver. In the latter case, the photon would contribute to reflection losses. If the photon stays in the receiver, it will continue striking surfaces until it is absorbed.

The results of a surface/photon interaction will depend on the optical properties of the surface. In general, surface properties such as absorptivity, emissivity, and specularity will depend on characteristics of the surface, such as its temperature and surface conditions, and on the characteristics of the incident radiation, particularly incident angle and spectral distribution (Siegel and Howell 1972).

The impact of the incident angle distribution is important. Any deviation from a normal angle of incidence (i.e. $\theta = 0$) will reduce the depth of penetration of a photon into the receiver. As the angle of incidence increases, photons will tend to strike the reflecting surfaces and be reflected back and forth between the wedges until they are absorbed or reflected out of the receiver. At a sufficiently large incident angle the insolation will be completely absorbed on the reflecting wedges or reflected away from the receiver, with none of the insolation penetrating into the receiver.

A photon entering a cavity-type receiver design will experience a slightly different set of interactions. First the photon must enter the receiver through the aperture of the enclosure without actually striking the enclosure. Once inside the receiver, the photon must actually strike the absorbing

surfaces (there is the possibility that a photon may enter the cavity, miss the absorbing surfaces, and pass through the other side of the receiver). When the photon strikes the first absorbing surface, it will probably be absorbed; but if the photon is reflected outward, it may either leave the receiver or be absorbed on the cavity surface. Once a photon enters the absorbing array, its history will be similar for either a reflecting wedge or shroud design.

The selection of aperture size is a critical decision in a cavity-type design. A large aperture will let most of the insolation enter the receiver and will simplify the insolation distribution on the absorbing surfaces, but it will be relatively ineffective in blocking reflected radiation and reradiation from the absorbing array. A small aperture will have low reflection and reradiation losses, but much of the insolation will strike the exterior surface of the enclosure and be lost as spillage.

4.1.3 Internal Radiation Heat Transfer

As the various surfaces in the receiver absorb energy, their temperatures increase and they will begin to emit radiant energy in all directions. Some of the energy will be absorbed by other receiver surfaces and a fraction will leave the receiver and be a reradiation loss. A given surface will both radiate energy and receive radiated energy from other surfaces, resulting in a net loss or gain for the surface. Though the calculation of internal radiation heat transfer is complicated, internal radiation heat transfer is a major mechanism of energy exchange and cannot be ignored.

4.2 AIR FLOW

One unique feature of the volumetric receiver is that ambient air is drawn directly into the receiver. This has the advantage of making the absorbing array look like a counterflow heat exchanger with the external surfaces having the lowest temperatures. But care must be taken to ensure proper airflow distribution. As the receiver surfaces heat up, the major mechanism for removing energy from the surface to the air is convective heat transfer. If air is not distributed in a manner approximating the distribution of absorbed insolation, the radiant energy absorbed on a surface will not be removed quick enough to

prevent the surface from overheating. Therefore, air flow into the receiver must be properly distributed both axially and circumferentially.

If the receiver was at ambient temperature and if an inlet manifold was not included, the air entering the receiver would be concentrated along the bottom of the absorbing array. With the receiver at operating temperature (1400 K), there will be a drastic change in the air density from the external rows to the internal rows. Bouyancy will tend to give the air velocity a vertical velocity component. In addition, orifices in the inlet manifold will help properly distribute air flow.

The driving force for the air flow is the pressure difference caused by the induced draft fan. Momentum added to the air by the fan will be used to overcome drag caused by the receiver surfaces, inlet manifold, and downcomer, and to accelerate the air. Viscous effects should be negligible.

Air flow distribution in the circumferential direction should be tailored to meet the circumferential distribution of insolation, which tends to be greatest on the north side of an open receiver and smallest on the south side. In addition, wind effects may cause circumferential variation in air flow distribution by causing a higher than normal pressure at the stagnation point and a lower than average pressure on the downstream side of the receiver.

As indicated above, bouyancy effects caused by large variations in air density will cause the air to rise in the receiver. When air reaches the receiver roof, most of the air will be drawn into the receiver but some will recirculate and exit the receiver; the energy used to heat this exiting air is considered a convection loss.

Two methods for augmenting convective heat transfer between the fibers and the air were considered in this study; both involved specific air flow problems. The preswirl concept consists of providing the incoming air with tangential momentum and allowing conservation of angular momentum to increase the tangential velocity as the air moves into the receiver. The major air flow problems involve calculating the relative fiber-air velocity as a function of receiver location and in determining the most attractive method of providing the initial angular velocity.

The rotating fiber concept adds another complicating factor to the air flow analysis: determining the proper rotation speed. The purpose of rotating the fibers is to increase the relative velocity between the fibers and the air and thus increase the convective heat transfer from the fibers. But as the fibers rotate through the air, the drag on the fibers will accelerate the air in the circumferential direction. Once the air has a circumferential velocity, density variations and conservation of angular momentum will tend to further accelerate the air tangentially. This air velocity will reduce the relative velocity between the fibers and the air, thereby reducing the convective heat transfer.

4.3 CONVECTIVE HEAT TRANSFER

As the absorbing surfaces receive radiant energy, they will increase in temperature until an energy balance is reached. Since convective heat transfer to the air is the most significant mechanism for removing heat from the absorbing surfaces, it determines to a great extent the equilibrium temperature of the receiver surfaces. A large convective heat transfer coefficient leads to the lowest temperature difference between the absorbing surfaces and the air.

Three primary factors influence the size of the convective heat transfer coefficient: the velocity of the air relative to the surface, the characteristic dimension of the surface, and the temperature difference between the surface and the air. The temperature difference plays an important role in natural and mixed-mode convective heat transfer. As the temperature difference increases, the driving force for natural convection increases, which raises the convective heat transfer coefficient. Velocity plays a critical role in forced and mixed-mode convection. Regions with high velocities will have correspondingly high heat transfer coefficients. A third way of increasing the heat transfer is by using a surface with a small characteristic dimension. Small-diameter fibers fit this category. Any decrease in fiber size will increase the convective heat transfer coefficient (i.e. $h \sim \frac{1}{d^{1/3}}$).

4.4 RECEIVER THERMAL PERFORMANCE MODELING

The unique features and unusual geometry of the volumetric receiver dictated that special models be developed to simulate the transfer processes occurring in the receiver. Models were developed to calculate: 1) both the distribution of insolation from the heliostat field through the receiver and the thermal radiation exchange factors for the surfaces in the receiver; 2) the air flow through the receiver, providing estimates of the convective losses from the receiver, the axial variation of air flow, and the pressure drop through the receiver; 3) the amount of convective heat transfer to the air from the absorbing surfaces; and 4) the receiver material and air temperature profiles and receiver thermal losses.

Because of the large number of surfaces in the receiver, many of which are not diffuse, it is difficult to calculate where the insolation from the heliostats is absorbed in the receiver, as well as the radiation exchange between surfaces within the receiver. For this problem a specialized Monte Carlo model was developed for the VAHR. Given the receiver geometry and the angular distribution of energy from the heliostats, the model uses a Monte Carlo technique to predict the distribution of absorbed insolation through the receiver and to estimate the exchange factors between "zones" within the receiver. The model also determines the amount of energy lost by reflection.

Modeling the air flow through the receiver is also complex, particularly for the region where the fibers and/or air are rotating. Two different models are used here. TEMPEST, a general-purpose thermal-hydraulic computer code developed by PNL, was used to model both convective losses from the receiver and the two dimensional (radial and axial) air flow through the receiver. TEMPEST modeling provided estimates of the convective heat loss from the receiver, and the axial and radial variation of air flow and magnitude of the pressure drop through the receiver.

The computer code VORTEX was developed to address: 1) concerns that the rotating fibers would impart enough angular momentum to the air such that the air would rotate to where there would be little relative velocity between the air and the fibers, and 2) how the tangenitial velocity of the air varies, given an initial "preswirl." The results of the VORTEX modeling provided

estimates of the radial variation of the angular velocity, the relative velocity between the air and fibers, and the power required to overcome the drag from the rotating fiber region.

An additional tool was needed to combine the information provided from the models discussed above in such a way to provide estimates of the temperature distributions of the air and fibers in the receiver, and to predict the losses from the receiver. This required developing a receiver performance model. The model couples the incident energy absorbed throughout the receiver with both the radiation exchange and convective heat transfer from the receiver material to the air. The receiver is modeled as a series of concentric cylindrical zones with air being drawn through the zones toward the downcomer. In addition to the receiver geometry, the model requires information on the absorbed insolation, the radiation exchange factors, and the air/fiber relative velocities for each zone. An energy balance written for each zone yields a set of equations of zone temperatures as a function of these inputs. Solving these equations provides temperature profiles of the air and receiver material and the amount of radiation lost to the surroundings.

5.0 RADIATION HEAT TRANSFER MODELING

Much of the attractiveness of the volumetric receiver depends on the impact of its unusual geometry on radiation absorption and heat transfer. The receiver absorbing rows are placed so that high-temperature surfaces will be in the interior of the receiver, thereby reducing reradiation and reflection losses from the receiver. The reflecting rows or shroud also reduce radiation losses by acting as a "light valve," which allows insolation to enter the receiver but inhibits reflected or reradiated energy from leaving the receiver interior. Both features can substantially reduce receiver thermal losses. To have any confidence in the predicted performance results, an accurate method of calculating radiation heat transfer must be available. This section describes the problem of analyzing radiation heat transfer and gives an overview of the selected analytical approach. Section 5.1 discusses the details of the problem and the possible solutions while Section 5.2 presents a background overview of Monte Carlo modeling. Section 5.3 discusses the exchange factor model while Section 5.4 presents the absorbed insolation distribution model. The comparison of code predictions with experimental results is provided in Section 5.5, while a discussion of the impact of sample size on the results is included in Section 5.6. The appendix describes the details of the specialized Monte Carlo code developed for volumetric receivers. Further details are given by Drost (1984).

5.1 SELECTION OF MODELING APPROACH

Radiation heat transfer analysis can be quite complex, particularly when a large number of surfaces with nonideal optical properties are considered. The analytical techniques available for radiation heat transfer vary widely in required effort, limiting assumptions, and accuracy. This section describes the radiation heat transfer problem and discusses the reasoning used in selecting Monte Carlo modeling as the preferred approach.

5.1.1 Problem

A radiation heat transfer analysis is required for all performance calculations. In particular, the following information is required:

1. Distribution of Absorbed Insolation - As insolation reaches the receiver, it will pass through the reflecting zones or shroud with a fraction being absorbed or reflected and then enter the absorbing zones, where the remaining radiation is absorbed. The radiation analysis must predict where insolation is absorbed in the receiver for varying receiver geometries, surface properties, and insolation characteristics. This analysis should also predict reflection losses from the receiver.

2. Thermal Radiation Exchange Factors - The radiation analysis must also predict the radiation exchange from receiver surface to receiver surface and from receiver surface to the surroundings (radiation exchange to the surroundings represents a thermal loss). Since complete radiation exchange calculations between surfaces cannot be made until surface temperatures are known, exchange factors between surfaces are first calculated and used later for performance calculations.

The radiation heat transfer analysis is particularly complicated because of the large number of surfaces involved (approximately 50 for a symmetrical section of a fin-type receiver, and several hundred for a fiber-type receiver) and because of the importance of including directional surface properties and possibly spectral properties.

5.1.2 Applicability of Analysis Methods to the VAHR

The efforts of many investigators have resulted in the development of a variety of methods for analyzing radiation heat transfer problems. Our literature review identified two generic types of analysis appropriate for modeling the radiation heat transfer in a volumetric receiver. The first method models the radiation between individual receiver surfaces, while the second models the receiver absorbing surfaces as an emitting or absorbing gas without individual

surfaces being identified. The fin-type concepts clearly could not be modeled as an absorbing or emitting gas because: 1) this model would not give results with the detail required, and 2) a fin array exhibits strongly anisotropic characteristics, which would prohibitively complicate any analysis. A fiber receiver could possibly be modeled as an absorbing or emitting gas because of the large number of small surfaces.

Fin-Type Receiver Radiation Modeling

The key problem in modeling discreet surfaces is predicting the view or exchange factor between surfaces. Emery et al. (1981) identified seven methods for predicting view factors. They concluded that for complicated configurations only numerical methods are appropriate, particularly for cases with partially obstructed views, which is the case for the volumetric receiver. Of the four numerical approaches, Emery et al. conclude that a Monte Carlo approach is best suited to the determination of view factors between a single small area and surrounding areas. This is normally the situation encountered in the volumetric receiver where we are interested in radiation heat transfer for either a small fin or a small symmetric section of the receiver exterior boundary. Monte Carlo modeling has the added advantage of allowing the inclusion of non-diffuse, nongray surfaces with relative ease (Siegel and Howell 1972; Howell 1968; Toor and Viskanta 1968).

With the selection of Monte Carlo modeling, there were still two possible approaches; a general Monte Carlo computer code could be acquired or a Monte Carlo computer code designed specifically for a volumetric receiver could be developed. A variety of generalized Monte Carlo photon and neutron transport codes (Halbleib 1979; Los Alamos 1978) and Monte Carlo radiation heat transfer codes (Corlett 1966) exist. In both cases these codes are very general; the resulting complexity would require excessive computer time, particularly for use as a design tool where many geometric arrangements would have to be considered.

For our purposes the preferred method of modeling radiation heat transfer was to develop a specialized Monte Carlo computer code designed to take advantage of the regular geometry of the volumetric receiver to reduce computer time.

Fiber-Type Receiver Radiation Modeling

The fiber-type receiver could by modeled as an absorbing or emitting gas and evaluated using either analytical techniques such as solutions of the equation of transport or zoning methods (Siegel and Howell 1972). However, all analytical methods ultimately depend on having an estimate of the attenuation and scattering caused by the fibers. This information can only be developed by either Monte Carlo modeling or experiment.

Monte Carlo modeling can use either specified surfaces with a fixed location or a statistical method to determine the location of an event. The first method is similar to the method selected for analyzing the fin designs. The second method has been used by a number of authors to investigate radiation heat transfer in packed beds (Yang 1981) and participating media (Mishkin and Kowalski 1983). This approach was attractive but finally rejected because it would require the development of a second Monte Carlo code; therefore, one Monte Carlo approach using discreet fixed surfaces was selected for both fin and fiber designs.

5.2 MONTE CARLO MODELING

The Monte Carlo approach to radiation heat transfer problems has been widely used and the method is well documented (Siegel and Howell 1972; Toor and Viskanta 1968; Weiner et al. 1965). In this section the Monte Carlo method is briefly described. The specific model used for analyzing the volumetric receiver is described in the Appendix.

The Monte Carlo approach is a statistical method of modeling a problem as a series of probabilistic and deterministic events. In thermal radiation heat transfer applications energy emitted from a surface is simulated by a large number of photon bundles. The emitted bundles are followed as they proceed from one event to another with the results of each event being recorded until the photon bundles either leave the receiver or are absorbed on a surface. A large number of bundles are simulated, and the results of all events are totaled. A sufficiently large number of bundles must be considered to insure that variations in the results due to random events are small. The results can

then be used to determine the fraction of the emitted energy which either has been absorbed on each surface or has the left the receiver.

The major problems with Monte Carlo modeling deal with geometrical considerations (which surface is struck by a bundle?) and surface considerations (what happens when the surface is struck?). Methods of modeling the interactions of a bundle with a surface are described by several authors (Siegel and Howell 1972; Yang 1981). When a photon strikes a surface the incident angle and wavelength should be known. If surface properties such as absorptivity and specularity are known as a function of incident angle and wavelength, then the relevant optical properties can be calculated. If the bundle is totally or partially absorbed, the energy reduction due to the interaction is added to the total absorbed for that surface. A reflection angle must be selected for a diffusely reflected photon bundle. This reflection angle is selected in such a way as to insure that there is an equal probability for reflection in any direction. If the reflection is specular, the angle of reflection equals the angle of incidence.

The problems associated with receiver geometry involve determining which surface is struck by a photon bundle once the bundle has been emitted. This problem has been avoided by many researchers by selecting simple geometries. When complex geometries are considered (Corlett 1966; Modest 1968), the method consists of describing each surface mathematically and determining which surface intercepts the vector that describes the path of the energy bundle. The distance between the emission point and each intercepting surface is calculated and the surface with the shortest distance is identified as the surface struck by the energy bundle. When a large number of surfaces is involved, the computational time associated with determining impact location becomes substantial.

The volumetric receiver includes an arrangement of pins in concentric cylindrical rows. The regular spacing of the pins and their arrangement into rows suggests that a more efficient method of determining impact location can be used. This approach consists of dividing the receiver into computational cells, where the cells are arranged so that absorbing surfaces are located on cell boundaries. This simplifies identification of the impact location because one of the four surfaces in a cell is the emitting surface and only the three

remaining cell boundaries can be struck by the emitted photon bundle. The details of this approach are described in the Appendix.

5.3 EXCHANGE FACTOR CALCULATION

The exchange factors from one zone to all other zones are calculated by selecting a typical fin or fiber in the zone and emitting photon bundles from all four fin or fiber surfaces. The photon bundles are followed and their histories are noted. After a sufficiently large number have been simulated, the resulting absorbed energy distribution gives the fraction of energy leaving the emitting surface and being absorbed on the absorbing surface. Then the exchange factor can be calculated from Equation (5.1) (Toor and Viskanta 1967).

$$F_{ij} = \lim_{N \to \infty} \left(N_{i-j} / N_i \right) \tag{5.1}$$

The significance of F_{ij} and its relationship to other radiation properties are discussed in Section 8.

The calculation of exchange factors follows the same procedure as for the determination of insolation distribution. A photon bundle is emitted into a cell, and the interactions between the cell and the photon bundle are determined. If the energy level of the photon bundle has not dropped below the minimum energy level, the photon bundle will exit the cell and move into a new cell, where it can interact with the cell boundaries. This procedure is continued until the photon bundle either exits the receiver or its energy level drops below the minimum amount.

The main difference between the insolation calculation and the exchange factor calculation is in the location of the initial emission. The point of emission for exchange factor calculations is determined by dividing a typical fin or fiber surface into increments and emitting photon bundles from the midpoint of each increment. The number of photon bundles emitted in each

increment is based on the surface area of the increment relative to the total surface of the fin or fiber. The number of photons emitted from increment i is given by

$$NPHIM_i = \frac{NPHOT \times Area_i}{\sum_{j=1}^{n} Area_j} \qquad (5.2)$$

where $NPHIM_i$ = number of photon bundles emitted from increment i

$Area_j$ = surface area of increment j

NPHOT = number of photons emitted from fin or fiber

All emitting surfaces are assumed to be diffuse emitters. The selection of emission angle follows the same procedure used for selecting the angle for diffuse reflection described in the Appendix.

This method for calculating exchange factors assumes that a zone consists of one row of fibers or fins and that there is a regular spacing between the fibers or fins. In addition, the geometric relationship between surfaces in any one row and all other rows must be constant in the circumferential direction. In this case a symmetry argument can be used to justify using one typical fin or fiber as the emitter because all fins or fibers in a given zone "see" the same geometric arrangement in all other zones. Those restrictions are met in all volumetric receiver designs with one exception, the staggered fin array, where the fins are packed more densely in the interior zones. In that array, one "typical" fin was selected as the emitter, although it was understood that other fins in the same zone would "see" different geometric configurations. In fiber designs, simulations have shown that the emitting surfaces are so small compared to the spacing between zones that the relative arrangement of fibers in different zones had no detectable effect on exchange factor calculations.

The calculation of a complete set of exchange factors for a receiver consists of taking one representative fiber or fin in each zone and determining the exchange factors to all other zones. For a receiver with n zones, this will require n Monte Carlo simulations and will produce an n + 1 by N + 1

matrix of exchange factors where the surroundings are now included as one zone. The calculations of exchange factors make substantial demands on computing resources.

5.4 INSOLATION DISTRIBUTION CALCULATION

The calculation of insolation distribution is similar to exchange factor calculations. Here the results consist of exchange factors from the surroundings to the receiver surfaces. As with exchange factor calculations, the use of one typical emitting surface in calculating insolation distribution is based on the assumptions of regular spacing between fins and fibers in a zone and constant geometric relationships between surfaces in one row and all other rows.

The calculations of absorbed insolation distribution involves one Monte Carlo simulation. The results are the fraction of insolation absorbed in each of n zones and the fraction of energy exiting the receiver to the surroundings. The last result is the reflection loss from the receiver.

5.5 MODEL VERIFICATION

The Monte Carlo model described above was used as the basis for two computer codes. The VORRUM computer code calculates absorbed insolation distribution while the VORVFM code calculates exchange factors. In order to develop confidence in the analytical model and the resulting computer codes, a variety of tests were conducted to verify the results. The verification of a Monte Carlo code is complicated because of the variation in results caused by the probabilistic nature of the technique. Therefore, three approaches were pursued: comparison with ray tracing by hand, comparison with analytical results, and comparison with experimental results.

The first method compared the predicted locations of photon bundle impact and incident angles with hand calculations and graphic ray tracing. In all cases the predicted results duplicated hand calculations.

The second approach compared predicted results with analytical results for a single, simple enclosure with surfaces of either black or diffuse-gray. The

enclosure is shown in Figure 5.1. In the diffuse-gray case the analytical results are approximate because the diffuse-gray model assumes uniform incident flux on each surface. This is a poor assumption for the case being studied. To improve the accuracy of the analytical calculation, surface four was divided into four zones, each assumed to be isothermal and subject to uniform incident flux. The results for this case are reported in Table 5.1.

The final method of verifying VORRUM involved comparing the predicted results to experimental results. The fraction of radiation transmitted through

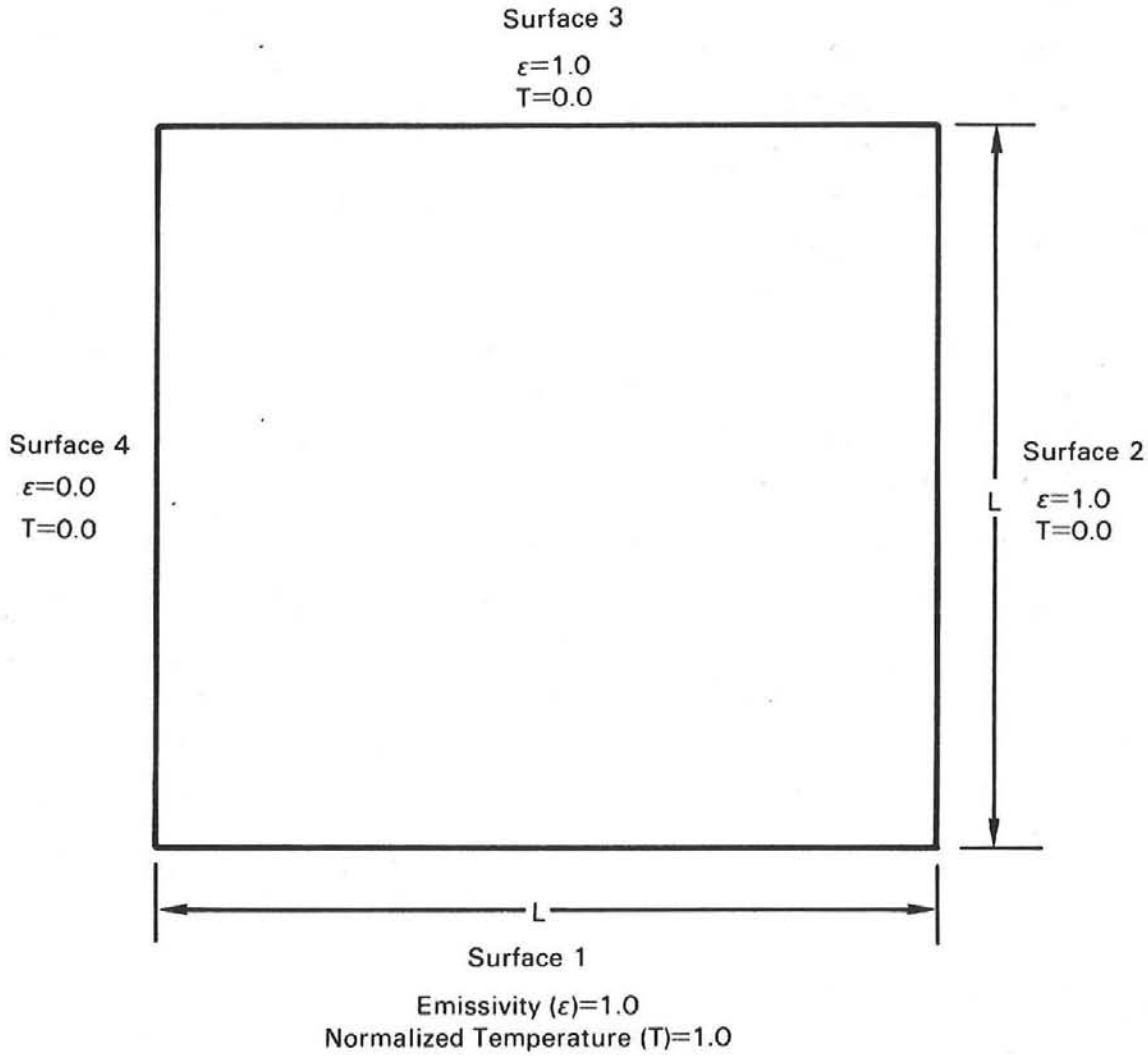

FIGURE 5.1. Enclosure Used for Comparison with Analytical Results

TABLE 5.1. Analytical Results Versus VORRUM Prediction

Diffuse-Gray Surfaces			
	% of Energy Leaving Surface		
Heat Transfer Path	Analytical	Computed Results	Computed Results Standard Deviation
1-2	41.39	41.36	0.94
1-3	48.97	48.86	0.97
1-4	9.64	9.78	0.50

both one and two reflecting zones was determined experimentally by PNL for a range of inlet angles. The results for the first row are presented in Figure 5.2. VORRUM was used to simulate the same situation, and assumed a constant emissivity independent of incident angle or wavelength and was modified to emit all photon bundles at the incident angle of interest. The results show that VORRUM duplicates the general trend of decreasing transmittance with increasing angle of incidence. As the angle of incidence increased, VORRUM tended to underestimate the transmittance. Inlet angles off normal produce multiple reflections. This type of situation has been recognized as being the most challenging for a Monte Carlo simulation (Howell and Bannerot 1974). The conclusion, given the uncertainties in the experimental results, is that VORRUM successfully predicted experimental results, with predicted results being conservative since zone absorption is overestimated.

A second comparison was made between experimental results and the results predicted by VORRUM. In this case the experimentally determined transmittance of two reflecting zones was compared to the transmittance determined using VORRUM. The comparison is presented in Figure 5.3. As with the one-zone case, VORRUM tends to underestimate the transmittance while duplicating the general trend of decreasing transmittance with increasing angle of incidence. In general, given the uncertainties in the comparison, it appears that VORRUM can successfully predict experimental results.

The VORVFM exchange factor uses the same Monte Carlo technique as VORRUM, so results of the comparisons described above are assumed to also apply to the VORVFM code. The main difference between the two codes is in the initial emission of the photon bundles. These calculations agree with hand calculation.

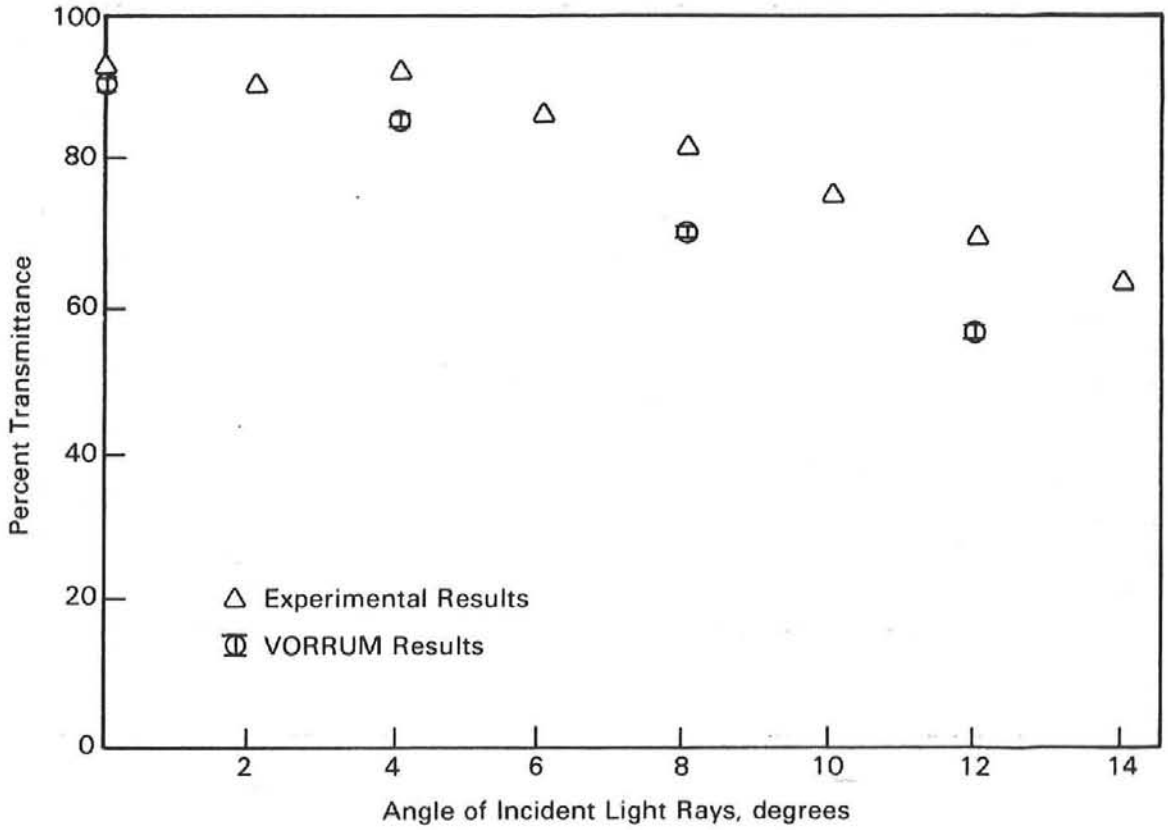

FIGURE 5.2. Comparison with Experimental Results--Transmission Through First Reflecting Zone

5.6 SAMPLE SIZE CONSIDERATIONS

The uncertainty in the results of a Monte Carlo simulation depends on the number of photon bundles simulated. As this number approaches infinity, the uncertainty and the computer budget both approach zero. Since the computer budget was limited, some compromise between uncertainty and running time was required.

Early sensitivity studies indicated that the variance in the results was decreased by using the minimum number of batches consistent with the assumption of a Gaussian distribution of the results. In addition, these studies incrementally reduced photon energy rather than having the photon either terminated or uneffected by an interaction. This allowed more information to be obtained from one photon bundle. Other variance reduction techniques, such as photon

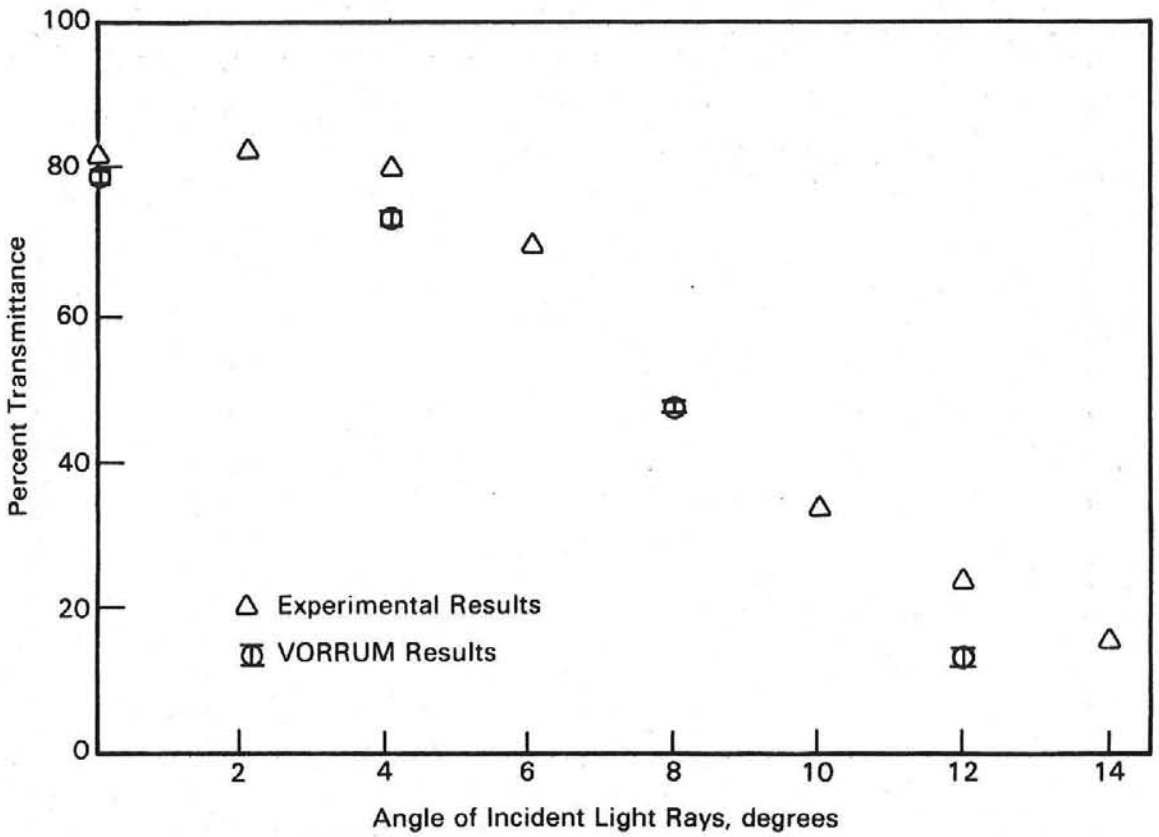

FIGURE 5.3. Comparison with Experimental Results--Transmission Through First and Second Reflecting Zones

bundle splitting and Russian Roulette were investigated, but these are appropriate only where there is one small area of interest in the region being simulated. This was not the case in the volumetric receiver simulation.

The design procedure consisted of using small numbers of photons in survey studies to identify attractive designs and then increasing the sample size once a design had been selected. Survey studies using VORRUM used photon batch sizes of 100 for 20 batches and produces standard deviations that were around 20% of the mean value for most results. Preliminary calculations were made using batch sizes of 800 for 20 batches, which resulted in standard deviations that were around 5% of the mean values. Because of the expense of calculating exchange factors, VORVFM was run with batch sizes of 100 for 20 batches. While

the uncertainty experienced in this study was suitable for a survey study, a detailed design would require VORRUM and VORVFM simulations with much larger batch sizes, perhaps 5000 photons per batch. This would require around 10,000 CPU seconds of computer time on a CDC 3300 computer.

6.0 AIR FLOW MODELING

Operation of the volumetric receiver requires that energy absorbed in the receiver be continually removed by the air being drawn into the receiver. However, merely establishing a specified air flow rate is not sufficient to guarantee proper cooling. The air flow distribution in the receiver must be such that regions of excessively high or low temperatures are avoided. Such regions not only impair receiver performance, but can also endanger its integrity. Another consideration in receiver performance is the degree of convective loss it experiences. If the air inflow velocity at the receiver periphery is too low, large amounts of thermal energy could be lost to the surroundings through natural convection. Finally, the determination of receiver pressure drop is important because it determines the power requirement for providing the air flow.

The air flow analysis task can be divided into three major areas of concern: 1) receiver air flow distribution, 2) receiver convective loss, and 3) receiver pressure drop. The purpose of this task was to analyze air flow in prospective receiver designs from these three standpoints, identify deficiencies, and provide feedback to the design process. This chapter describes the analysis methods used to accomplish this. Section 6.1 deals with the methodology for determining the orifice strategy for the inlet manifold to obtain the desired axial distribution of air inflow and for determining the receiver pressure drop. Analysis of air flow distribution for receiver designs which induce rotational air flow to enhance convective heat transfer is described in Section 6.2. The procedure for calculation of the convective losses from the receiver is described in 6.3.

6.1 MANIFOLD ORIFICING AND RECEIVER PRESSURE DROP

6.1.1 Orifice Distribution Calculation Method

Early in the development of the volumetric receiver, it was found that an orifice distribution scheme for the inlet manifold would have to be adopted to obtain the desired axial distribution of air inflow to the receiver. In the initial receiver design, where no orifices were employed, the air flow was

grossly maldistributed with most of the flow occurring in the bottom of the receiver. Adding orifice holes to the manifold to choke off this excess flow and force more air to flow through the upper portions was seen as a way of correcting this situation. However, the problem with implementing this idea was how to determine the required orifice configuration.

Since heat generation in the receiver is assumed to be axially uniform, the desired air inflow distribution should also be axially uniform. If a uniform orifice distribution along the manifold is assumed, a uniform pressure drop across the manifold would exist and there would be no pressure drop along the manifold. However, this is not the case. Air is constantly being added to the down-flow in the manifold by the flow through the orifices. This accelerating flow in the manifold will create a pressure drop along its length. Therefore, it is evident that a nonuniform orifice distribution is required. The correct distribution will result in a balance between the pressure drop across the orifices and the pressure drop along the manifold. To establish this balance, the expressions for flow through an orifice [Equation (6.1)] and the pressure gradient along the manifold are formulated [Equation (6.2)]. They are:

$$\dot{m} = dw = c\sqrt{2g\rho\,(P_{atm} - P)}\;a\;dx \tag{6.1}$$

$$\frac{dP}{dx} = \frac{-16w}{\rho\pi^2 D^4 g}\frac{dw}{dx} \tag{6.2}$$

where w = manifold flow (lbm/sec)
a = total orifice area per unit length (ft)
c = orifice coefficient for single hole
D = manifold diameter (ft)
ρ = air density (lbm/ft^3)
$\dot{m}$ = flow through orifices (lbm/sec)
P_{atm} = atmospheric pressure (lb/ft^2)
P = manifold interior pressure (lbf/ft^2)
g = gravitational constant (ft/s^2)
x = coordinate direction of manifold axis (ft).

With axially uniform inflow, the rate of change of manifold downflow with distance, $\frac{dw}{dx}$, is constant and equal to the total receiver flow divided by the manifold length (L):

$$\frac{dw}{dx} = \frac{-w_t}{L} \tag{6.3}$$

By combining this condition with the two previous relations, a differential equation can be derived which specifies the axial orifice area variation necessary for providing axially uniform inflow:

$$\frac{da}{dx} - \frac{16\ L\ (1 - 1/Lx)}{\pi^2 D^4}\ c^2 a^3 = 0 \tag{6.4}$$

This equation can be converted into a more useful form by substituting an expression for the fraction of total manifold surface area open to flow, $\bar{f}$ (orifice area divided by manifold area). The equation then takes the form

$$\bar{f} = \frac{a}{\pi D},\quad \frac{d\bar{f}}{dx} - \frac{16\ (L - x)}{D^2}\ c^2\ \bar{f}^3 = 0 \tag{6.5}$$

which can be converted into numerical form and solved on a computer by specifying the open area fraction at the top of the manifold. This value is governed by manifold structural considerations.

6.1.2 Air Flow Distribution TEMPEST Model

To verify the computed orifice configuration and also determine receiver pressure drop, a receiver model was developed using the PNL-developed code, TEMPEST. TEMPEST is a hydrothermal computer program designed to analyze a broad range of coupled fluid dynamic and heat transfer problems. TEMPEST uses the full three-dimensional, time-dependent equations of continuity, motion, and heat transport to calculate the velocity, pressure, and temperature fields for either laminar or turbulent fluid-flow situations.

The TEMPEST model used is a representation in cylindrical coordinates of the receiver and the atmosphere immediately surrounding it. Figure 6.1 shows the model in a half plane view along the axial direction. The model possesses 21 radial nodes, 26 axial nodes, and one circumferential node. The model uses

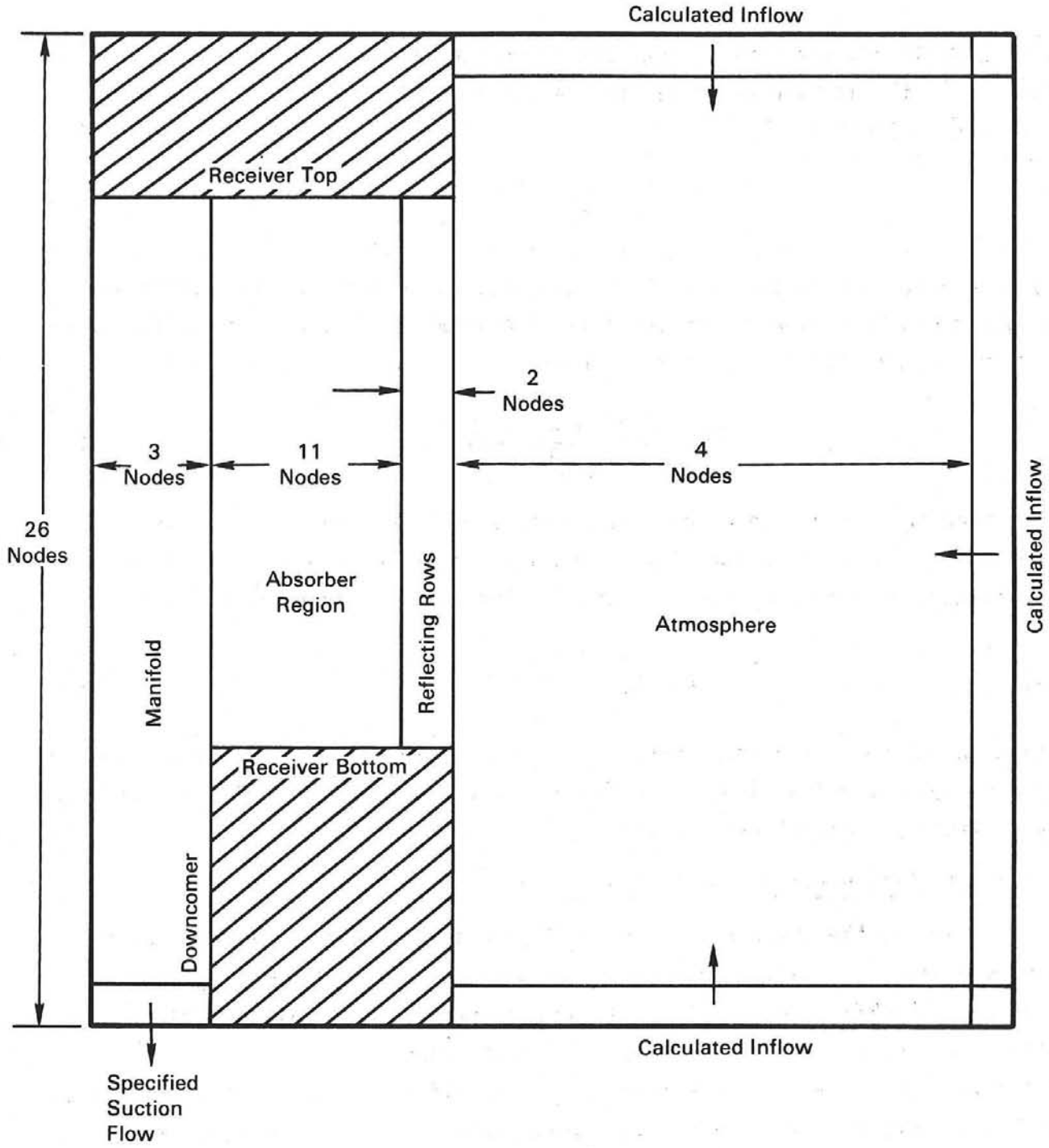

FIGURE 6.1. Volumetric Receiver Air Flow Distribution - TEMPEST Model

three radial nodes to model the manifold and downcomer, eight radial nodes for the absorber structure and reflecting zone, and four radial nodes in the atmosphere immediately surrounding the receiver. In the axial direction, the receiver has 16 nodes, with an additional six nodes modeling the upper portion of the downcomer.

Suction flow through the receiver is simulated by specifying a negative flow velocity at the bottom downcomer cells. This velocity is based on a 50-MWt receiver with air leaving at 2000°F through a downcomer of specified diameter. Air flowing through the receiver is assumed to move only in the radial and axial directions. TEMPEST is not able to treat rotational air flow, so designs where the air does have a tangential velocity component cannot be rigorously modeled. It is assumed that an orificed manifold which gives an even inflow for no air rotation will perform identically in situations where the air is rotating. Similarly, the receiver pressure drop calculated for the nonrotational case is considered equivalent to that for the rotational case.

Flow resistance caused by receiver internals is modeled by the specification of drag coefficients on both the radial and axial node faces. Loss coefficients added to the outer manifold node are used to simulate orifices in the manifold. The orifice area fraction distribution calculated for the manifold is converted to a loss coefficient distribution and input to the model. This is done by combining the orifice Equation (6.7) with the pressure drop formulation Equation (6.7) used in TEMPEST:

$$\frac{dw}{dx} = c\sqrt{2g\,\rho\,(P_{atm} - P)} \quad \bar{f}\pi D = \frac{-w_t}{L} \tag{6.6}$$

$$P_{atm} - P = \frac{1}{2} K\,\rho\,\frac{V^2}{g} \tag{6.7}$$

where V = free stream inflow velocity

K = loss coefficient

Using the fact that the inflow velocity, V, is uniform and equal to:

$$V = \frac{w_t}{\pi D L \rho} \tag{6.8}$$

an expression for the loss coefficient as a function of the fraction of orifice area and the single hole orifice coefficient can be derived:

$$K = \left(\frac{1}{c\bar{f}}\right)^2 \tag{6.9}$$

No heat generation in the receiver is assumed during model runs. Air is drawn through the receiver isothermally at a temperature of 2000°F. This is done for three reasons. First, this assumption maximizes the air flow velocity in the receiver and results in a conservative estimation of the receiver pressure drop. Secondly, it has no effect on the function of the manifold because in the real case the air has already been heated to this temperature before it reaches the manifold. Finally, this assumption allows the model runs to be performed faster and much more cheaply.

The distribution of air flow in the receiver predicted by the model with the calculated manifold orifices is still not uniform. The reason for this is the difference in order between the orifice distribution calculation and the calculation performed by TEMPEST. While the orifice distribution calculation is essentially a one-dimensional treatment of receiver flow, TEMPEST handles it in a full three-dimensional manner. To upgrade the orifice distribution calculation to account for multi-dimensional effects is impractical. Therefore, the approach taken is to use the manifold interior pressure distribution calculated in the first model run to back-calculate a new loss coefficient distribution that will result in uniform inflow. On incorporation of this revised distribution into the model, the calculated inflow distribution becomes uniform to within ±3%. Orifice area fractions are derived from this successful loss coefficient distribution.

Receiver pressure drop is determined from the same run by subtracting the interior pressure at the bottom of the manifold from the atmospheric pressure.

6.2 TANGENTIAL AIR FLOW ANALYSIS

In some receiver designs, the radial inflow of air by itself is not sufficient to cool the receiver interior. In such designs, additional cooling is provided by establishing a relative velocity between the air and the absorber structure in the tangential (rotational) direction. This can be done in two ways. The first design, the rotating fiber bed (RFB), creates this relative velocity by rotating the absorber structure (fiber bed) through the inflowing air. In the stationary fiber bed (SFB) design, the fiber bed is stationary and the incoming air is given a rotational component (preswirl) which creates the relative velocity as the air is drawn into the receiver.

In both designs, the presence of the fiber bed acts to reduce the relative velocity and, consequently, the convective heat transfer coefficient. The rotating fibers in the RFB tend to drag air along with them, creating a rotational air velocity in the same direction as the fibers are traveling. Similarly, in the SFB design the drag of the fibers acts to slow down the rotational component of the inflowing air. Two other effects, the thermal expansion of the air as it is heated and the conservation of angular momentum, act to speed up the rotation of the air as it is drawn into the receiver. This is good from the standpoint of the SFB but bad for the RFB.

In analyzing the air flow in these designs, it is important to insure that the relative velocity between the air and fibers is large enough throughout the receiver to maintain an adequate heat transfer coefficient. For the RFB design, this requires the rotational component of the air flow to be small in relation to the fiber rotation. Conversely, it is desirable to have the rotational velocity of the air to be as large as possible in the SFB design. At the same time, however, it is necessary to show that the combined effects of thermal expansion and conservation of angular momentum do not create a maelstrom in the interior of the receiver. This could create structural problems caused by excessive loadings on receiver internals.

As stated previously, TEMPEST does not have the capability for modeling this kind of flow situation. A new computer routine, VORTEX, was created to enable analysis of this type of air flow. VORTEX makes use of the cylindrical

coordinate form of the Navier-Stokes equations to describe the flow in the receiver. Some simplifying assumptions are made to the equations to enable their solution:

- Axially uniform inflow allows a two-dimensional treatment of the flow in the r-θ plane.
- Flow is steady-state.
- Flow is inviscid.
- There is no pressure gradient in the tangential direction; driving or retarding force is the drag of fibers.
- Fiber drag is considered a body force (distributed uniformly over given volume).
- Radial or tangential flow velocities (u or v) do not vary in tangential direction (axisymmetric flow).

The equations then reduce to:

$$\frac{1}{r}\frac{\partial}{\partial r}(rU \cdot \rho U) - \rho\frac{V_t^2}{r} = \frac{-\partial p}{\partial r} \qquad \text{radial direction} \qquad (6.10)$$

$$\frac{1}{r}\frac{\partial}{\partial r}(rU \cdot \rho V_t) + \rho\frac{UV_t}{r} = \text{fiber drag force} \qquad \text{tangential direction} \qquad (6.11)$$

$$\text{fiber drag force} = \frac{1}{2} C_D \rho \left[U^2 + (V_f - V_t)^2\right]^{1/2} (V_f - V_t) \frac{N_f A_f}{V_z} \qquad (6.12)$$

where U = radial air velocity (ft/sec)
V_t = tangential air velocity (ft/sec)
C_D = fiber drag coefficient
V_f = fiber tangential velocity (ft/sec)
N_f = number of fibers in zone
A_f = cross sectional area of a fiber (ft^2)
V_z = volume of zone (ft^3)
ρ = air density (lbm/ft^3)

With the assumption of uniform inflow, the radial flow velocity can be found from continuity and is:

$$U = - \frac{w_t}{2\pi r L \rho} \tag{6.13}$$

Substituting this into the tangential equation of motion gives:

$$\frac{dV}{dr} + \frac{1}{\rho}\frac{d\rho}{dr} V_t + \frac{1}{r} V_t = - \frac{1}{2} C_D \rho \left[U^2 + (V_f - V_t)^2\right]^{1/2} (V_f - V_t) \frac{N_f A_f}{V_z} \frac{2\pi r}{w_t} \tag{6.14}$$

Since the velocity of interest is the relative velocity between air and fiber, we make the following substitution:

$$\Delta V = V_f - V_t = 2\pi w_f r - V_t \tag{6.15}$$

where w_f is the fiber angular velocity (rad/sec).

This gives:

$$\frac{d\Delta V}{dr} + \left[\frac{1}{\rho}\frac{d\rho}{dr} + \frac{1}{r} - \frac{1}{2} C_D \rho \left(U^2 + \Delta V^2\right)^{1/2} \frac{N_f A_f}{V_z} \frac{2\pi r}{w_t}\right] \Delta V = 2\pi w_f \left[2 + \frac{r}{\rho}\frac{dP}{dr}\right] \tag{6.16}$$

which is the governing equation of flow for the fiber bed designs. In VORTEX, this equation is converted to finite-difference form and solved from the receiver surface to the inlet manifold.

The receiver is divided into a number of radial zones that can represent an area of the fiber bed, a reflecting row, or a dead zone (free space). Within each zone, the distribution of heat generation and fiber distribution (if any) is considered uniform. VORTEX divides each zone into a user-specified number of nodes for solution purposes. VORTEX requires specification of

receiver characteristics, zone characteristics, and boundary conditions to complete the calculation. These specifications are:

Receiver characteristics

- total air mass flow rate
- receiver height
- fiber area

Zone Characteristics

- heat generation rate (from receiver performance simulation)
- zone radial width
- number of fibers
- rotation speed
- drag coefficient of fibers (value for cylinder in turbulent cross flow)
- number of computational nodes

Boundary Conditions

- receiver outer radius
- air inlet temperature
- air inlet density
- initial tangential velocity.

VORTEX first makes use of continuity and a steady-state heat balance to calculate the radial flow velocity, temperature, and density of the air at each point in the receiver. Using this information along with the input conditions, it then repeatedly solves the governing equation of motion at each point in the receiver, starting at the receiver periphery and marching inwards, to give the distribution of relative velocity.

6.3 RECEIVER CONVECTIVE LOSS

Calculations of the convective losses from the volumetric receiver are accomplished using TEMPEST. Only the designs which have an outer reflecting wedge row (or "light valve") are considered. No convective loss calculations are performed for the shrouded designs.

The "light valve" concept is used in the volumetric receiver as a means of reducing reradiation losses. However, the reflecting wedges (light-valve) introduce their own loss mechanism. Since the wedges are not perfectly reflective, they will absorb a portion of the incoming energy flux and will heat above ambient conditions. The temperature difference between the reflecting wedges and the air will induce natural convection. If the air velocities due to natural convection are large compared to the inflow velocity, a significant percentage of the energy absorbed by the wedges could be lost to the surroundings. TEMPEST is employed to ascertain thermal energy loss caused by natural convection over the reflecting wedges.

The TEMPEST model used to perform the analysis is shown in Figure 6.2. It is a three-dimensional cartesian representation of one-half of a single reflecting wedge, the dead zone between it and the fiber bed, the volume of air to which its large face transfers heat, and the atmosphere outside it. The model has an axial extent of 17 nodes, a width of 11 nodes wide, and a depth of 8 nodes. The half-wedge is treated with 180 solid material cells having the thermal properties of aluminum. Since the wedge face does not lie in one of the coordinate planes, it must be approximated in a "stair-step" fashion as shown in the figure. The wedge cells generate heat at a uniform volumetric rate determined from the results of a receiver performance simulation.

To model heat transfer from the wedge to the air, values for the heat transfer coefficient are input for the solid cell faces in contact with the air cells. These heat transfer coefficients are determined empirically using the following relations:

forced convection $$Nu_L = 0.654\ (Re_L)^{0.5} \tag{6.17}$$

natural convection $$Nu_H = 0.098\ (Gr_H)^{0.333} \left(\frac{T_{surf}}{T_{air}}\right)^{-0.14} \tag{6.18}$$

mixed convection $$h_{mix} = [(h_{fc})^{3.2} + (h_{nc})^{3.2}]^{1/3.2} \tag{6.19}$$

where Re = Reynolds number

Gr = Grashof number

T_{surf} = Surface temperature

T_{air} = Bulk air temperature

Nu = Nusselt number

h = Convective heat transfer coefficient

H = Receiver height

L = Wedge length.

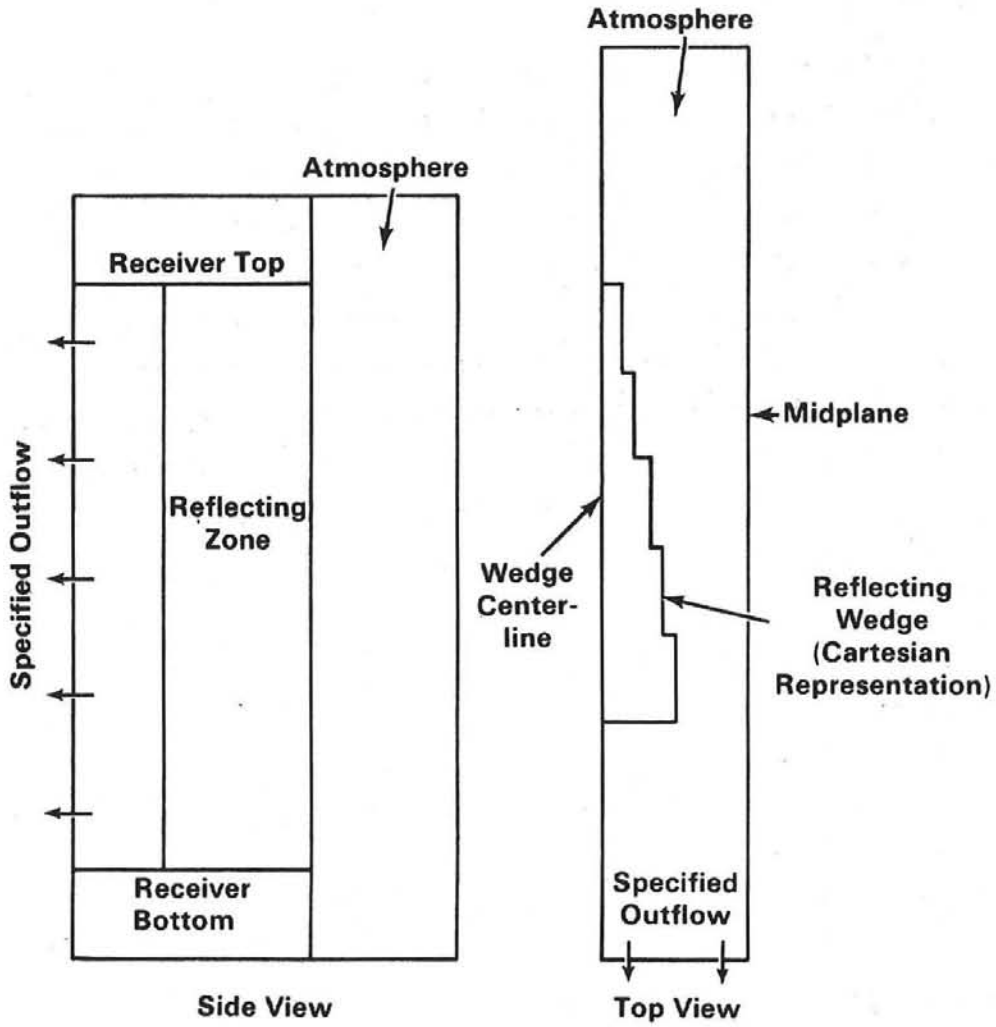

FIGURE 6.2. Volumetric Receiver Convective Loss - TEMPEST Model (not to scale)

Air properties are evaluated at the bulk air temperature for the reflecting zone calculated by the receiver performance simulation. Longitudinal (inflow) air velocity over the wedge face necessary for calculation of the forced convection heat transfer component is determined from continuity. The temperature difference between the wedges and air, as calculated by the performance simulation, is used in finding the natural convection component. A uniform velocity outflow boundary condition at the edge of the dead zone (beginning of the fiber bed) is specified to simulate uniform inflow to the receiver. Also, a computed inflow/outflow boundary condition is used at the edge of the atmosphere cells.

Convective loss from the receiver is determined from the model output by examining the air velocity distribution crossing the plane representing the receiver surface (plane normal to wedge tip). The cells with a negative flow velocity normal to this plane represent regions where convective loss is occurring. The net heat transport into the ambient is calculated from these outflow velocities and the corresponding air temperature. This value is then multiplied by the total number of half-wedges (twice the total number of wedges) to determine the total receiver convective loss.

7.0 CONVECTIVE HEAT TRANSFER MODELING

The initial emphasis of the convective heat transfer investigation was directed toward the array of staggered fins within the volumetric receiver and vertical reflecting wedges around its periphery. As the development of the configuration progressed, the density of the array had to be reduced to allow penetration of the radiant energy further into the interior. This resulted in less surface area for convective heat transfer, and the possibility of incorporating enhanced heat transfer from the fins became very important. The conversion from the staggered-fin and radial-fin configurations to the fiber-array arrangement was necessitated by the decision that convective heat transfer of the former two configurations was too low to adequately cool the surfaces. Consequently, the emphasis shifted to understanding convective heat transfer from thin fibers.

The specific correlations used in the calculations are provided in Section 8. The rationale for the selection of these correlations is described here.

7.1 CONVECTIVE HEAT TRANSFER FROM FIN SURFACES

The large and complex geometries in the VAHR, the high temperatures, and the large differences in local velocities presented problems in selecting satisfactory models for the heat transfer computations because neither natural nor forced convection is dominant in all regions of the receiver. Even considering only forced convection, a single correlation cannot cover all regions of the receiver. The outer region, consisting of reflecting rows in the original configuration, and the outermost absorbing row could be modeled as flat vertical plates. The rest of the absorbing rows should be modeled as two vertical flat surfaces with staggered horizontal flat plates (normal to the vector of the induced flow) extending from one vertical surface to the other. However, no correlation was found in the literature to describe the heat transfer performance of this type of geometry.

The modeling of natural convection from the surfaces in the absorbing region would logically require the identification of a characteristic length

for a vertical flat surface that is longer than the spacing between the horizontal surfaces. A method of selecting this longer characteristic length has not been identified yet, and no data were available on the effect of the horizontal plate fins in the natural convective heat transfer.

Most of the correlations for both forced and natural convection were derived from data that were taken at temperatures lower than those expected to be present in the VAHR. Also, the hydraulic diameter of a typical flow channel in the VAHR is much larger than the diameter of the test sections used to obtain the data.

7.1.1 Forced Convection Heat Transfer

For the absorbing region of the receiver, the closest representations for which data were available were compact heat exchangers with staggered plates and staggered cylinders. The former configuration was motivated by the analysis of compact heat exchangers, and consequently, the hydraulic radius of the test sections were very much smaller than in the VAHR. However, the range of conditions of the other physical parameters, both for the solid surface and the flowing gas, were close to the range of interest. Another family of correlations that could be applied to this problem was for staggered arrays of cylinders in crossflow. A typical calculation of the heat transfer coefficient as a function of linear velocity for the VAHR using a number of these correlations gave a significant variation (a factor of approximately 3) between the highest and lowest values for the outer rows of absorbing pins. An empirical expression developed by Weiting (1975) was recommended because it included the greatest sensitivity to configuration parameters. This correlation is of the form

$$\frac{h}{\rho V_\infty C_p} = \beta\left(\frac{L}{D_h}\right)^b (\alpha)^c (Re)^d (Pr)^e \qquad (7.1)$$

where D_h = hydraulic diameter
α = height/width ratio of the free-flow area
L = distance from the front of the plate
V_∞ = free-stream velocity
Re = Reynolds number
Pr = Prandtl number.

The forced convection expression for the row of reflecting plates was calculated from the classic solution of developing boundary layers (the Pohlhausen solution) (Kays and Crawford 1980).

$$Nu = \frac{hL}{k} = 0.644 \left(\frac{LV_\infty}{\nu}\right)^{1/2} \left(\frac{C_p \mu}{k}\right)^{1/3} \qquad (7.2)$$

7.1.2 Natural Convection

Many of the correlations for natural convective heat transfer in the literature for staggered arrays of parallel plates were derived for plates that were parallel to the direction of the buoyancy forces. In the absorbing region of the VAHR, the horizontal plates are perpendicular to the direction of buoyancy-induced flows. Essentially all of these correlations have the general form of

$$Nu = a(Gr)^n \qquad (7.3)$$

where $Gr = \frac{g\beta y^3}{\nu^2} (T_{surf} - T_{bulk})$
a = constant
n = 1/3 for transition flow, $Gr > 10^{10}$
1/4 for laminar flow.

Thus, the characteristic length L has a very significant impact on the convective coefficient calculated from these correlations. For the VAHR configuration, it is not immediately obvious what is the appropriate characteristic length. The length not only directly affects the calculated coefficient,

but also determines the point at which the boundary layer changes from laminar to turbulent (and the recommended correlation changes).

Much of the natural convection data was obtained at cryogenic temperatures, which makes their applicability uncertain.

The correlation selected was that by Siebers, Schwind, and Moffat (1983), which was based on data collected at temperatures reasonably close to the VAHR operating conditions and on using air as the heat transfer fluid.

7.1.3 Mixed-Mode Heat Transfer

The most straightforward approach to the correlation of mixed-mode convection is to combine the values of the heat transfer coefficients calculated independently for the natural and forced convection mechanics using the equation

$$h_m = [(h_f)^a + (h_n)]^{1/a} \qquad (7.4)$$

where h_m = mixed-convection heat transfer coefficient
h_f = forced-convection heat transfer coefficient
h_n = natural-convection heat transfer coefficient
a = arbitrary constant.

Several different authors have suggested different values for the exponent a in the above equation. Most estimates range from a value of 2.0 to 3.2. Siebers, Schwind, and Moffat (1983) recommend using a value of 3.2, based upon the data they gathered for a vertical surface in crossflow.

7.2 ENHANCED HEAT TRANSFER FROM FINS

Since the initial analysis of the convective heat transfer for both the staggered- and radial-fin configurations gave low values of the heat transfer coefficient (ranging from 1.1 to 3.0 btu/hr-ft^2-°F), some form of heat transfer enhancement was needed. Various methods to enhance forced-convection heat transfer have been reported in the literature. Those chosen for their suitability in the present application are basically of the type where some form of

surface interruption is used. The use of periodic interruptions to a plate wall restricts the development of a thick boundary layer, and the higher heat transfer coefficient associated with developing flow is obtained. A summary of the possible techniques is reported in Table 7.1.

In general, the enhancement is greatest in the turbulent and transition regimes, with transition typically occurring at a Reynolds number (based on the hydraulic diameter) of about 1,000. The range of Reynolds numbers for flow into the VAHR, based on channel width for the radial-fin configurations, is expected to be on the order of 10^3 to 10^4. The effect of accelerating flow, as the air moves inward along a radius, will be to increase the stability of the flow and reduce the enhancement effects.

TABLE 7.1. Summary of Enhancement Techniques for Fin Designs

Reference	Flow Description	Characteristic	Enhancement Achieved
Sparrow et al. (1977)	Interrupted Wall Channels	Laminar (Re: 200-1600)	~60-80%
Cur & Sparrow (1979)	Interrupted Wall	Turbulent Fully Developed (Re: $>10^4$)	2
Yang (1983)	Interrupted Compact Surfaces	"2nd Laminar Flow Regime" ($Re_{C1} < Re < Re_{C2}$)	~80-100%
Tanasawa et al. (1983)	Rib-Type Turbulence Promoters	Re: (1.3×10^4-1.5×10^5)	~1.6-1.9
Shah (1975)	Perforated Surfaces	Laminar (Re < 1000) Transition/Turbulent	None ~2 - 3
Lee & Yang (1978)	Perforated Surfaces	2nd Laminar Flow Higher Flow Range	~1.5 - 2 ~3
Liang & Yang (1975)	Perforated Surfaces	Re: (3×10^3 - 2×10^4)	~2 - 3

One flow regime of interest is the "second laminar flow" regime, which is found to exist for all plate surfaces with fins for interrupting the boundary layer. In this regime, enhancement is caused by the self-sustaining flow oscillations that are produced in the boundary layer. Operations in this regime may be of interest because significant heat transfer enhancement may be obtained while avoiding the vibration and noise in the transition and turbulent regimes.

A rough summary of the conclusions to be drawn from Table 7.1 is that: 1) in the "pure" laminar regime, very little (if any) enhancement is expected; 2) in the "second-laminar" regime, enhancements of 80 to 100% may be obtained; 3) in the turbulent regime, enhancements of 2 to 3 times normal may be expected.

The results indicate that, given the anticipated velocities of the VAHR, even enhancement would not be sufficient to yield a plausible fin design. Moreover, the impact of any type of enhancement on the absorption characteristics or, more fundamentally, on the absorption area - at least in the case of perforated surfaces - introduced further questions and lowered the incentive for proceeding in this direction.

7.3 CONVECTIVE HEAT TRANSFER FROM CYLINDERS

The evolution and design of a fiber packing for the volumetric receiver was largely motivated by higher convective heat transfer from cylinders of small diameter. An extensive review of literature has been made by Morgan (1975). The degree of assurance in the design of heat transfer from cylinders is considerably greater than that from staggered fins.

7.3.1 Forced Convective Heat Transfer

A considerable amount of experimental data is available; some of the data are for conditions similar to that anticipated in the VAHR. The primary uncertainty in the experimental value of a forced convection coefficient lies in isolating the coefficient from contributions of natural convection and radiation, and from the possible effects of free-stream turbulence and partial

blockage in the test section. Nevertheless, the available correlations do not show a wide degree of scattering for the conditions of interest.

7.3.2 Natural Convection

Natural convection is much greater in the horizontal mode than in the vertical. As the slope of the test section is increased from 0 to 45°, the natural convective heat transfer will drop about 10%. As the test section is moved to vertical, the coefficient may drop to a value of only 30% of that in the horizontal position because the boundary layer thickens as the convective flow moves up over the vertical surface. Also of concern is whether the characteristic length, fundamental to the evaluation of the Grashof number, is well understood. If small perturbations in the surface could cause separation of the boundary layer, they would affect the thickness of the boundary layer and, by inference, the characteristic length of the surface.

7.3.3 Combined Forced and Natural Convection

In the past there has been confusion over how to calculate the Nusselt number when both natural and forced modes of convection are present. Some workers have suggested that the heat transfer coefficients be calculated separately and the higher value used. Others have suggested that the vectorial sum of the Nusselt numbers of the two modes be used. However, both of these methods can result in considerable error, and approaches based on the resultant flow velocity have led to greater success. Morgan (1975) gives a detailed treatment of this approach, which results in an expression for the combined heat transfer coefficient similar to that expressed for flat plates.

8.0 THERMAL PERFORMANCE MODELING

The thermal performance model incorporates the results of the radiation heat transfer study, the convective heat transfer study, and the air flow study in a model that determines the thermal performance of a volumetric receiver design. The primary results from the performance model are the equilibrium temperatures of the receiver surfaces. This information can then be used to calculate important thermal performance results, such as air temperature, reradiation losses, and flux ratio. Section 8.1 provides an overview of the model and describes key modeling assumptions. Section 8.2 discusses the reasons for selecting a transient model, while Section 8.3 describes the details of the transient model. Sections 8.4 through 8.6 describe specific features of the transient model, which include radiation heat transfer, drag and convection, and shroud performance. Section 8.7 discusses the type of results obtained, and Section 8.8 describes the model verification.

8.1 RECEIVER ARRANGEMENT AND ASSUMPTIONS

To simplify the analysis, the volumetric receiver is divided into a number of two-dimensional concentric cylindrical zones (axial variations of energy and fluid flow are neglected). Each zone is assumed to be isothermal with all solid surfaces having the same temperature. The zone arrangement and indexing scheme is shown in Figure 8.1. A receiver with n zones has the surroundings as zone 0 with the first receiver zone being zone 1. The terminal absorber is zone n. If either a reflecting zone or a shroud is included, it would be designated zone 1 with the first absorbing zone being zone 2. Previous investigations (Drost and Eyler 1981) indicated that increasing the number of zones improves receiver performance, but that the impact decreases as more zones are considered until there is negligible impact for adding any more zones. This point occurs at about ten zones; therefore all designs were modeled with at least ten zones.

The arrangement of the receiver in concentric cylindrical zones is based on the assumptions of uniform insolation and air flow in the vertical and circumferential directions. The consideration of radiation flux variations in

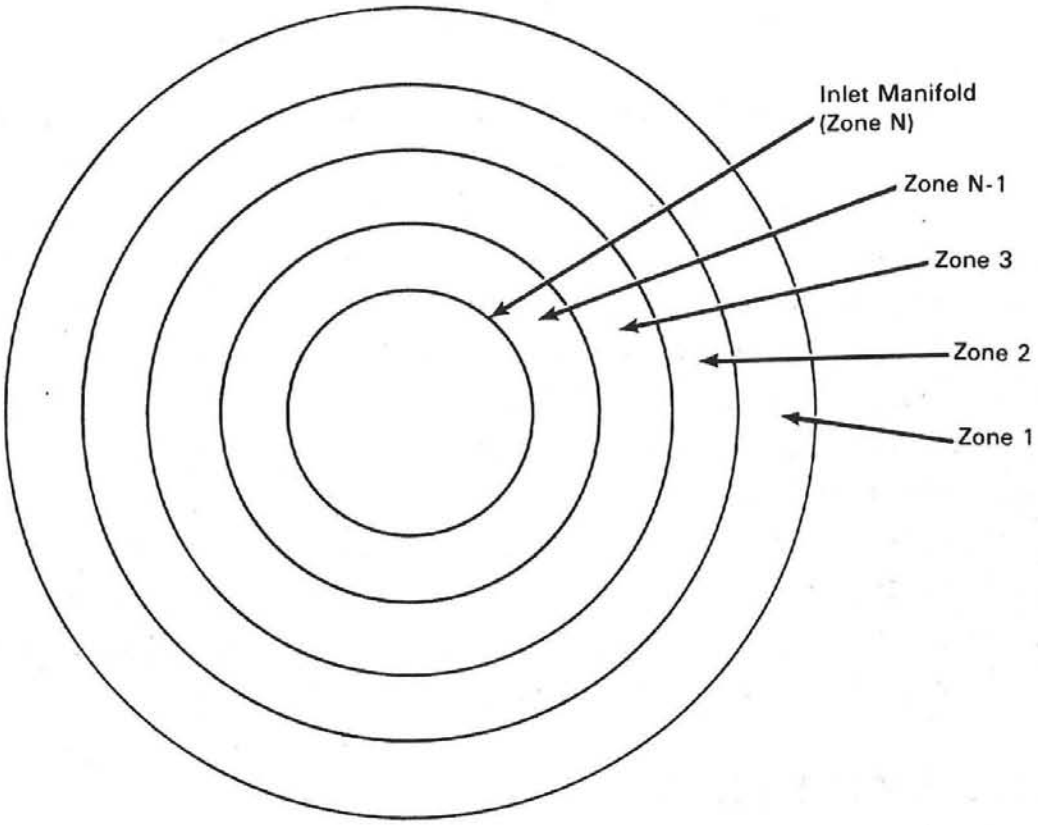

FIGURE 8.1. Receiver Zone Arrangement

either direction would have involved a large number of zones, requiring a very large number of exchange factors. Generating such a large number of exchange factors using the Monte Carlo technique would have been prohibitively expensive. Instead, these assumptions were made to simplify the analysis. The assumption of uniform air flow may be reasonable because the air flow analysis has shown that there is substantial flexibility in distributing air flow. The assumption of uniform flux is not realistic, considering that surround heliostat fields have a distinct asymmetry, with the majority of mirrors north of the receiver. However, the resources were not available to provide that level of detail for the modeling effort. The model does predict the maximum flux maldistribution that can be tolerated without exceeding material temperature limits. In many zones, the local flux could be 2 to 3 times the average flux without exceeding the material temperatures limits.

A second set of assumptions involves surface emissivity, which is used in determining exchange factors, and maximum material temperature, which is used for calculating the flux ratio. The assumed material properties for various surfaces are given in Table 8.1.

8.2 GENERAL APPROACH

The main problem in modeling the volumetric receiver thermal performance is determining the equilibrium temperatures of the various receiver surfaces while they are exchanging radiant energy (with other receiver surfaces and the surroundings) and convecting energy to the flowing air. Two numerical approaches were tried: a steady-state approach and a transient approach. The steady-state approach was similar to an "iterative" method of solving second-order partial differential equations. Zone material temperatures were assumed, and the convection and radiation heat transfer was determined, allowing the calculation of a new zone temperature. This procedure was continued until the zone temperatures converged. Unfortunately, this approach proved to be unstable for many cases of interest, so the transient approach was considered. This approach consisted of having the receiver at an initial temperature and allowing the receiver surfaces to increase in temperature as solar radiation is absorbed until the receiver surface reaches a steady-state temperature. At this point the insolation striking a surface just equals the net radiation heat

TABLE 8.1. Material Properties

Zone Type	Material	Emissivity and Absorptivity	Maximum Temperature, K
Reflecting zone	Aluminum	0.2	645.0
Shroud	Insulated refractory	1.0	1800.0
Fiber zone	Nextel® 312	0.9	1480.0
Fin zone	Silicon carbide	0.8	1590.0
Terminal absorber	Silicon carbide	0.8	1590.0

® Registered trademark of the 3M Corporation.

transfer and convection from the surface to the air. By including a variable fictitious thermal inertia or time step, the stability of the transient approach could be insured.

8.3 TRANSIENT MODEL

The transient approach consists of letting a receiver at some initial temperature increase in temperature until the receiver reaches an equilibrium steady-state temperature distribution. By conducting an energy balance on zone i we get

$$\frac{dT_i}{dt} = \frac{Q_i(T)}{\dot{m}_i C_{pi}} \tag{8.1}$$

where Q_i consists of both a convection and radiation component in addition to insolation and is given by Equation (8.2).

$$Q_i = -A_i \varepsilon_i \sigma T_i^4 - \sum_{j=0}^{n}\left[B_{ij} \sigma T_j^4\right] - h_i A_i (T_i - T_{a_i}) + Q_{ins_i} \tag{8.2}$$

Equation (8.1) was solved numerically using an Euler method resulting in Equation (8.3).

$$T_{i_{n-1}} = \frac{Q_i (T_n)}{\dot{m}_i C_{pi}} \Delta t + T_{i_n} \tag{8.3}$$

Unlike most transient solutions, we are not interested in the time-dependent solution but in the steady-state solution; therefore the actual values used for Δt and $m_i C_{pi}$ are not important as long as the numerical scheme is stable and does not require an excessive amount of computer time. For our purposes Δt was assumed to be 1 and was not explicitly included in the calculation. A value of $\dot{m}C_p$ was included and represented the variable that could be adjusted to insure convergence of zone temperature. Increasing the thermal mass improves stability but increases the computer time required for convergence.

The performance analysis is conducted for a receiver producing hot air with a specified exit temperature. The convergence of zone temperatures does not insure that the actual product temperature will equal the design temperature; therefore, the zone temperature convergence procedure must be nested in a procedure that converges on the design product temperature. This approach starts with an assumed amount of energy incident on the receiver (receiver power level). The transient simulation is conducted until steady-state temperature conditions are reached and the product temperature is compared to the design temperature. A new value for incident energy on the receiver is selected if the calculated and design temperatures have not converged, and the process is repeated.

Given an assumed power level and initial temperature, the computational procedure consists of simulating a large number of time steps. This is continued until receiver temperatures converge. The most important computational procedure is the determination of the receiver temperature distribution at the end of a time step, given the temperature distribution at the beginning of the time step. The calculations for time step j starts with the zone and air temperatures known from time step j-1. The numerical scheme consists of five steps:

Step 1 - The insolation added to each zone and reflection losses are calculated based on the insolation distribution from the Monte Carlo radiation model and the current power level.

Step 2 - Based on the j-1 zone temperatures, the net radiation heat transfer between zones is calculated (see Section 8.3).

Step 3 - Based on the j-1 zone and air temperatures, the air temperature at time step j is calculated using Equation (8.4).

$$T_{a_j} = T_j + T_{a_{j-1}} - T_j \exp\left[\frac{-(h_{j-1})A}{\dot{m}_i C_{p_A}}\right] \qquad (8.4)$$

Step 4 - Once the zone and air temperatures are known, the energy convected from the zone to the air can be calculated by conducting an energy balance on the air.

Step 5 - The new zone temperature is determined using Equation (8.3).

Step 6 - The zone temperature convergence is checked and iteration is terminated if the zone temperatures converge; otherwise steps 1 through 6 are repeated until the temperatures converge.

The receiver is assumed to initially be at the temperature of the surroundings, which is assumed to be at 294 K. This value is also assumed for both the air inlet temperature and the "sky" temperature used for calculating reradiation losses.

8.4 RADIATION HEAT TRANSFER

The performance model takes the zone temperatures and determines the radiation heat transfer between zones. This is done using exchange factors supplied by the Monte Carlo radiation simulations.

8.4.1 Definition of Exchange Factor

The Monte Carlo radiation heat transfer model gives an exchange factor for energy transfer between two surfaces. Of the total number of energy bundles emitted by one surface, the fraction that is incident on a second surface is the exchange factor (Howell 1968, p. 21). Toor and Viskanta (1967) define an absorption factor between finite surfaces i and j. The absorption factor is given in Equation (8.5).

$$F_{ij} = \lim_{N_i \to \infty} \left(N_{i-j}/N_i \right) \tag{8.5}$$

N_{i-j} represents the number of photon bundles emitted by surface i absorbed at surface j. Based on a comparison of the Monte Carlo algorithms used by Howell and by Toor and Viskanta, it appears that Howell's exchange factor is the same quantity as the absorption factor of Toor and Viskanta . In this paper the term "exchange factor" will refer to F_{ij} as defined in Equation (8.5). It should be noted that the exchange factor is related to the "Hottel Script F" by Equation (8.6) (Toor and Viskanta 1967).

$$F_{ij} = \varepsilon_i \, B_{ij} \tag{8.6}$$

The net radiation heat transfer rate for a given surface can be calculated by conducting an energy balance on the surface as presented in Equation (8.7).

$$Q_i = A_i \, \varepsilon_i \, \sigma T_i^4 - A_i \sum_{j=1}^{n} B_{ij} \left(\sigma \, T_j^4 - \frac{Q_i (1-\varepsilon_j)}{A_j \, \varepsilon_j} \right) \tag{8.7}$$

Toor and Viskanta (1967) give the reciprocity conditions for the exchange factors as

$$A_i \, \varepsilon_i \, B_{ij} = A_j \, \varepsilon_j \, B_{ji} \tag{8.8}$$

8.4.2 Exchange Factor Processing

The exchange factors calculated in the Monte Carlo model are statistical and only approximate the true result. The stability of the transient solution for the equilibrium temperature distribution depends on reciprocity being maintained between surfaces and on the summation of exchange factors equalling 1.0. Because of the statistical nature of the Monte Carlo results, random variations may result in reciprocity, as defined in Equation (8.8), not being maintained.

To insure that reciprocity is maintained, the exchange factors are processed. Processing consists of assuming that the exchange factors in the outward direction are valid. An exchange factor in the outward direction is an exchange factor between an interior zone and a zone located closer to the external surface of the receiver. The reciprocity relation (Equation 8.8) is then used to calculate the exchange factors in the interior direction. The exchange factor from a zone to itself is calculated by summing the exchange factors to all other zones and subtracting from 1.0.

The processed exchange factors were compared to the unprocessed exchange factors for several cases, and the results indicated that processing had a negligible impact on the exchange factor values.

8.4.3 Calculation of Radiation Heat Transfer

With the exchange factors known, the radiation heat transfer between zones can be calculated for each time step. At the start of a time step, the zone temperatures are known. After use of Equation (8.7) for each zone, the net radiation heat transfer to each zone can be calculated. The net radiation heat transfer to the surroundings (Zone 0) is the reradiation loss.

Care must be taken in calculating the proper zone area for each zone. In general the area is the surface area of either all the fins or all the fibers in a zone. The interior zone, or terminal absorber, is modeled as emitting only in the outward direction; therefore the surface area should be only the area of the external surface of the terminal absorber.

The key assumptions in the radiation heat transfer calculation have been discussed earlier. One additional assumption relates to the performance modeling, the assumption that the exchange factors are independent of surface temperatures. The exchange factors are a function of surface geometry and optical properties. Optical properties such as emissivity, absorptivity and reflectivity are, in general, a function of temperature; therefore the exchange factors should, in general, be a function of temperature. However, the computational resources required to run the Monte Carlo simulation for each time step would be excessive with this added complexity. In addition, all surfaces except the reflecting zone surfaces were already high-emissivity surfaces, and any increase in emissivity due to a temperature rise would result in a small percentage change in the emissivity. Also, an increase in surface emissivity is desirable because the reduction in reflection losses normally exceeds the increased reradiation. Therefore, using a constant emissivity based on low temperature data should yield conservative results. The reflecting zones are a major exception because the attractiveness of the concept depends on maintaining a low emissivity in the reflecting zone. Reflecting zone designs, however, were unattractive even using optimistic optical properties (see Section 9.4). Considering temperature-dependent optical properties would only make the unattractive reflecting zone concept look worse.

8.5 CONVECTIVE HEAT TRANSFER AND DRAG

The performance model includes algorithms for determining the convective heat transfer between the receiver surfaces and the air. It also predicts the power required to turn the rotating section of the rotating fiber designs.

8.5.1 Relative Velocity

The determination of both the convective heat transfer coefficient and drag depends on the relative velocity between the receiver surfaces and the air. For fins, the relative velocity has only one component, which is in the radial direction. The radial velocity is

$$V_r = \frac{\dot{m}}{\rho A} \tag{8.9}$$

where air density is calculated by assuming that air is an ideal gas. The flow area available for air flow in a given zone accounts for the fraction of area blocked by solid surfaces.

Designs with rotating fibers involve two components of relative velocity: the radial component V_r given in Equation (8.9) and a tangential component V_θ caused by the rotation of the fiber through the air. As air moves into the receiver, the drag of the air on the moving fibers will tend to accelerate the air in the tangential direction, reducing the relative velocity. This effect is accounted for by including a drag factor (DF) that is the ratio of the actual relative velocity to the tangential velocity of the fibers. The drag factor was calculated as part of the air flow analysis described in Section 6. The relative tangential velocity for zone i is

$$V_\theta = (\dot{\omega})(2\pi r_i)(DF)/60 \tag{8.10}$$

The combined relative velocity is given by

$$V_{rel}^2 = V_r^2 + V_\theta^2 \tag{8.11}$$

8.5.2 Convective Heat Transfer From Fins

Convection from absorbing zones with fin-shaped pins and wedge-shaped pins in reflecting zones is assumed to have components of forced and natural convection. The natural convection Nusselt number is given by (Seibers, Schwind, and Moffat 1983):

$$Nu_{L_{fr}} = 0.098(Gr_L)^{1/3} \left[\frac{T_{zone(j)}}{T_{air_B(j)}}\right]^{-0.14} \tag{8.12}$$

where the significant length is the vertical length of the fin or wedge-shaped pin. This is normally the height of the zone. The forced convection component is given by (Seibers, Schwind, and Moffat 1983):

$$Nu_{Z_f} = 0.654\ (Re_Z)^{0.5} \tag{8.13}$$

where the significant length Z is the horizontal length of the fin or reflecting zone. This is normally the thickness of the zone. Air properties are calculated at the film temperature. The combined convective heat transfer coefficient is given by

$$h_{mix} = \left[(h_{fc})^{3.2} + (h_{nc})^{3.2}\right]^{1/3.2} \tag{8.14}$$

The terminal absorber is a special fin-shaped surface that includes the orificed inlet manifold. Because of the difficulty in predicting the convection from the terminal absorber, particularly for designs that include a substantial tangential air velocity, it was decided to arbitrarily fix the heat transfer coefficient from a terminal absorber at 30 W/m^2-K. Since little energy ultimately reaches the absorber, such an arbitrary choice should not significantly affect the results.

8.5.3 Convective Heat Transfer From Fibers

Convection from fibers for either fixed or rotating fiber designs is dominated by forced convection. The Nusselt number based on fiber diameter for forced convection is shown in Equation (8.15) (Morgan 1975).

For Re < 35

$$Nu_{F,D} = 0.583\ (Re_D)^{0.471} \qquad (8.15a)$$

For Re > 35

$$Nu_{F,D} = 0.795\ (Re_D)^{0.384} \qquad (8.15b)$$

where air properties are calculated at the film temperature. Inclusion of a shroud involves a separate convection model, which is presented in Section 8.4.

8.5.4 Drag

For designs with rotating absorbing zones, energy is required to actually rotate the zones. Parasitic power requirements are calculated by estimating the power required to overcome drag on the rotating surfaces and then dividing by an efficiency that accounts for motor and gear losses and rolling friction.

The drag force on a given zone is equal to the number of fibers in the zone times the drag per fiber. The number of fibers can be calculated from the average zone radius, the fraction of the zone surface area blocked by fibers, and the fiber diameter. The drag on an individual fiber is given by Equation (8.16) where the fiber is modeled as a cylinder in cross flow. The Reynolds number in Equation (8.16) is based on cylinder diameter, and the area is the projected area of the fiber (Welty, Wicks, and Wilson 1976).

$$F = \frac{A_p\ C_D\ \rho\ V_\infty^{\ 2}}{2} \qquad (8.16)$$

The drag coefficient is calculated from Equation (8.17) (Bejan and Poulikokos 1972).

For Re <4.0

$$C_D = 10.0\ \ Re^{-0.6} \qquad (8.17a)$$

For Re > 4.0

$$C_D = 5.484\ Re^{-0.246} \qquad (8.17b)$$

The power to overcome drag in zone i is given by Equation (8.18).

$$P_i = \frac{\text{Number of fibers}_i \quad A_{p_i} C_{D_i} \rho_i V_i^3}{2} \tag{8.18}$$

The total parasitic power used to rotate all rotating zones is given by Equation (8.19.)

$$P_T = \sum_{I=1}^{n} P_i \tag{8.19}$$

8.6 SHROUD MODEL

The inclusion of a shroud involves a separate model for determining the exchange factors between the shroud, the surroundings, and all other receiver surfaces. In addition, a separate convective heat transfer model is required in order to predict the convection between the shroud and the incoming air. Otherwise, the shroud is treated as any other receiver zone.

The Monte Carlo computer codes do not model the impact of the shroud on either insolation distribution or internal exchange factors. The prediction of exchange factors involving the shroud or the surroundings required the combination of a method for predicting radiation view factors between cylinders of finite length and the results of the Monte Carlo simulations.

A volumetric receiver with a shroud is modeled as an absorbing cylindrical core surrounded by a cylindrical shroud. Figure 8.2 shows the assumed arrangement of the receiver and the numbering scheme for the various surfaces. The view factors between the various surfaces shown in Figure 8.2 can be calculated using the equations for view factors between nested cylinders of finite length (Siegel and Howell 1972) and view factor algebra. The view factors between the surfaces in Figure 8.2 will equal the exchange factor if all surfaces are assumed to be black. This is a good assumption for surroundings but is not relevant for the core because we know the exchange factors for the core from the Monte Carlo model. To determine the impact of the shroud emissivity on receiver performance, a transient simulation of the receiver shown in Figure 8.2 was developed using a diffuse-gray model for shroud surfaces.

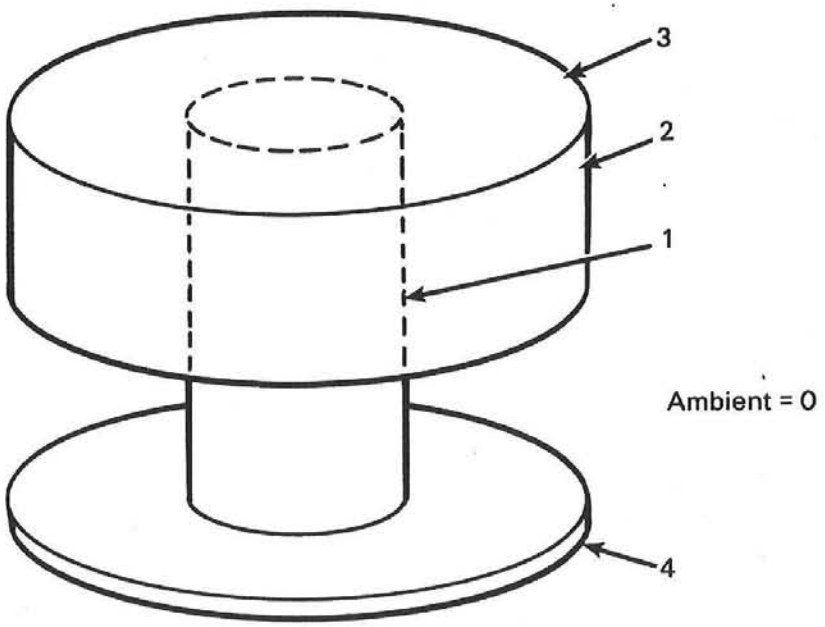

FIGURE 8.2. Schematic of Shroud Layout

The core was modeled as a black body at a temperature that radiated energy at a rate equal to reflection and reradiation from a typical core. The results, shown in Table 8.2, indicate that the emissivity of the shroud surfaces has little impact on either shroud temperature or reradiation losses.

The shroud can also have the size of the aperture reduced by blocking a fraction of the circumference as shown in Figure 8.3. This type of reduction of aperture area may be required to allow structural support of the receiver or to reduce thermal losses. The exchange factors are modified to account for the reduced aperture area. The details of the calculation of various exchange factors are presented by Drost (1984).

The general approach used in the performance model is independent of the receiver type. All surfaces are assumed to be initially at ambient temperatures. Insolation is added to the receiver, and the temperature of the receiver surface increases until the equilibrium temperature is reached. The shroud can absorb insolation directly from the heliostat field or as reflected energy from the absorbing core. Reflected energy from the core is calculated by the Monte Carlo model. The reflected energy is assumed to be diffuse so that the fraction of reflected energy reaching the shroud is determined by the

TABLE 8.2. Impact of Shroud Emissivity on Receiver Performance

Shroud Emissivity	Surface Temperature, K Surface: 2	3	4	Reradiation Losses, MW
0.2	990.5	951.9	891.2	10.17
0.4	991.8	956.4	901.4	10.17
0.6	992.2	957.7	904.3	10.16
0.8	992.2	958.0	905.4	10.15
1.0	992.4	958.6	906.3	10.14

(a) Receiver height 7 m
Core radius 5 m
Shroud radius 8.5 m
Aperture height 3.5 m

exchange factor from the core to the shroud. The remaining fraction of reflected energy exits the receiver to the surroundings and is considered a reflection loss. Otherwise, the shroud behaves exactly as any other zone in the receiver.

Convection from the shroud surfaces to the incoming air can be an important factor in reducing thermal losses. The nature of convection differs from the other surfaces, and a separate convection model was required. Two cases were considered: the first case included convection from the bare walls of the shroud. The second case consisted of filling the shroud with fiber packing to add heat transfer area as shown in Figure 8.4. In both cases the conservative assumption of including only natural convection from these surfaces was made.

Natural convection from the shroud design can be from the shroud floor, roof, and side. Equation (8.20) gives the Nusselt number for natural convection from the shroud wall. In this case the significant length is the height of the shroud (Welty, Wicks, and Wilson 1976).

$$\text{For } Ra < 1.0 \times 10^9$$

$$Nu_{x_{fr}} = 0.555\ Ra^{0.25} \qquad (8.20a)$$

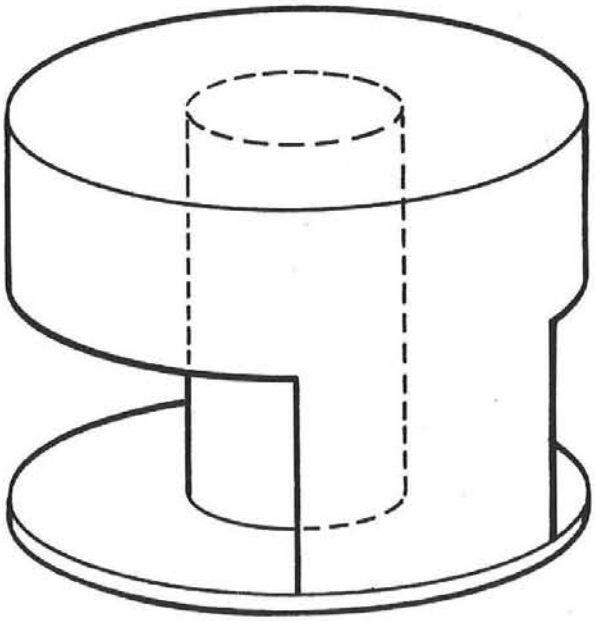

FIGURE 8.3. Schematic of Shroud with Aperture Blocking

For $Ra > 1.0 \times 10^9$

$$Nu_{x_{fr}} = 0.210\ Ra^{0.4} \qquad (8.20b)$$

where Ra is the Raleigh number.

Natural convection from the receiver floor is given by Equation (8.21), and natural convection from the receiver roof is given by Equation (8.22). In both cases the significant length is the area of the annular region between the shroud and the core divided by the perimeter of the annular region (Welty, Wicks, and Wilson 1976).

For $Ra < 2.0 \times 10^7$

$$Nu_{x_{fr}} = 0.54\ Ra^{0.25} \qquad (8.21a)$$

For $Ra > 2.0 \times 10^7$

$$Nu_{x_{fr}} = 0.14\ Ra^{0.333} \qquad (8.21b)$$

$$Nu_{x_{fr}} = 0.27\ Ra^{0.25} \qquad (8.22)$$

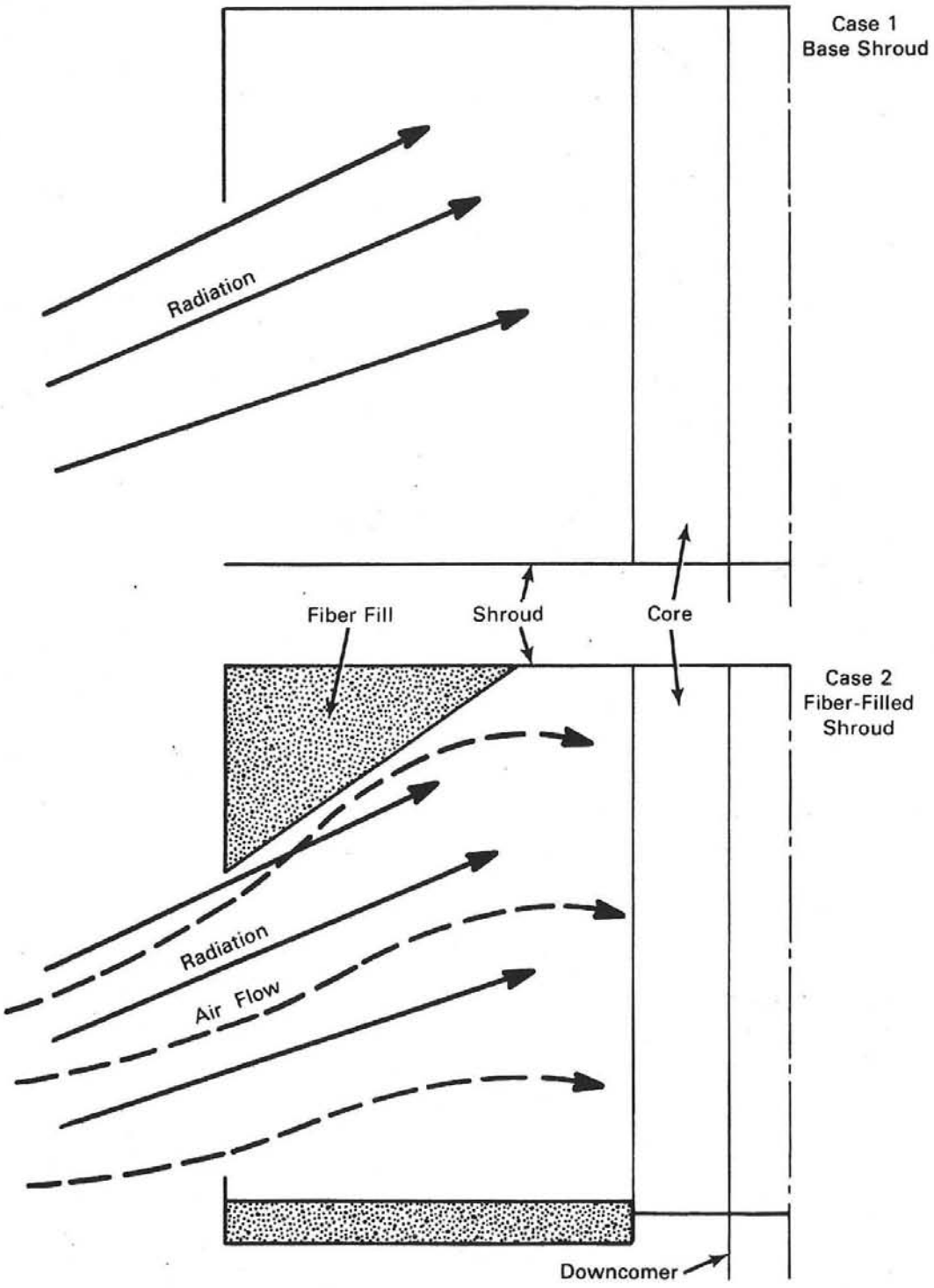

FIGURE 8.4. Shroud With Fiber Fill

Natural convection from a single strand in the fiber fill is given by Equation (8.23), where the significant length is the fiber diameter (Morgan 1978).

For Ra <100

$$Nu_{x_{fr}} = 1.02\ Ra^{0.148} \tag{8.23a}$$

For 100 < Ra < 10,000

$$Nu_{x_{fr}} = 0.85\ Ra^{0.188} \tag{8.23b}$$

For Ra > 10,000

$$Nu_{x_{fr}} = 0.480\ Ra^{0.250} \tag{8.23c}$$

Because of the nature of the performance model, the entire shroud is assumed to be isothermal. As Table 8.2 shows, there can be significant temperature variation between surfaces when convection is neglected. The inclusion of convection from shroud surfaces may further increase the temperature variations, but the analysis of this effect was beyond the scope of the study.

8.7 RESULTS OF THE PERFORMANCE MODEL

This section discusses the type of results produced by the performance model. The primary result of the performance model is the receiver equilibrium temperature distribution, including the zone material temperature, zone air exit temperature, and zone bulk air temperature. Once the receiver equilibrium temperature distribution is known, the performance model determines the reradiation losses and the flux ratio for each zone. The flux ratio is the ratio of maximum allowable flux (flux which would cause the zone material to exceed its maximum temperature limits) to the calculated flux based on average flux distribution. This number indicates how much flux maldistribution can be tolerated without exceeding material temperature limits. The thermal performance computer code also reports a variety of secondary results such as zone convective heat transfer coefficient, exchange factors, and net zone radiation heat transfer.

The computer code calculates several performance quantities, including receiver absorptivity, thermal efficiency, and total efficiency. Receiver absorptivity equals the ratio of the amount of energy absorbed in the receiver to the amount entering the receiver, and is calculated from the reflection loss evaluated using the Monte Carlo radiation model. The performance model does not independently calculate reflection loss but, where necessary, modifies it to include the impact of a shroud. The receiver thermal efficiency equals the ratio of the amount of energy transfered to the air in the receiver to the amount absorbed in the receiver. It includes a convective loss estimate that is calculated external to the performance model and included as an input variable. The performance model does not consider optical effects related to spillage losses. The receiver total efficiency equals the product of receiver absorptivity and thermal efficiency.

The results also include a gross receiver energy balance which totals convection, reflection, and reradiation losses; useful energy (energy added to the product air); and unaccounted energy (energy not accounted for because of an equilibrium temperature distribution not exactly converging to steady-state). The results also include the reradiation loss from each zone. This data proved useful in selecting designs that minimize reradiation losses.

8.8 VERIFICATION

The thermal performance code could not be completely verified because experimental results were not available. Instead, two approaches were used to give some indication that the performance model was working as intended. First, all significant algorithms such as heat transfer coefficient and view factor calculations were compared to hand calculations. Second, the equilibrium temperature distribution was checked to insure that the net receiver energy balance, net zone energy, and net internal radiation heat transfer all equaled 0.0, as the First Law of Thermodynamics would require. The computer code that embodies the performance model also calculates the unaccounted energy, which gives an indication of how close the computer solution is to the steady-state solution. The convergence criteria for zone temperature can be adjusted to obtain the desired level of agreement between the calculated equilibrium temperature distribution and the true steady-state solution.

of an average annual output was beyond the scope of this study. The end use for the product was not specified. The receiver was to deliver air at the design temperature to the ground level.

The designs considered in this study were all assumed to use a surround field. This eliminated traditional downward-facing cavities and cavity receivers with a north field. (As will be discussed later, a modified downward-facing aperture may be preferred so as to minimize the amount of insolation absorbed on the receiver top.) Both designs have advantages, but since the existing radiation heat transfer and performance models did not allow an accurate evaluation of these concepts, they were not evaluated. We found no reason to believe that these concepts would be more appropriate than the shroud concept.

Several major assumptions in the radiation heat transfer model were discussed earlier. Assumptions specific to particular designs are presented here.

The modeling of fin-shaped rows for radiation was straightforward, but the fiber designs included several simplifying assumptions. All the fibers in a zone were assumed to be in one row, where actually a zone would contain many rows with the fibers being more sparsely spaced. Secondly, the fibers were modeled as small squares with a surface area equal to the surface area of the cylindrical fiber. This assumption was required because the radiation model in its current form could not simulate curved surfaces. Because of its small size, the fiber may consist of three or four strands wrapped together. In any case, the impact is hoped to be small because the radiation tends to be quite diffuse, in which case the square and cylindrical models could have similar performance.

9.2 ABSORBING ARRAY SELECTION

Section 3.1 discussed the three absorbing array configurations considered in this study. This section describes the evaluation of the staggered fin, radial fin, and fiber array designs. For the purpose of this evaluation, a base case design was developed for each absorbing array; each array was housed in a cavity-type shroud for consistency in the evaluation. Performance calculations were made and are reported below.

9.0 VOLUMETRIC RECEIVER DESIGN STUDIES

Section 3 presented an overview of the evolution of the volumetric receiver design, while Sections 4 through 8 discussed thermal processes and described models developed to simulate these processes. This section reports the results of the studies that led to the decisions during the design evolution. Detailed here are the results of the absorbing array study, which ultimately led to choosing ceramic fibers as the preferred array elements. Also included are results of the convective heat transfer enhancement study, which led to the choice of the preswirl method for augmenting convection. Presented here are details of the geometric loss reducer study, which demonstrates the problems with the reflecting row light-valve technique and depicts the need for a shroud/cavity type of housing to reduce thermal losses. The final volumetric air heating receiver design emerged from these three studies and is described in Section 9.5. Finally Section 9.6 describes the uncertainties associated with this final preconceptual design. Before presenting the results, we first describe the ground rules and assumptions used in these studies.

9.1 GROUND RULES AND ASSUMPTIONS

To compare the various designs on a consistent basis, a number of ground rules and assumptions were used throughout the study. Also, certain technical constraints were imposed on the designs to limit the scope of the study.

All designs were evaluated using a common set of ground rules. These include:

Plant output - 50 MWt
Product - high-temperature air
Product temperature - 1367 K
Product pressure - 1 atm
Inlet air temperature - 297 K
Inlet air pressure - 1 atm

Receiver performance was calculated at a specific point in time. In actual operation, daily and annual variations in the heliostat field output will cause variations in the receiver performance and output. The calculation

9.2.1 Staggered Fin Array

The staggered fin concept consists of a volumetric receiver with an absorbing media of a large number of short fins arranged in annular zones. The fins in one zone are offset from the fins in an adjacent zone. This design has the advantage of allowing more dense packing toward the interior of the receiver, and was originally thought to have superior pin-to-air heat transfer.

Preliminary calculations indicated that a staggered fin receiver would be large. In this study the receiver height was assumed to be 15 m, with the absorbing array of 0.75-m-long fins extending 10 m out from the centerline of the receiver. The selection of the fin spacing was based on a series of insolation distribution calculations using the VORRUM computer code. The goal was to have a large fraction of the insolation absorbed on the interior zones where the heat transfer area was large and the exchange factor for radiation to the surroundings was small. This type of distribution was obtained by having the fins in the exterior rows widely spread with the packing becoming more dense in the interior zones. The absorbing array was not extensively studied, and performance can probably be improved somewhat. But the poor overall performance of this concept indicated that a detailed evaluation was not appropriate.

It was assumed that the base case design would include a shroud with an aperture height of 6.0 m and without any shroud fiber packing for enhancing convection from the shroud. The characteristics of the base case design are presented in Table 9.1.

The results for the base case design are presented in Table 9.2. The staggered fin design is predicted to have a total receiver efficiency of 39.3% and a minimum flux ratio (as defined in Section 8.7) of 1.2. Although the flux ratio of 1.2 implies that an average material temperature limit would not be exceeded, the allowable peak flux is only 20% greater than the average flux, which is an unacceptable safety factor. Based on the low efficiency and unacceptable flux ratio, the staggered fin design was rejected.

The major problem with the staggered fin design is the low convective heat transfer coefficient between the fins and the air. It is possible that methods

TABLE 9.1. Staggered Fin Base Case Design

Overall Characteristics

Receiver Height = 15.0 m
Receiver Radius = 19.0 m
Air Flow Rate = 42.8 kg/s
Product Design Temperature = 1367 K

Aperture Height = 6.0 m
Blocking Factor = 0.05
Shroud Fill = None

Zone Characteristics

Zone No.	Type	Height, m	Depth, m	Fin Spacing, m	Convection Area, m^2	Radiation Area, m^2	Emissivity
1	Shroud	15.0	9.0	NA	2714.0	2714	1.00
2	0.001-m-thick Fin	15.0	0.75	5.18	270.0	270	0.80
3	"	15.0	0.75	4.79	270.0	270	0.80
4	"	15.0	0.75	4.40	270.0	270	0.80
5	"	15.0	0.75	4.01	270.0	270	0.80
6	"	15.0	0.75	1.81	540.0	540	0.80
7	"	15.0	0.75	1.62	540.0	540	0.80
8	"	15.0	0.75	0.71	1080.0	1080	0.80
9	"	15.0	0.75	0.31	2160.0	2160	0.80
10	"	15.0	0.75	0.13	4320.0	4320	0.80
11	"	15.0	0.75	0.05	8640.0	8640	0.80
12	Terminal Absorber	15.0	NA	NA	8759.0	3739	0.80

TABLE 9.2. Staggered Fin Base Case Design Performance

Zone	Zone Convective Heat Transfer Coefficient, W/m^2-K	Zone Material Temperature, K	Zone Air Exit Temperature, K	Zone Flux Ratio	Zone Insolation, %
1	9.19	1160	669	1.8	5.7
2	6.42	1231	690	1.6	3.7
3	6.48	1298	713	1.4	7.8
4	6.24	1294	734	1.4	6.2
5	6.07	1302	753	1.4	5.7
6	5.90	1325	791	1.4	7.2
7	5.71	1360	827	1.3	8.5
8	5.41	1387	891	1.3	9.9
9	4.94	1432	998	1.3	14.2
10	4.24	1469	1145	1.2	14.4
11	3.43	1489	1297	1.3	10.3
12	5.00	1508	1362	1.4	4.8

Energy Balance	
Reflection Losses, W	2,137,770
Convection Losses, W	0
Reradiation Losses, W	75,566,536
Useful Power, W	50,317,066
Unaccounted Power, W	207,801
Total, W	128,229,254

Receiver Efficiency

Receiver Absorptivity = 0.982
Receiver Thermal Efficiency = 0.400
Receiver Total Efficiency = 0.393

of enhancing heat transfer could be developed. One of our sensitivity studies investigated the impact of a fivefold increase in the convective heat transfer coefficient, and the results show that the total efficiency is still unacceptably low (55.1%) but that the minimum flux ratio has significantly improved to 2.1. It appears that even with a major increase in the convective heat transfer coefficient, the staggered fin design is not competitive with other air heating receiver concepts.

Several other sensitivity studies were conducted, and the results are summarized in Table 9.3. The impact of different product temperatures was investigated. Product temperatures of 1089 K (1500°F) and 811 K (1000°F) were considered, and the results show that the receiver efficiency and flux ratios

TABLE 9.3. Staggered Fin Array Sensitivity Study Results

Base Case	Thermal Efficiency	Total[(a)] Efficiency	Minimum Flux Ratio
Unpacked Shroud T = 1367 K	0.400	0.393	1.2
Unpacked Shroud T = 1089 K	0.564	0.555	1.7
Unpacked Shroud T = 811 K	0.722	0.710	2.1
Packed Shroud T = 1367 K	0.473	0.466	1.5
Uncovered T = 1367 K	0.305	0.284	1.3
Unpacked Shroud T = 1367 K Augmented Convection	0.560	0.551	2.1

(a) Does not include convection or spillage losses.

are improved but that the concept is still not competitive with other air heating receivers at these operating temperatures. The inclusion of fiber packing in the shroud improved receiver efficiency by 15%, while the deletion of a shroud decreased thermal performance by 30%.

9.2.2 Radial Fin Array

The radial fin concept consists of large fins arranged radially to form the absorbing array of the volumetric receiver. It was clear from preliminary calculations that a radial fin receiver would be large. In this study the receiver height was assumed to be 15 m with the fins extending 10 m from the centerline of the receiver. The selection of the fin spacing was based on a series of insolation distribution calculations using the VORRUM computer code. The results are presented in Table 9.4 where each zone in the first column represents a 0.75-m-long segment of one radial fin. Based on these calculations, the design with an angle of 5 degrees between fins was selected. These results are based on Monte Carlo simulations with a relatively small number of

TABLE 9.4. Insolation Distribution for the Radial Fin Array

Zone	Energy absorbed in zone, %					
	12 fins (30° spacing)	24 fins (15° spacing)	36 fins (10° spacing)	72 fins (5° spacing)	120 fins (3° spacing)	360 fins (1° spacing)
1 (10 m-9.25 m)	4.2	5.6	6.8	9.4	13.1	35.1
2 (9.25 m-8.5 m)	9.1	6.6	6.9	10.4	15.6	24.4
3 (8.5 m-7.75 m)	5.5	6.6	7.8	11.0	15.6	14.3
4 (7.75 m-7.00 m)	6.8	7.8	7.7	11.8	11.4	7.2
5 (7.00 m-6.25 m)	7.4	7.0	7.2	11.0	9.5	4.2
6 (6.25 m-5.50 m)	6.2	7.9	9.1	8.1	8.0	3.4
7 (5.50 m-4.75 m)	7.4	7.8	7.6	7.4	5.9	2.4
8 (4.75 m-4.00 m)	6.8	7.0	8.0	6.5	5.0	1.8
9 (4.00 m-3.25 m)	6.6	8.3	7.7	5.4	3.6	1.5
10 (3.25 m-2.5 m)	7.1	7.1	6.8	5.0	3.2	0.9
11	25.5	22.2	19.7	10.5	6.3	2.5
Reflection Loss, %	7.4	6.1	4.8	3.4	2.9	2.2

photon bundles, so the standard deviation is relatively high (approximately 25% of the mean value). However, the actual results are not as important as the trends, which show that as more fins are added, the insolation is absorbed on the exterior portions of the fins and that reflection losses decrease. Convection considerations suggest a large number of fins, but the 1° and 3° designs have an unacceptable fraction of the energy absorbed in the exterior four zones.

Table 9.5 presents the characteristics of the base case design. We assumed that the base case design would include a shroud with an aperture height of 6 m and without shroud fiber packing. The results for this base case design are presented in Table 9.6. The radial fin design has a total receiver efficiency of 45% and a minimum flux ratio of 0.9 for the interior zone. A flux ratio less than 1.0 indicates that the material temperature limit has been exceeded; therefore this design is unacceptable. The design could be modified to increase the flux ratio by increasing either the receiver radius or diameter. This would increase the size and weight of the design, which is already too large and heavy. Based on the low efficiency and unacceptable flux ratio, the radial fin design was rejected.

As with the staggered fin array, the major problem with the radial fin design was the low convective heat transfer coefficient between the fins and the air. It is possible that methods of enhancing heat transfer could be developed. One of our sensitivity studies investigated the impact of a fivefold increase in the convective heat transfer coefficient. The results show that the total efficiency is still unacceptably low (67%), but that the minimum flux ratio is a reasonable 3.4. It appears that even with a major increase in the convective heat transfer coefficient the radial fin design is not competitive with other air heating receiver concepts.

Several other sensitivity studies were conducted and the results are summarized in Table 9.7. The impact of varying the product temperature was investigated and shows that reducing the product temperature will improve the

TABLE 9.5. Radial Fin Base Case Design

Overall Characteristics

Receiver Height = 15.0 m
Receiver Radius = 19.0 m
Air Flow Rate = 42.8 kg/s
Product Design Temperature = 1367 K

Aperture Height = 6.0 m
Blocking Factor = 0.05
Shroud Fill = None

Zone Characteristics

Zone No.	Type	Height, m	Depth, m	Fin Spacing, m	Convection Area, m^2	Radiation Area, m^2	Emissivity
1	Shroud	15.0	9.0	NA	2714	2714	1.00
2	0.001-m-Thick Fin	15.0	0.75	0.8627	1638	1638	0.8
3	"	15.0	0.75	0.7978	1638	1638	0.8
4	"	15.0	0.75	0.7331	1638	1638	0.8
5	"	15.0	0.75	0.6684	1638	1638	0.8
6	"	15.0	0.75	0.6038	1638	1638	0.8
7	"	15.0	0.75	0.5391	1638	1638	0.8
8	"	15.0	0.75	0.4744	1638	1638	0.8
9	"	15.0	0.75	0.4097	1638	1638	0.8
10	"	15.0	0.75	0.3450	1638	1638	0.8
11	"	15.0	0.75	0.2803	1638	1638	0.8
12	Terminal Absorber	15.0	NA	NA	3759	236	0.8

TABLE 9.6. Radial Fin Base Case Performance

Zone	Zone Convective Heat Transfer Coefficient, W/m^2-K	Zone Material Temperature, K	Zone Air Exit Temperature, K	Zone Flux Ratio	Zone Insolation, %
1	9.08	1080	632	2.1	2.90
2	6.08	1167	737	1.8	8.48
3	5.50	1248	826	1.6	10.29
4	5.08	1316	905	1.5	10.81
5	4.74	1369	974	1.4	10.50
6	4.45	1410	1034	1.4	9.88
7	4.22	1445	1088	1.3	8.71
8	4.01	1474	1136	1.3	8.33
9	3.85	1502	1179	1.2	6.05
10	3.73	1534	1219	1.1	6.46
11	3.62	1563	1257	1.0	5.53
12	5.00	1598	1362	0.9	11.20

Energy Balance	
Reflection Losses, W	941,197
Convection Losses, W	0
Reradiation Losses, W	59,246,245
Useful Power, W	50,347,454
Unaccounted Power, W	253,921
Total, W	110,788,818

Receiver Efficiency
Receiver Absorptivity = 0.991
Receiver Thermal Efficiency = 0.459
Receiver Total Efficiency = 0.455

receiver efficiency and flux ratio. The inclusion of fiber packing in the shroud improves thermal efficiency by 15%, while deleting the shroud decreases the thermal efficiency by 20%.

9.2.3 Fiber Array

The fiber array concept consists of a volumetric receiver where the absorbing medium is made up of a large number of ceramic fibers. Based on estimates of receiver heat transfer area and convective heat transfer coefficients, it was clear that a fiber design would be large. For the base case design the absorbing core was 20 m high and had a radius of 7.9 m. With a shroud having a 6-m aperture height but no fiber packing, the total receiver

TABLE 9.7. Radial Fin Sensitivity Study Results

Base Case	Thermal Efficiency	Total[(a)] Efficiency	Minimum Flux Ratio
Unpacked Shroud T = 1367 K	45.9	45.5	0.9
Unpacked Shroud T = 1089 K	65.6	65.1	1.8
Unpacked Shroud T = 811 K	83.4	82.6	2.6
Packed Shroud T = 1367 K	52.1	51.7	1.1
Uncovered T = 1367 K	36.5	35.2	0.9
Unpacked Shroud T = 1367 K Augmented Convection	67.8	67.2	3.4

(a) Does not include convection or spillage losses.

diameter was 21.9 m. The design of the fiber absorbing core is discussed in more detail in Section 9.3. Characteristics of the base case design are presented in Table 9.8.

The results for the base case design are presented in Table 9.9. The fiber array design has a total receiver efficiency of 56.7% and a minimum flux ratio of 1.8. Although the performance of the fiber receiver is better than the fin designs, the large size and low thermal efficiency made this design also unattractive.

Several other sensitivity studies were conducted and the results are summarized in Table 9.10. The impact of different product temperatures was investigated. Product temperatures of 1089 K (1500°F) and 811 K (1000°F) were considered, and the results show that the receiver efficiency and flux ratios are better with the 811 K design, showing good efficiency and a flux ratio of 3.1. The inclusion of shroud packing shows a relatively small improvement (5%) in receiver performance. With the unpacked design, the shroud surface is

TABLE 9.8. Base Case Fiber Design Characteristics

Overall Characteristics

Receiver Height = 20.0 m
Receiver Radius = 21.9 m
Air Flow Rate = 42.8 kg/s
Product Design Temperature = 1367 K
Aperture Height = 6.0 m
Blocking Factor = 0.05
Shroud Fill = None

Zone Characteristics

Zone No.	Type	Height, m	Depth, m	Fiber Spacing, m	Convection Area, m^2	Radiation Area, m^2	Emissivity
1	Shroud	20.0	14.0	NA	4152	4152	1.00
2	0.0006-m-dia fiber	20.0	0.6	0.012	124	124	0.90
3	" " " "	20.0	0.6	0.009	151	151	0.90
4	" " " "	20.0	0.6	0.0075	165	165	0.90
5	" " " "	20.0	0.6	0.0045	240	240	0.90
6	" " " "	20.0	0.6	0.0033	285	285	0.90
7	" " " "	20.0	0.6	0.0020	387	387	0.90
8	" " " "	20.0	0.6	0.0010	566	566	0.90
9	" " " "	20.0	0.6	0.0005	730	730	0.90
10	" " " "	20.0	0.6	0.0001	1016	1016	0.90
11	Terminal Absorber	20.0	NA	NA	3759	3759	0.80

TABLE 9.9. Fiber Array Design Performance Results

Zone	Zone Convective Heat Transfer Coefficient, W/m^2-K	Zone Material Temperature, K	Zone Air Exit Temperature, K	Zone Flux Ratio	Zone Insolation, %
1	11.44	953	728	2.8	4.7
2	53.16	1132	781	1.8	6.2
3	55.70	1109	835	2.1	5.1
4	59.23	1131	890	2.2	5.6
5	63.47	1160	963	2.3	8.2
6	68.44	1188	1038	2.4	8.9
7	74.65	1237	1126	2.4	13.2
8	82.08	1280	1219	2.7	16.9
9	91.13	1328	1299	3.0	16.5
10	102.02	1365	1356	3.8	12.9
11	5.00	1376	1362	13.3	0.9

Energy Balance	
Reflection Losses, W	761,415
Convection Losses, W	0
Reradiation Losses, W	37,650,082
Useful Power, W	50,322,276
Unaccounted Power, W	189,708
Total, W	88,923,483

Receiver Efficiency

Receiver Absorptivity = 0.991
Receiver Thermal Efficiency = 0.572
Receiver Total Efficiency = 0.567

already quite large and the addition of more surface area by packing does not significantly improve performance, but does improve the flux ratio because a smaller fraction of the energy convected to the air is handled by the interior fiber zones. The uncovered design with no shroud has a 20% reduction in receiver efficiency.

In the final analysis, the fiber design proved to be the best candidate for the absorbing array. Besides providing better heat transfer coefficients compared to the fin designs, the fiber concept eliminates concern with angular variations in insolation and reduces the weight and cost of the receiver.

TABLE 9.10. Results of Fiber Array Sensitivity Studies

Base Case	Thermal Efficiency	Total[(a)] Efficiency	Minimum Flux Ratio
Unpacked Shroud T = 1367 K	0.572	0.567	1.8
Unpacked Shroud T = 1089 K	0.802	0.795	2.5
Unpacked Shroud T = 811 K	0.934	0.926	3.1
Packed Shroud T = 1367 K	0.594	0.589	2.4
Uncovered T = 1367 K	0.446	0.422	1.7

(a) Does not include convection or spillage losses.

However, concern over the large size of even the fiber receiver design led us to consider techniques to enhance convection from the fibers. These are discussed below.

9.3 CONVECTIVE HEAT TRANSFER ENHANCEMENT

Section 3.2 described two techniques for augmenting the convective heat transfer from the fiber array. This section describes the evaluation of these techniques. Both methods center around increasing the relative velocity between the air and the fibers. One method moves the fibers through the air (rotating fiber array), while the other method moves the air quickly past the fibers (preswirl). For this evaluation, both designs included reflecting wedges around the receiver's perimeter. Performance calculations were made and are reported below.

9.3.1 Rotating Fiber Array

This technique consists of two regions of fiber zones, one rotating at some specified angular velocity, and the other region fixed. A concept sketch of this technique is shown in Figure 9.1. As the fibers rotate through the radially flowing air, the velocity of the air will be large relative to the

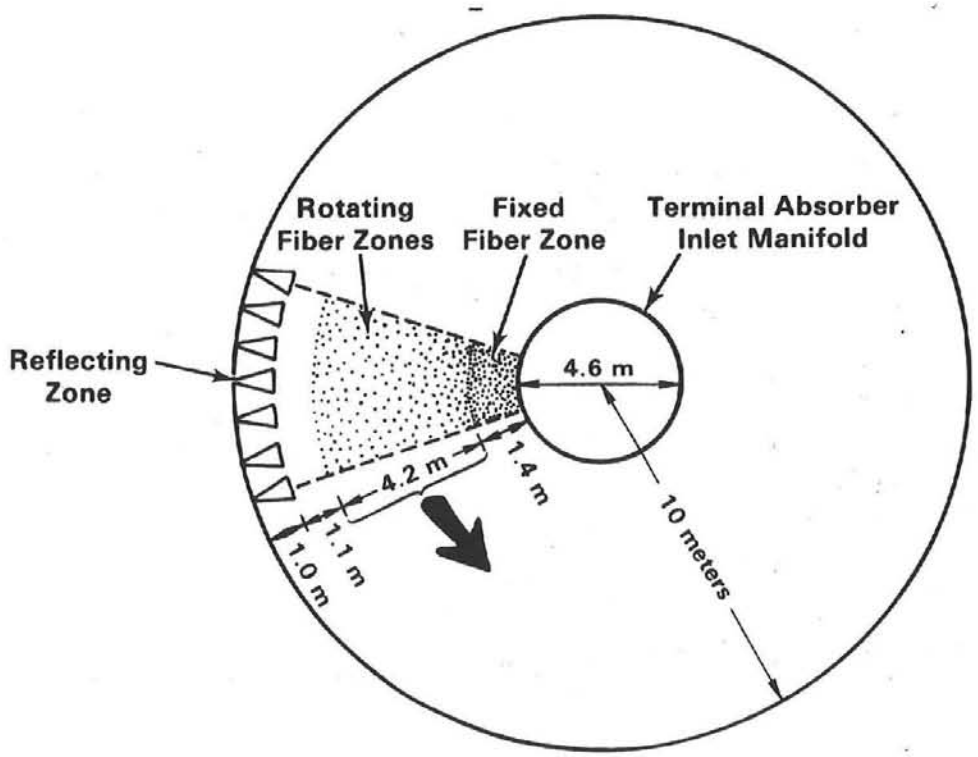

FIGURE 9.1. Plan View of the Rotating Fiber Volumetric Receiver

fibers. Figure 9.2 shows the results of the VORTEX analysis of this technique, where we see the radial distribution (from the outer fiber zone inward) of fiber, tangential and radial air, and fiber/air relative velocities.

The rotating fibers tend to drag air along with them, creating a tangential component of the air velocity toward the direction of fiber rotation. Since the airflow must conserve angular momentum, this tangential component increases as the air flows inward. The increase shown in Figure 9.2 suggests that the two inner fibers zones should remain stationary.

In principle, this technique is very effective in augmenting convective heat transfer. However, a rotating component in the receiver makes the design much more complex than the original concept. Details would have to be worked out regarding the mechanical design of this mechanism to operate in a high-temperature environment. Furthermore, methods to prevent fiber damage in case of emergency conditions would have to be incorporated into the design.

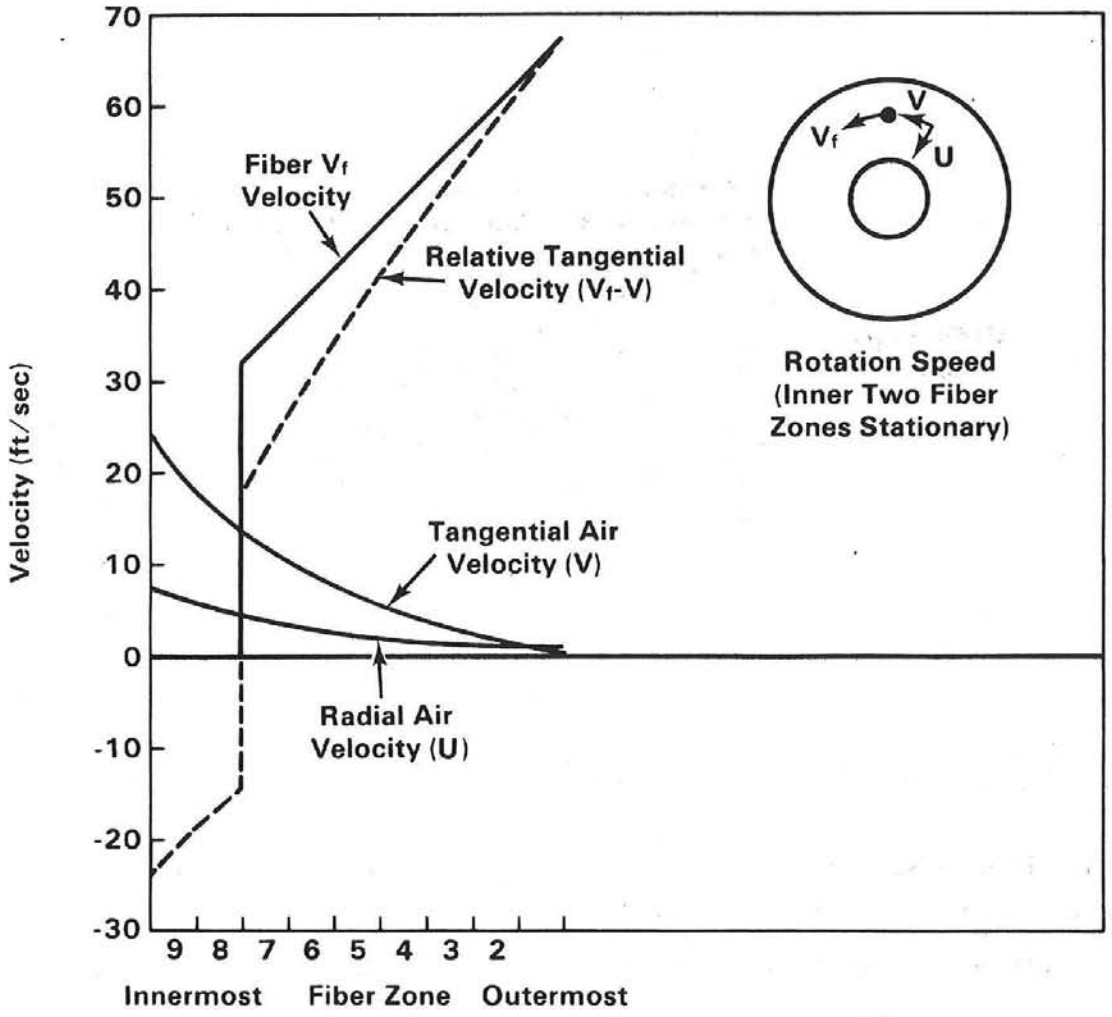

FIGURE 9.2 Velocity Profiles for Rotating Fiber Receiver

9.3.2 Preswirl

The preswirl technique, shown in Figure 9.3, consists of plane jets of air issuing tangentially from a series of slotted pipes located at the perimeter of the receiver. This tangentially directed airflow will impart enough angular velocity to the radially flowing air to induce a swirl before the air reaches the fibers. As the air flows radially inward, it must conserve angular momentum, so the angular velocities (and therefore relative velocities) will be largest in the critical inner region of the receiver (Figure 9.4). Energy requirements to produce the jets are, in principle, relatively low.

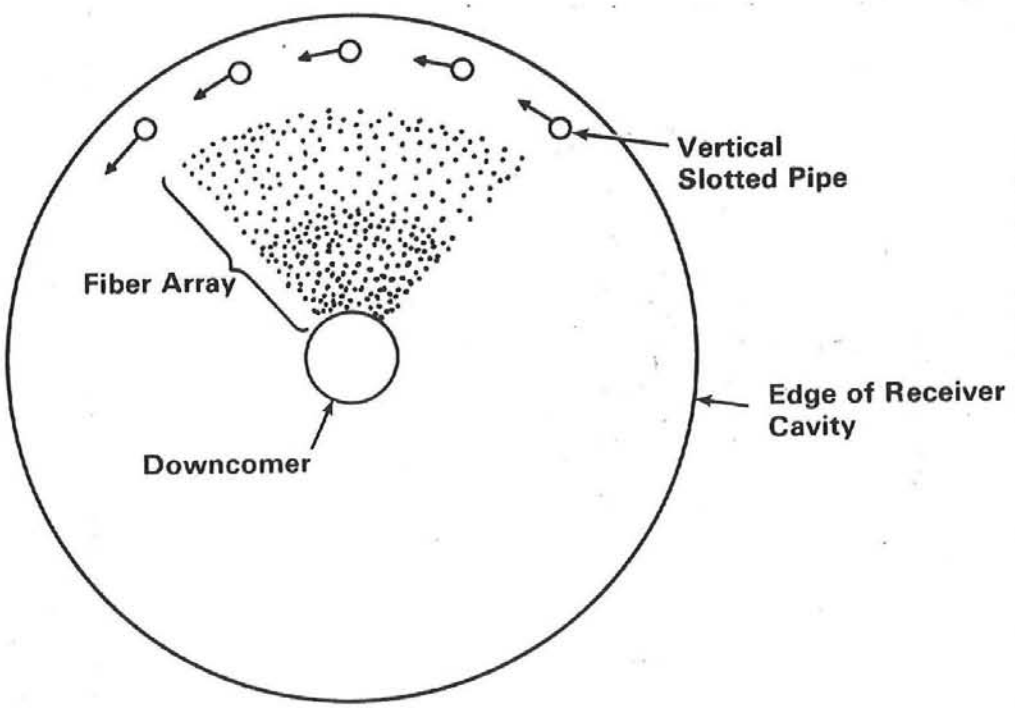

FIGURE 9.3. Plan View of Preswirl Volumetric Receiver

9.3.3 Comparison of the Thermal Performances

The rotating fiber array and preswirl techniques were evaluated in terms of thermal performance using the computer codes discussed in previous sections. Two nearly identical base case designs were developed. One design incorporated the rotating concept; the other included the preswirl. In both designs the maximum relative air velocity at the fibers was limited to 30 m/s. The results of this evaluation are presented in Table 9.11. The results indicated that the type of augmentation has little impact on receiver efficiency but does affect the minimum flux ratio. As shown in Figure 9.5, the velocity distribution for the preswirl design more nearly approximated the distribution of absorbed insolation. Therefore, areas with high energy absorption corresponded to areas of high convective heat transfer coefficients, which resulted in lower fiber temperatures.

Although both techniques offer similar performance, the technical risks associated with the rotating concept were perceived to be greater than with the preswirl. Many problems could be imagined associated with the mechanical

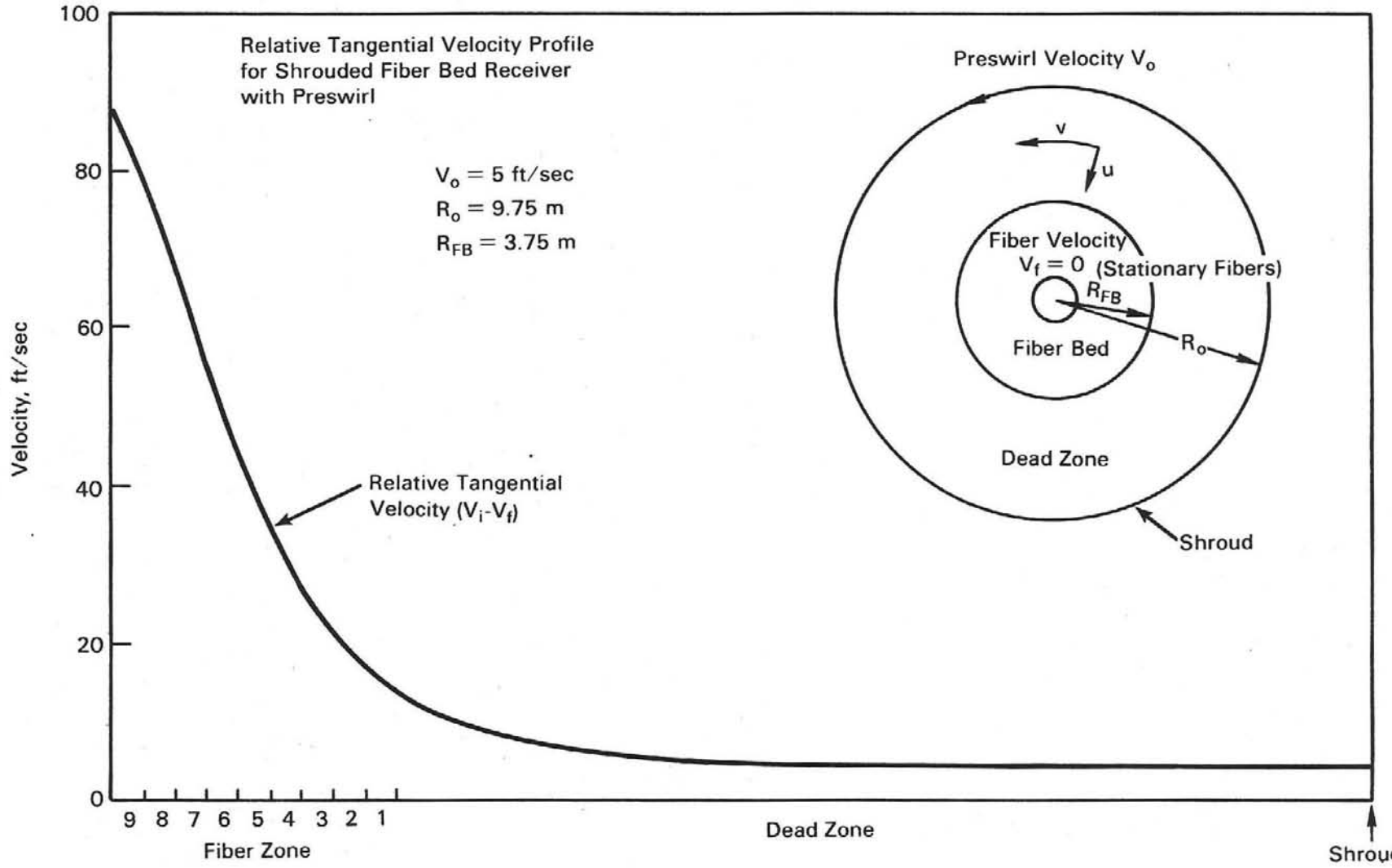

FIGURE 9.4. Velocity Profiles for Preswirl Receiver

TABLE 9.11. Impact of Augmentation Technique on Thermal Performance

Base Case	Thermal Efficiency	Total Efficiency[a]	Minimum Flux Ratio for Fiber Zones
Preswirl (30 m/s max.) T = 1367 K	0.885	0.868	3.9
Rotation (25 rpm) T = 1367 K	0.876	0.859	2.8

(a) Does not include convection or spillage losses.

design of the rotating mechanism and the operation of a receiver with a large component rotating. As a result, the preswirl technique was preferred. One main difficulty with the preswirl technique, however, is significant: nonuniformities of the angular velocities may be unavoidable because of peripheral velocity variations from the discrete number of jet sources. These nonuniformities may lead to hot spots within the receiver. In addition, the theory of slotted jets is not well developed, and theory on jets in series is nonexistent. Therefore, substantial development of this technique would be required before reliable performance predictions are possible.

9.4 GEOMETRIC LOSS REDUCER

Section 3.3 described two techniques for reducing reflection and reradiation losses in an attempt improve thermal performance. The first method consists of a row of specularly reflecting wedges arranged vertically around the perimeter of the receiver. A cavity-type shroud housing the absorbing array is the second method. Both methods are evaluated below.

9.4.1 Reflecting Row

Reflecting rows for geometric loss reduction originally appeared attractive, and the inclusion of reflecting rows was felt to be an important feature of any volumetric receiver design. Therefore, the reflecting zone concept was studied in detail.

The reflecting rows were a unique feature of this design and were the subject of a generic study used to identify the most attractive reflecting row

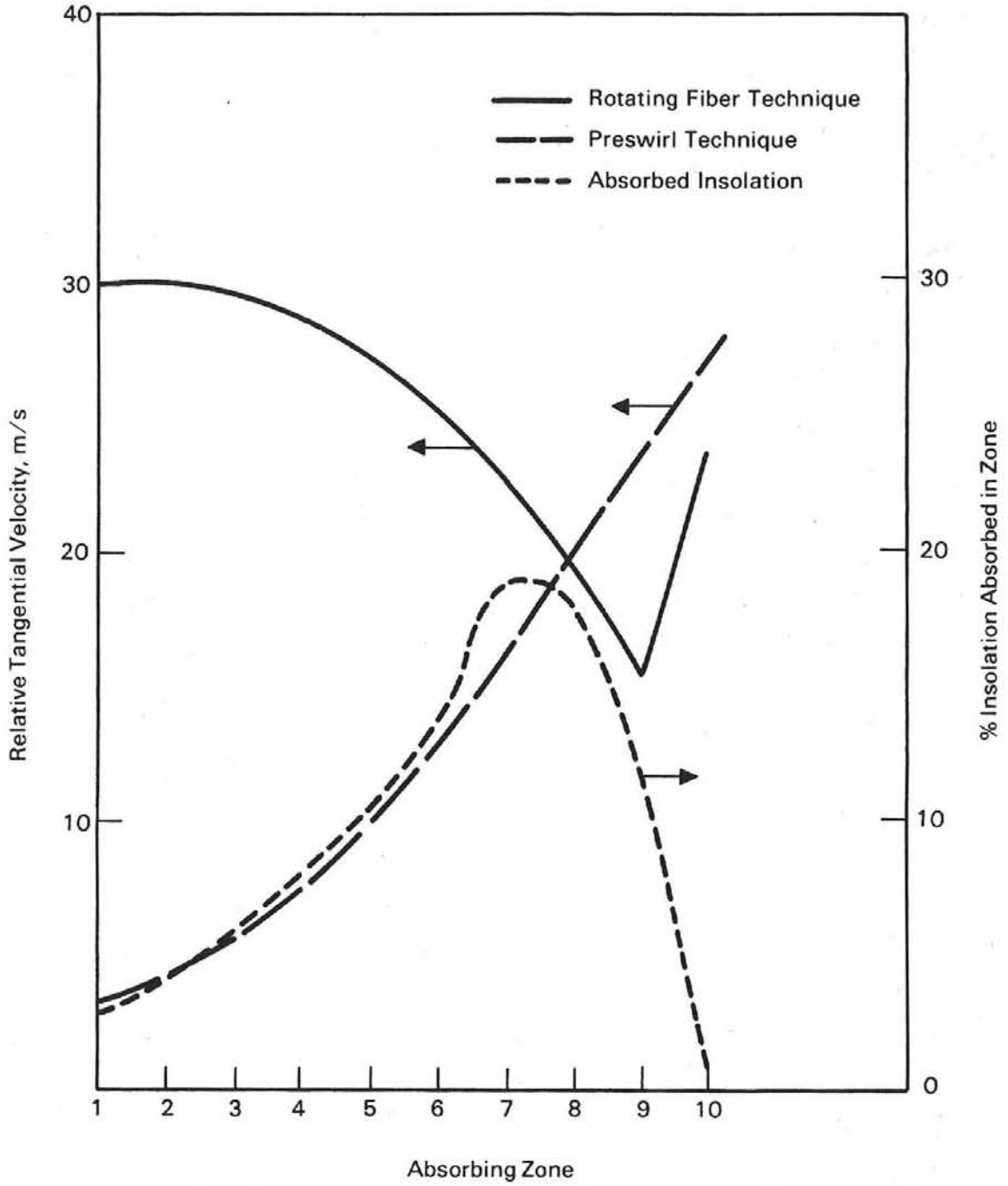

FIGURE 9.5 Distribution of Air Relative Velocity and Insolation Absorption

configuration. Since the study was generic, it was not associated with any specific receiver design. The inclusion of an absorbing core would have substantially increased the computer time required for one simulation, and would have limited the scope of the study. Therefore, the study used an idealized absorbing core.

The generic reflecting zone study was conducted using a modified version of the VORRUM computer code. This variant, the VORRRM (Volumetric Receiver Reflecting Row Model), simulated both the interaction of the reflecting row with insolation and with reradiated or reflected energy. First, the model simulated the interaction of insolation with the reflecting zone, determining the energy absorbed in the reflecting zone, the energy reflected back to the surroundings, and the energy passing through the core into the interior. Any radiation passing through the reflecting zones was assumed to be absorbed in the interior of the receiver. After determining the zone performance from the standpoint of insolation, the VORRRM code then simulated the emission of reradiated or reflected photon bundles from an idealized core. The history of the photon bundles was observed, and the results for a large number of photon bundles determined the fractions of reradiated or reflected photon bundles which were absorbed in the reflecting zone, reflected back to the absorbing core, or passed through the reflecting zone to the surroundings.

A large number of designs were simulated using the VORRRM computer code. The most attractive designs were based on a performance figure of merit (the minimum combined receiver losses). The combined receiver losses for the generic study included reflection and reradiation from the interior receiver surfaces and reflection from the reflection rows. The combined reflection and reradiation coming from the absorbing core was assumed to be 30% of the incident energy on the receiver. Based on this estimate, the receiver loss is given by

$$\text{Receiver loss} = \text{Reflection loss from reflecting zone} + \text{Reflecting zone Transmissivity for reradiation} \times 0.30$$

The most attractive reflecting zone design will have the lowest losses while not exceeding material temperature limitations. In general, low-loss designs also have large amounts of incident energy and reradiation absorbed in the reflecting zones, resulting in high material temperatures. For the generic study, it was assumed that the reflecting zones are fabricated from aluminum, which limits the zone temperature to 650 K. Any safety factor needed to account for maldistribution of insolation or air flow will further reduce the maximum allowable zone temperature.

The reflecting zone temperature was calculated by estimating the energy absorbed in the zone and then determining the zone temperature necessary to transfer the energy from the pin to the air. The pin-to-air convective heat transfer coefficient was assumed to be 5.0 W/m^2-K.

The reflecting zone analysis consisted of three stages. In the first stage, the design of a single reflecting zone was investigated for four receiver geometries. Characteristics of the four receiver geometries (case 1 through 4) are:

Case	Receiver Radius, m	Receiver Height, m	Heliostat Image Size, m
1	5	10	4.0
2	5	10	2.0
3	10	5	4.0
4	10	5	2.0

The significant parameters which characterize a zone were the cell aspect ratio, cell width, and wedge angle. These parameters are shown in Figure 9.6. Surface emissivity was assumed to be 0.2 for the aluminum reflecting rows. This assumption was optimistic, particularly considering that the operating temperature of the reflecting zone was normally around 600 K.

Following the first stage analysis, one of the single-reflecting-zone designs was selected as the first zone in a two-reflecting-zone design; subsequently another single-reflecting-zone design was selected as the first of

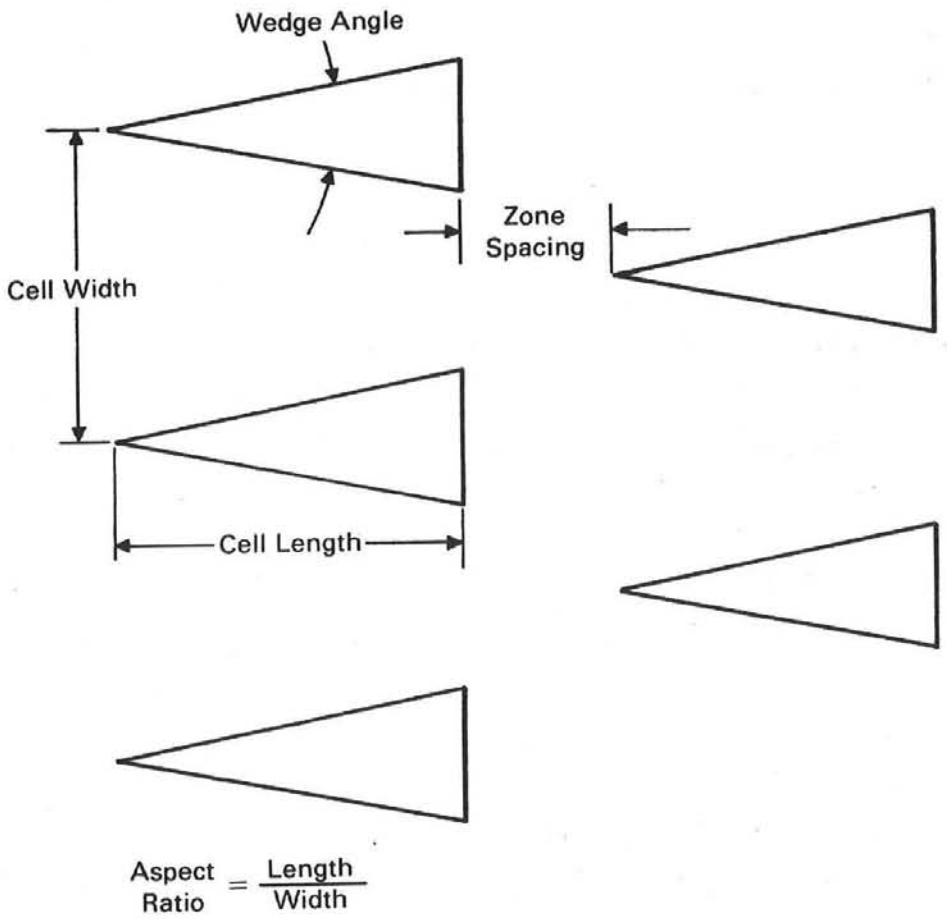

FIGURE 9.6. Parameters Which Characterize a Reflecting Row Zone

a three-reflecting-zone design. The results for the case 1 evaluations indicated that all case 1 designs were not feasible due to material temperatures exceeding the specified limit. Therefore, multiple-zone designs were not considered for this case.

Stage two consisted of simulating a number of two-zone designs. The design of the first zone was fixed, while that of the second zone was varied. The results indicated that the spacing between the two zones was not an important factor in determining the performance, so it was not included in the sensitivity study.

The results of the stage-two analysis indicated that the two-zone designs were not competitive with the one-zone design. But to determine the impact of adding successive reflecting zones, one three-zone case was investigated. The

results of the two-zone analysis for case 4 were reviewed and one two-zone configuration was selected for the first two zones of a three-zone design. The geometry of the first two zones was fixed while the aspect ratio and wedge angle of the third zone was varied. The results indicated that the three-zone case was even less attractive than a two-zone case.

The results of the various simulations indicated that the best performance was obtained with a large radius or a small image size. Either resulted in a reduction in the average incident angle of the insolation. Case 1 was rejected because much of the insolation had a large incident angle, which resulted in the insolation being either absorbed in the reflecting zone or reflected back to the surroundings. Based on these results, the base design was determined to have a radius of 10 m and a height of 5 m. The base case design was assumed to operate with a heliostat which produced a 2.0-m image (i.e. 95% of the heliostat's energy at the receiver would be contained in a circular image with a 2 m diameter).

With the selection of the base case dimensions, the reflection row design was identified by reviewing the results of the various simulations described above. Because of assumptions in calculating the zone temperature, the actual value of the zone temperature is less important than the trends indicated by the results.

The impact of successive reflecting zones on reflecting zone performance is shown in Figure 9.7. The results for the best one-, two-, and three-zone designs are plotted. Adding successive zone has a small effect on receiver losses but a dramatic impact on zone material temperature, where only the one-zone case has a maximum zone material temperature below 650 K, the assumed maximum allowable material temperatures. Based on these results, only one-zone designs, were considered further.

The impact of aspect ratio and wedge angle on losses and zone temperature is shown graphically in Figure 9.8. The influence of cell width on reflecting zone performance is shown in Figure 9.9. Both graphs are for the base case design but the specific values are less important than the general trends.

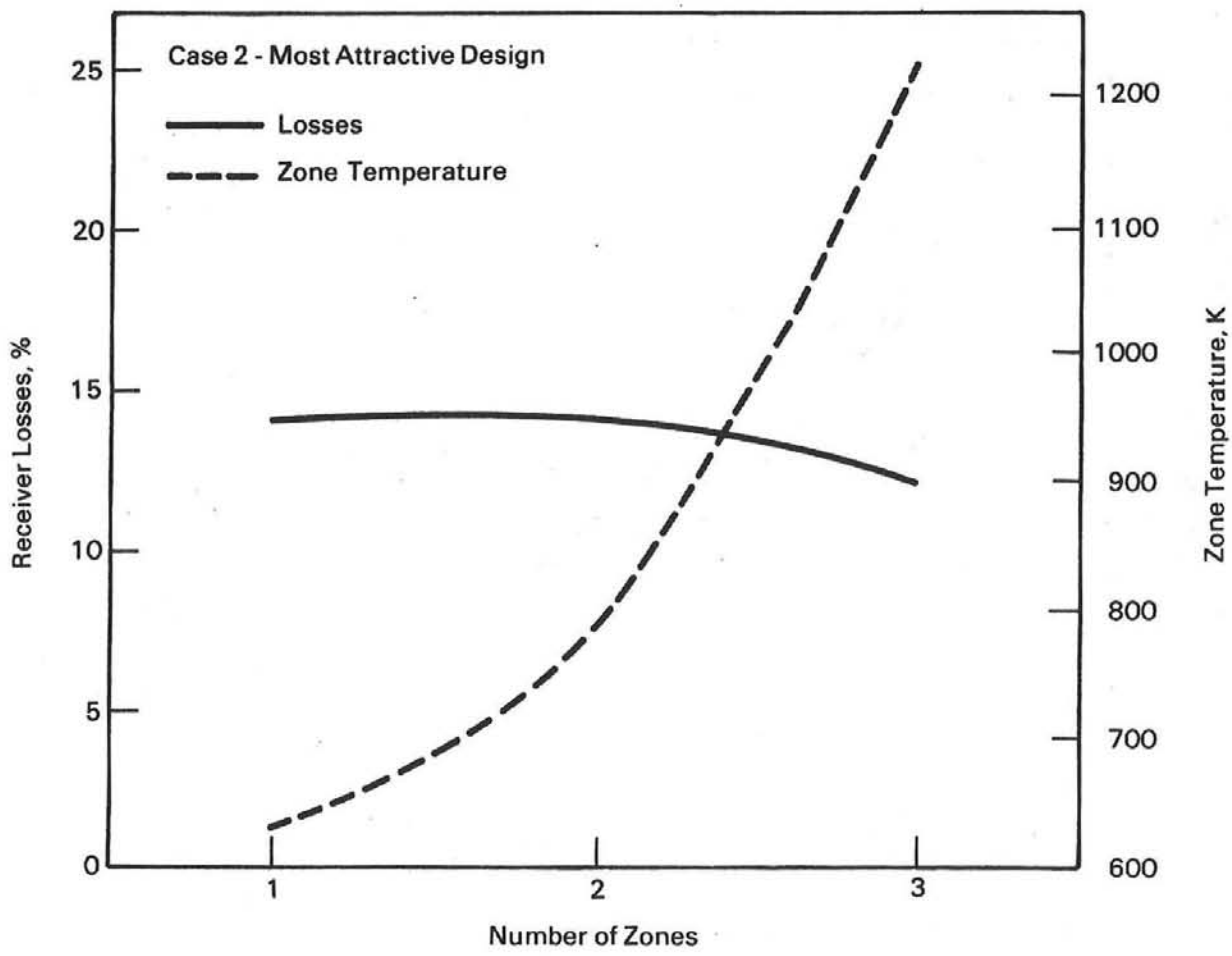

FIGURE 9.7. Impact of the Number of Reflecting Zones on Reflecting Zone Performance

The following conclusions were reached after evaluating the results of the various reflecting row designs considered in this study:

- The most attractive receiver consisted of a 10-m-radius, 5-m -tall receiver used with a heliostat which produces a 2-m-wide image. The 5-m-radius receiver is not feasible with existing heliostats (i.e. those with a 4-m-wide image).
- Multiple reflecting zones are not desirable. One reflecting zone is superior to two zones, which are in turn superior to three zones. Therefore, the base case design will have one row.

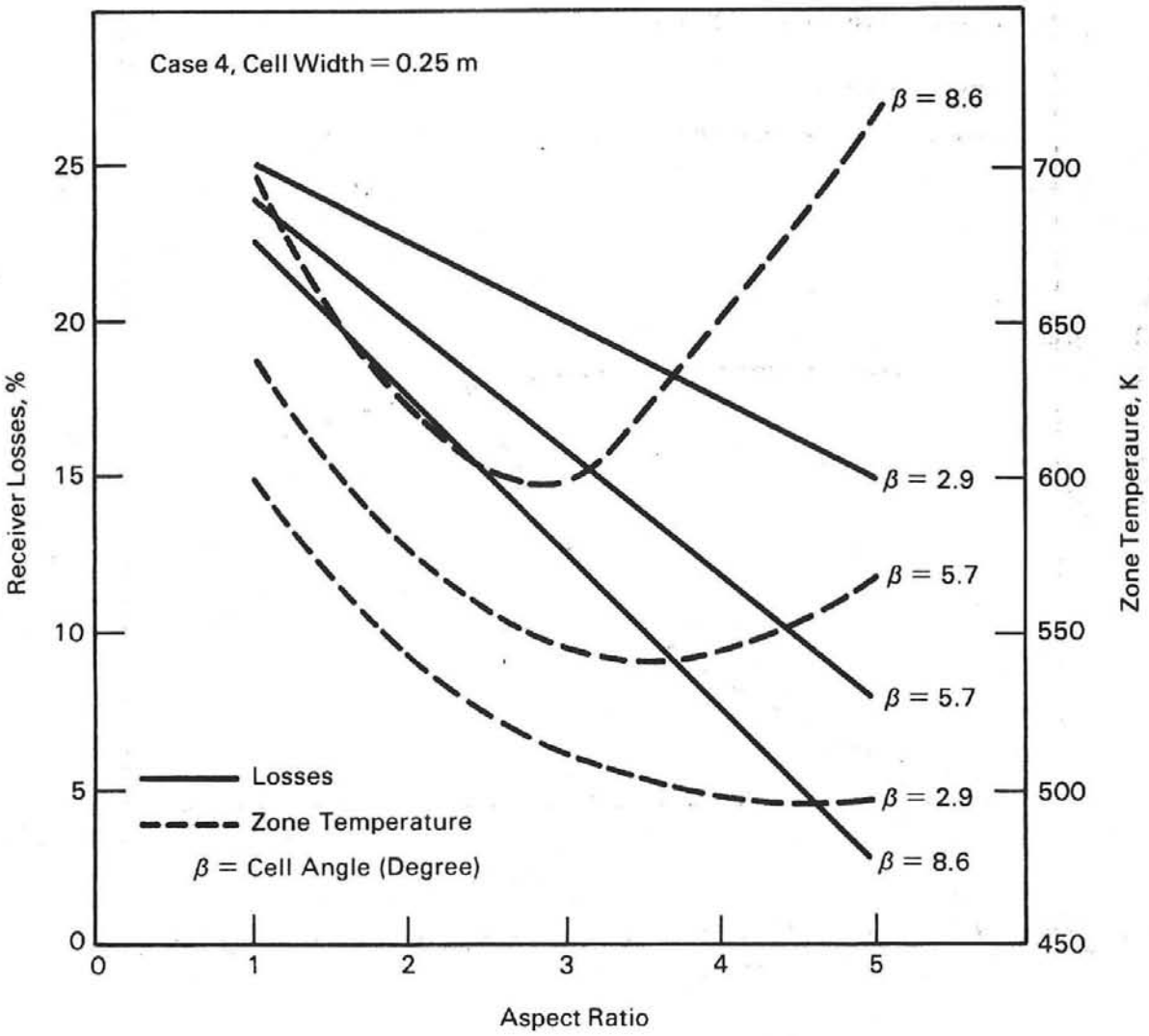

FIGURE 9.8. Influence of Aspect Ratio and Wedge Angle on Reflecting Zone Performance

- Increasing the aspect ratio will result in a decreased zone temperature because absorbed energy does not increase as rapidly as heat transfer area.
- Increasing wedge angle increases zone temperature and decreases reradiation. The increase in zone temperature is caused by increased absorption of incident radiation, whereas the absorption of reradiated energy is almost constant with wedge angle.

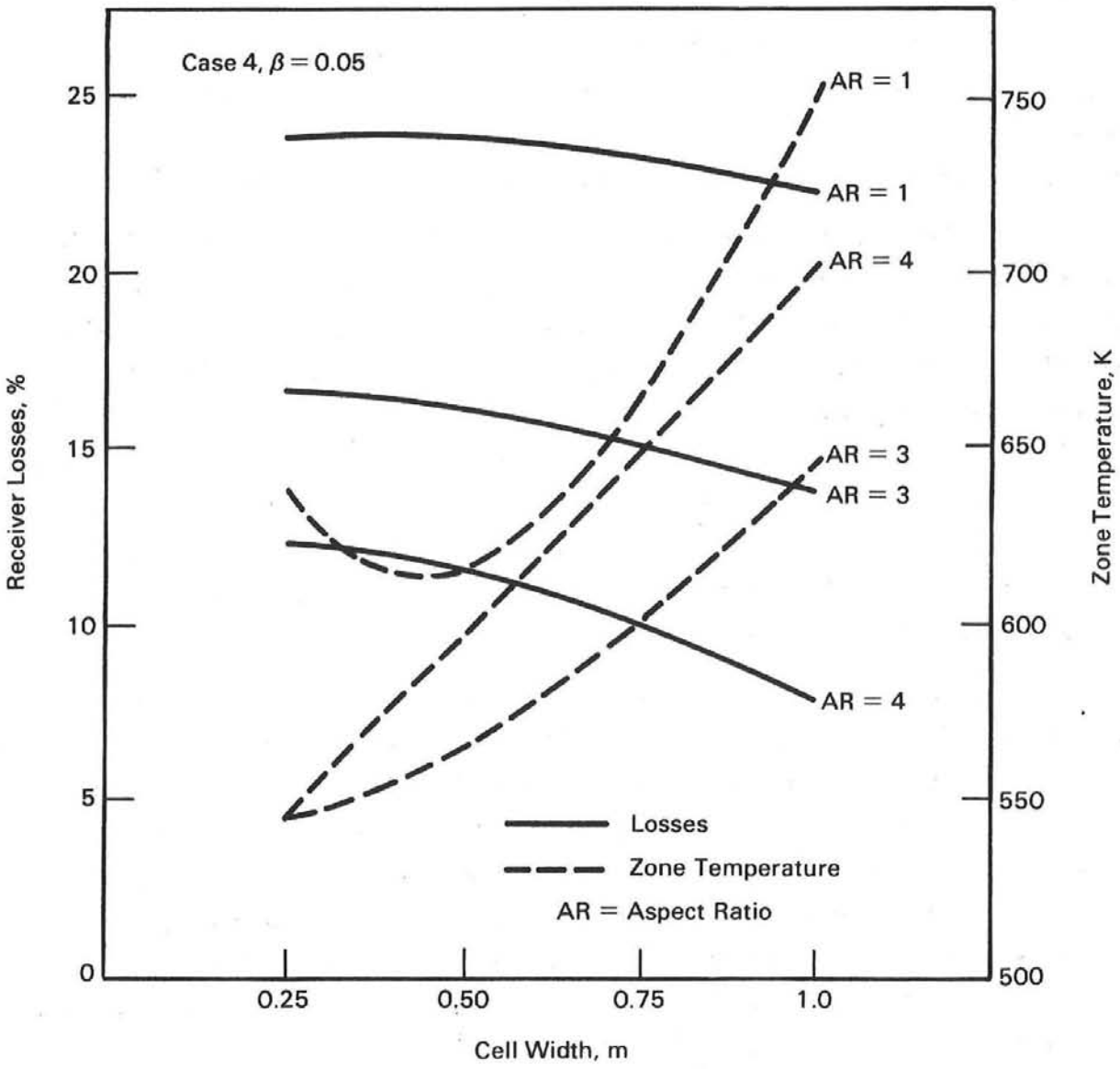

FIGURE 9.9. Impact of Cell Width on Reflecting Zone Performance

- When the aspect ratio is kept constant, zone temperature decreases and reradiation losses increase by decreasing the pin spacing.
- Based on the generic study, the most attractive reflecting row design consists of 1-m-long pins separated by 0.125 m and having a wedge angle of 3.5°.

Using the results of the generic study of reflecting rows, the base case reflecting row fiber design characteristics were specified (Table 9.12). The absorbing zone was selected after simulating several fiber arrays and selecting the design that resulted in the bulk of the energy being absorbed in the interior zones without an excessive amount reaching the terminal absorber.

The results for the base case design are presented in Table 9.13. The reflecting row fiber receiver will have a total receiver efficiency of 86.8%, a reflecting row flux ratio of 1.4, and a minimum fiber zone flux ratio of 3.9. The efficiency of this design is good, as is the fiber zone minimum flux ratio. But the reflecting row flux ratio is unacceptably low, even based on extremely optimistic assumptions (a reflecting row emissivity of 0.2 and an image size of 2 m). With such a low flux ratio, the reflecting row concept was dropped from further consideration. The nearly exhaustive investigation of reflecting row design suggests that little improvement can be expected by further optimization of the reflecting row concept.

Several sensitivity studies were conducted and the results are reported in Table 9.14. The impact of different product temperatures on receiver performance was investigated. Product temperatures of 1089 K (1500°F) and 811 K (1000°F) were considered and the results showed a substantial improvement in receiver efficiency, but the flux ratio for the reflecting row is only acceptable with a product temperature of 811 K (and these results are still based on the unreasonable emissivity and image size assumptions described above). It is unlikely, even at 811 K (1000°F), that a successful reflecting zone design can be obtained.

The impact of the image size assumption was investigated by assuming an image size of 4 m, the typical size for a second-generation heliostat (incident angle σ = 0.10 radians). The radiation distribution and exchange factors for the base case design were reevaluated using the VORRUM and VORVFM computer codes and the results used in the performance model. The design also includes a new reflecting zone design with 0.625-m-long fins spaced 0.25 m apart. The performance model demonstrates that using an image size of 4 m reduces the reflection row flux ratio to a disastrous 1.1.

TABLE 9.12. Reflecting Row Fiber Design Characteristics

Overall Characteristics

Receiver Height = 5.0 m
Receiver Radius = 10.0 m
Air Flow Rate = 42.8 kg/s
Product Design Temperature = 1367 K

Zone Characteristics

Zone No.	Type	Height, m	Depth, m	Fiber Spacing, m	Convection Area, m^2)	Radiation Area, m^2	Emissivity
1	Reflecting Fins[a]	5.0	1.0	0.125	5027	5027	0.2
2	0.0006 m dia fiber	5.0	1.7	0.013	37	37	0.9
3	" " " "	5.0	0.6	0.010	44	44	0.9
4	" " " "	5.0	0.6	0.008	50	50	0.9
5	" " " "	5.0	0.6	0.0051	68	68	0.9
6	" " " "	5.0	0.6	0.0037	82	82	0.9
7	" " " "	5.0	0.6	0.0024	106	106	0.9
8	" " " "	5.0	0.6	0.0011	169	169	0.9
9	" " " "	5.0	0.6	0.0006	211	211	0.9
10	" " " "	5.0	0.6	0.0002	278	278	0.9
11	Terminal Absorber	5.0	NA	NA	289	72	0.8

(a) 1-m-long with wedge half angle of 0.025 radius.

TABLE 9.13. Reflecting Row Fiber Design Performance Results

Zone	Zone Convective Heat Transfer Coefficient, W/m^2-K	Zone Material Temperature, K	Zone Air Exit Temperature, K	Zone Flux Ratio	Zone Insolation, %
1	6.89	567	444	1.4	7.5
2	357.46	695	509	4.6	3.8
3	377.88	765	588	4.3	5.0
4	413.90	810	669	4.7	5.1
5	451.42	882	772	4.7	7.0
6	497.10	977	891	4.5	8.9
7	551.60	1087	1028	4.1	12.3
8	605.96	1199	1177	3.9	17.1
9	665.48	1293	1286	4.1	16.3
10	717.17	1361	1359	4.1	12.1
11	5.00	1462	1362	2.3	3.0

Energy Balance	
Reflection Losses, W	1,104,273
Convection Losses, W	0
Reradiation Losses, W	6,544,765
Useful Power, W	50,406,165
Unaccounted Power, W	17,367
Total, W	58,072,572

Receiver Efficiency	
Receiver Absorptivity	0.981
Receiver Thermal Efficiency	0.885
Receiver Total Efficiency	0.868

TABLE 9.14. Reflecting Row Fiber Design Sensitivity Study Results

Base Case	Thermal Efficiency	Total Efficiency(a)	Minimum Flux Ratio for Fiber Zones	Reflecting Zone Flux Ratio
T = 1189 K σ = 0.05	0.952	0.934	6.3	2.2
T = 811 K σ = 0.05	0.979	0.960	6.7	2.8
T = 1367 K σ = 0.10	0.861	0.836	3.1	1.1

(a) Does not include convection or spillage losses.

9.4.2 Shroud

The failure of the reflecting zone concept to produce the anticipated high thermal efficiencies indicated that an alternate geometric loss reducer should be considered. A second method for reducing reradiation and reflection losses involves installing a shroud around the fiber core. This section describes the results of the evaluation of a shrouded receiver with a fiber core.

The base case design for a shrouded receiver with a fiber core was selected by considering a variety of fiber core designs and shroud configurations. Three fiber core designs were evaluated; a fiber core with a radius of 2.5 m, a fiber core with a radius of 3.75 m, and a fiber core with a radius of 5.00 m. Each design was analyzed using 1) the VORRUM computer code to predict the distribution of absorbed insolation and 2) the VORVFM computer code to predict the exchange factors between zones. Three core heights were considered for each core design, and each of these were combined with either two or four shrouds. This resulted in 11 designs for each fiber core. All designs were analyzed using the thermal performance code, and all assumed preswirl enhancement of convection. The results are presented in Tables 9.15, 9.16, and 9.17.

TABLE 9.15. Core Designs With 2.5-Meter Radius

Design	Receiver Radius, m	Receiver Height, m	Aperture Height, m	Receiver Efficiency, %	Flux Ratio
1	3.5	5.0	4.0	84	1.3
2	3.5	5.0	5.0	82	1.3
3	8.5	10.0	4.0	87	2.1
4	8.5	10.0	6.0	83	2.1
5	8.5	10.0	8.0	80	2.1
6	8.5	10.0	10.0	79	2.1
7	13.5	15.0	4.0	87	2.7
8	13.5	15.0	6.0	85	2.7
9	13.5	15.0	7.0	82	2.7
10	13.5	15.0	10.0	78	2.7
11	13.5	15.0	15.0	74	2.6

TABLE 9.16. Core Designs With 3.75-Meter Radius

Design	Receiver Radius, m	Receiver Height, m	Aperture Height, m	Receiver Efficiency, %	Flux Ratio
1	4.75	5.0	4.0	85	2.0
2	4.75	5.0	5.0	83	2.0
3	9.75	10.0	4.0	86	2.9
4	9.75	10.0	6.0	82	2.8
5	9.75	10.0	8.0	79	2.9
6	9.75	10.0	10.0	78	2.9
7	14.75	15.0	4.0	83	3.6
8	14.75	15.0	6.0	80	3.5
9	14.75	15.0	7.0	77	3.5
10	14.75	15.0	10.0	73	3.4
11	14.75	15.0	15.0	70	3.4

TABLE 9.17. Core Designs With 5.0-Meter Radius

Design	Receiver Radius, m	Receiver Height, m	Aperture Height, m	Receiver Efficiency, %	Flux Ratio
1	6.0	5.0	4.0	85	2.4
2	6.0	5.0	5.0	83	2.4
3	8.5	7.5	4.0	85	3.0
4	8.5	7.5	5.0	83	3.0
5	8.5	7.5	6.0	81	3.0
6	8.5	7.5	7.5	80	3.1
7	11.0	10.0	4.0	83	3.6
8	11.0	10.0	6.0	80	3.6 (Base Case)
9	11.0	10.0	8.0	77	3.6
10	11.0	10.0	10.0	76	3.6

The base case was selected by reviewing the results and picking the most attractive design. Two restrictions were imposed on the selection. First the aperture height had to be at least 6.0 meters. This aperture area exceeds the size of the largest heliostat image, which should result in low spillage

losses. Secondly, the base case minimum flux ratio was assumed to be at least 3.0. The impact of a lower minimum flux ratio was considered in the sensitivity study. With these restrictions, the base case design consisted of a receiver with a 5-m-radius core, a height of 10 meters, and an aperture height of 6 meters. The base case was assumed to include a shroud without packing. The characteristics of the base case design are presented in Table 9.18.

The shroud design used with all shroud concepts is shown in Figure 9.10. The design is based on several simplifying assumptions. First, the aperture was assumed to be located solely on the side of the shroud. A more attractive design may have reduced the aperture height and reduced the radius of the shroud floor. The difficulty in predicting the exchange factors for this case forced the restriction on the shroud design. The distance between the core and the shroud was selected based on the 4-meter-aperture design and the design of the heliostat field. The image from the closest heliostats will strike the plane of the aperture with an angle of approximately 45°. The image from the most distant heliostat will strike the plane of the aperture with an angle of approximately 9°. To insure that some insolation would strike the top of the receiver core, the spacing between the core and the shroud must equal the receiver height minus the aperture height. Due to the two-dimensional nature of the analysis, the interaction of insolation on the top of the shroud is ignored. The shroud spacing was kept constant for various aperture heights. The impact of varying the spacing was investigated in the sensitivity study. In all cases the image from the nearest heliostat was required to strike the top of the fiber core.

The results for the base case design are presented on Table 9.19. The base case shrouded fiber design has a total receiver efficiency of 79.8% and a minimum flux ratio of 3.4. The flux ratio of 3.4 is acceptable.

The zone convective heat transfer coefficient is also of interest. The shroud convective heat transfer coefficient of 9.2 W/m^2-K is based on natural convection from the shroud walls. For the fiber zones, the convective heat transfer coefficient varies from 309.5 W/m^2-K to 629.6 W/m^2-K, demonstrating the very high heat transfer for augmented forced convection from small fibers. The convective heat transfer coefficient for the terminal absorber was

TABLE 9.18. Shrouded Fiber Design Characteristics

Overall Characteristics

Receiver Height = 10 m
Receiver Radius = 11 m
Air Flow Rate = 42.8 kg/s
Product Design Temperature = 1367 K

Aperture Height = 6.0 m
Blocking Factor = 0.05
Shroud Fill = None

Zone Characteristics

Zone No.	Type	Height, m	Depth, m	Fiber Spacing, m	Convection Area, m^2	Radiation Area, m^2	Emissivity
1	Shroud	10.0	6.0	NA	879	879	1.0
2	0.0006-m-dia fiber	10.0	0.3	0.016	34	34	0.9
3	" " " "	10.0	0.3	0.012	43	43	0.9
4	" " " "	10.0	0.3	0.009	52	52	0.9
5	" " " "	10.0	0.3	0.0055	76	76	0.9
6	" " " "	10.0	0.3	0.0039	96	96	0.9
7	" " " "	10.0	0.3	0.0024	132	132	0.9
8	" " " "	10.0	0.3	0.0011	212	212	0.9
9	" " " "	10.0	0.3	0.0006	271	271	0.9
10	" " " "	10.0	0.3	0.0001	415	415	0.9
11	Terminal Absorber	10.0	NA	NA	578	144	0.9

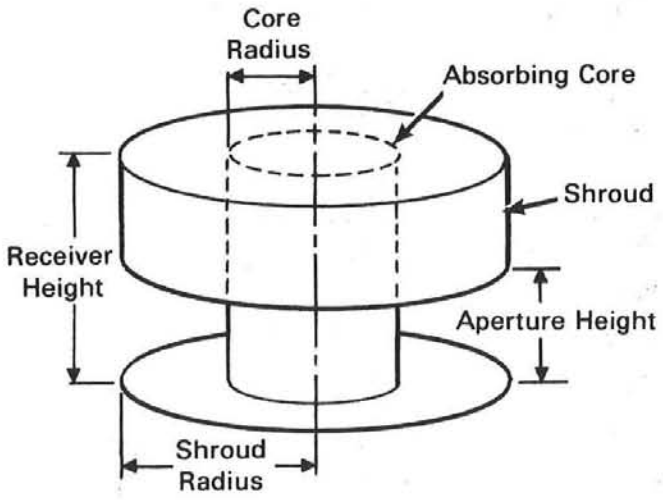

Schematic of Shroud

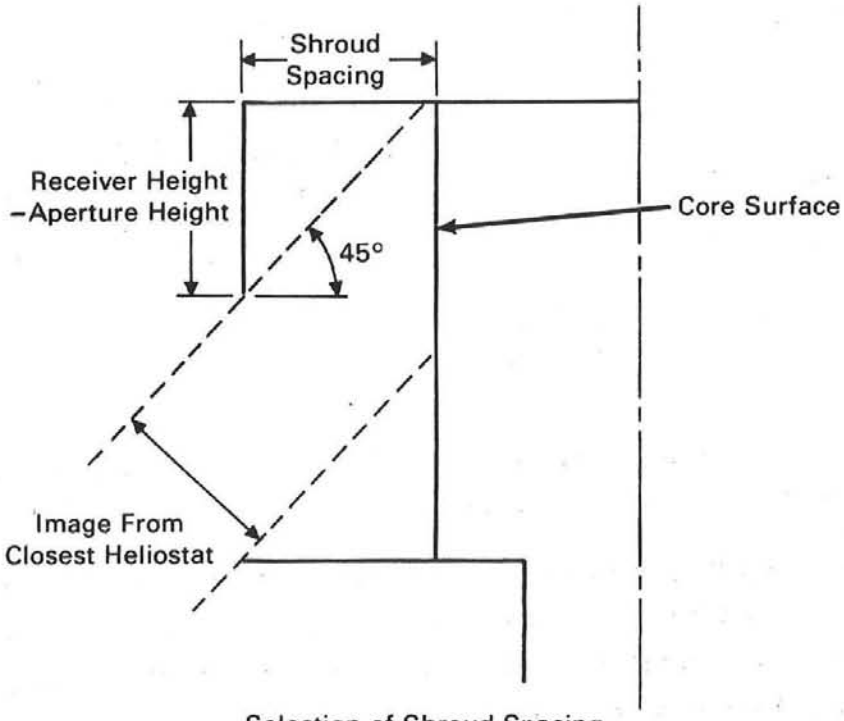

Selection of Shroud Spacing

FIGURE 9.10. Details of the Shroud Design

TABLE 9.19. Shrouded Fiber Design Performance Results

Insolation, Zone	Heat Transfer Coefficient, W/m^2-K	Zone Temperature Distribution: Zone Material Temperature, K	Zone Temperature Distribution: Zone Air Exit Temperature, K	Zone Flux Ratio	Absorbed %
1	9.2	818	384	2.9	3.5
2	309.5	663	444	4.1	3.0
3	332.9	733	525	3.8	4.5
4	367.4	812	625	3.6	5.8
5	408.1	906	764	3.5	8.4
6	452.1	1000	906	3.7	10.1
7	500.4	1115	1061	3.6	13.9
8	549.3	1230	1213	3.5	18.9
9	592.7	1315	1311	3.9	17.6
10	629.6	1362	1362	5.2	11.6
11	5.0	1367	1362	46.5	0.7

Energy Balance	
Reflection Losses, W	1,238,923
Convection Losses, W	0
Reradiation Losses, W	11,542,768
Useful Power, W	50,383,864
Unaccounted Power, W	110,460
Total, W	63,276,014

Receiver Efficiency	
Receiver Absorptivity	0.980
Receiver Thermal Efficiency	0.814
Receiver Total Efficiency	0.798

conservatively assumed to be 5.0 W/m^2-K. The material and air temperature distribution and flux ratio are shown graphically in Figure 9.11.

The base case design was the subject of a variety of sensitivity studies. Each one examined the impact of a design variable on the performance of the receiver. The first sensitivity study examined the impact of varying the maximum tangential velocity of the air in the receiver. Four cases were considered; the base cases with the maximum tangential air velocity equal to 30 m/s and the other cases with maximum tangential air velocity at 6 m/s, 18 m/s, and 42 m/s. The normalized air velocity profile was assumed to be constant for all four cases.

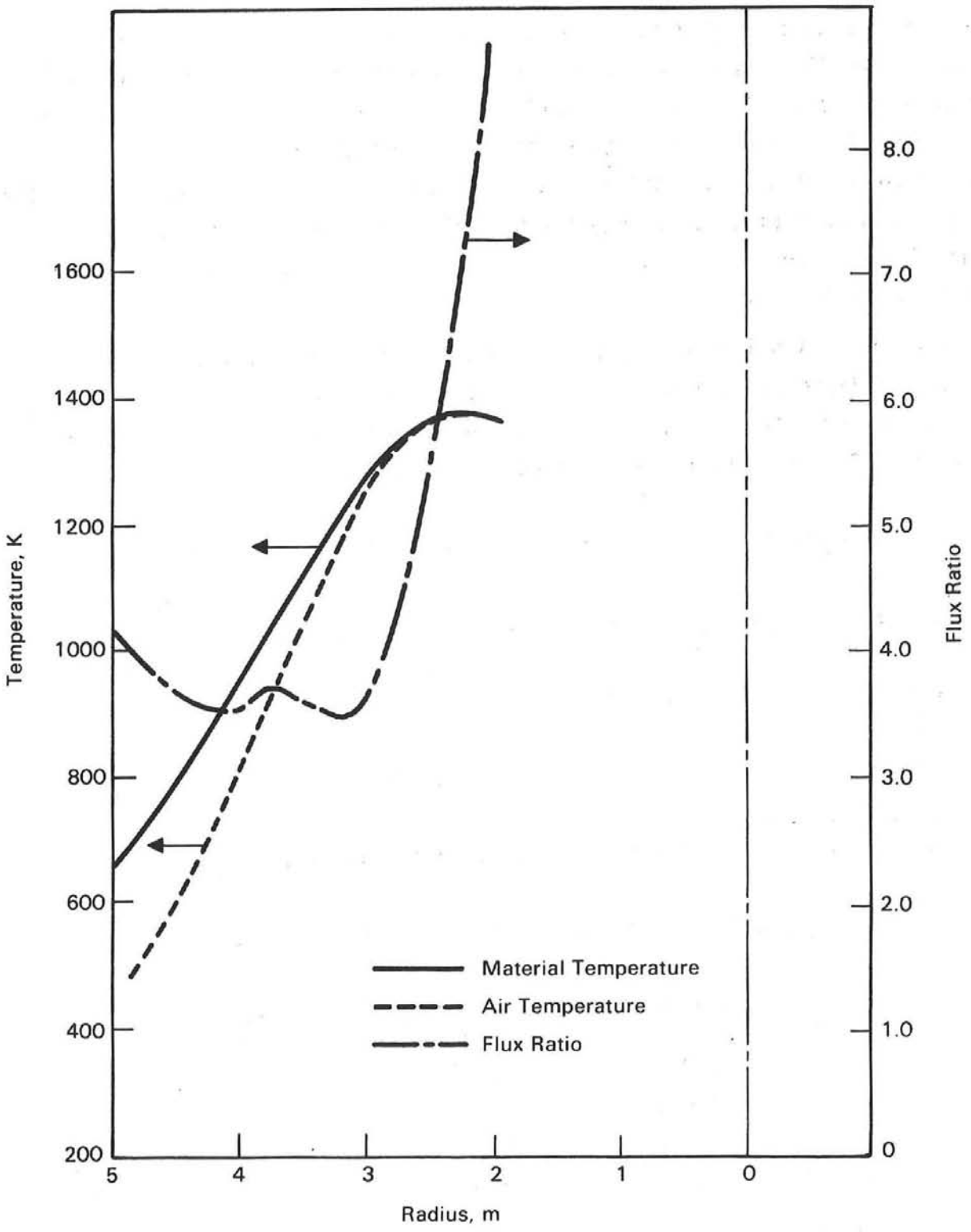

FIGURE 9.11. Temperature Distributions for the Base Case Shrouded Fiber Design

The results presented in Table 9.20 indicate that reducing the maximum air velocity from 30 m/s to 18 m/s has a negligible impact on the receiver efficiency but does result in a 9% reduction in minimum flux ratio. The 6-m/s case has a more significant drop in both efficiency and minimum flux ratio. The 42-m/s case results in an insignificant increase in efficiency and minimum flux ratio. This sensitive study suggests that the swirl velocity can be varied to reduce flow-induced fiber vibrations as long as the maximum velocity is above approximately 18 m/s.

The second sensitivity study deals with fiber diameter, which can have a substantial impact on the convective heat transfer coefficient. Four cases were considered: the base case, and designs with fiber diameters of 0.0003 m, 0.0012 m, 0.0020 m. The results are summarized in Table 9.21.

TABLE 9.20. Swirl Velocity Sensitivity Study Results

Case	Maximum Velocity (m/s)	Receiver Efficiency[(a)]	Minimum Flux Ratio
Base	30.0	0.798	3.4
Case 1	6.0	0.767	2.2
Case 2	18.0	0.791	3.1
Case 3	42.0	0.801	3.7

(a) Does not include convection or spillage losses.

TABLE 9.21. Fiber Diameter Sensitivity Study Results

Case	Fiber Diameter, m	Receiver Efficiency[(a)]	Minimum Flux Ratio
Base	0.0006	0.798	3.4
Case 1	0.0003	0.807	4.1
Case 2	0.0012	0.781	2.6
Case 3	0.0020	0.761	2.1

(a) Does not include convection on spillage losses.

The fiber diameter primarily affects the minimum flux ratio, where a doubling of the fiber diameter results in a 25% reduction in the minimum flux ratio.

This suggests that there is not much benefit from increasing the fiber diameter to improve the structural characteristics of the fiber. It should be noted that an increase in fiber diameter from 0.006 m to 0.0012 m increases the breaking strength from approximately 44.5 N (10 lbf) to 186.8 N (42 lbf).

Energy convected from the surface of the shroud may not be lost as in other cavity designs because the heated air is drawn into the receiver. Convection from the shroud to the air entering the receiver for the base case design was calculated based on the interior surface area of the shroud, sides, roof, and floor. Convection was assumed to be limited to natural convection. To investigate the impact of adding a fiber packing to the shroud, two additional cases were considered. In the first case enough fiber packing was added to provide 4000 m^2 of heat transfer area with a convective heat transfer coefficient based on natural convection from a fiber. The second case was similar except that 8000 m^2 of heat transfer area was added. Figure 9.12 shows the proposed location of the fiber packing. The results are summarized in Table 9.22.

The results indicate a substantial performance improvement when fiber packing with 4000 m^2 of surface area is added. There is a 21% reduction in losses and a 10% improvement in flux ratio. Adding 4000 m^2 of surface area would result in the fibers filling 0.55% of the volume of the shroud with a fiber spacing of 0.0677 m or 13.5 diameters. The wide spacing should reduce the interference of one fiber with another. The total mass of the 0.005-m diameter fibers is estimated to be approximately 20,000 kg. The case with 8000 m^2 of surface area shows that additional packing above 4000 m^2 results in insignificant improvement in either receiver efficiency or flux ratio with a substantial increase in fiber mass.

One method for reducing receiver thermal losses is to block a fraction of the circumferential area of the shroud aperture. An example of aperture blocking is shown in Figure 9.13 where 1/3 of the aperture is blocked. The blocked area can either be combined in one area as shown in the figure or be divided into two or more areas with apertures located between the blocked areas. The

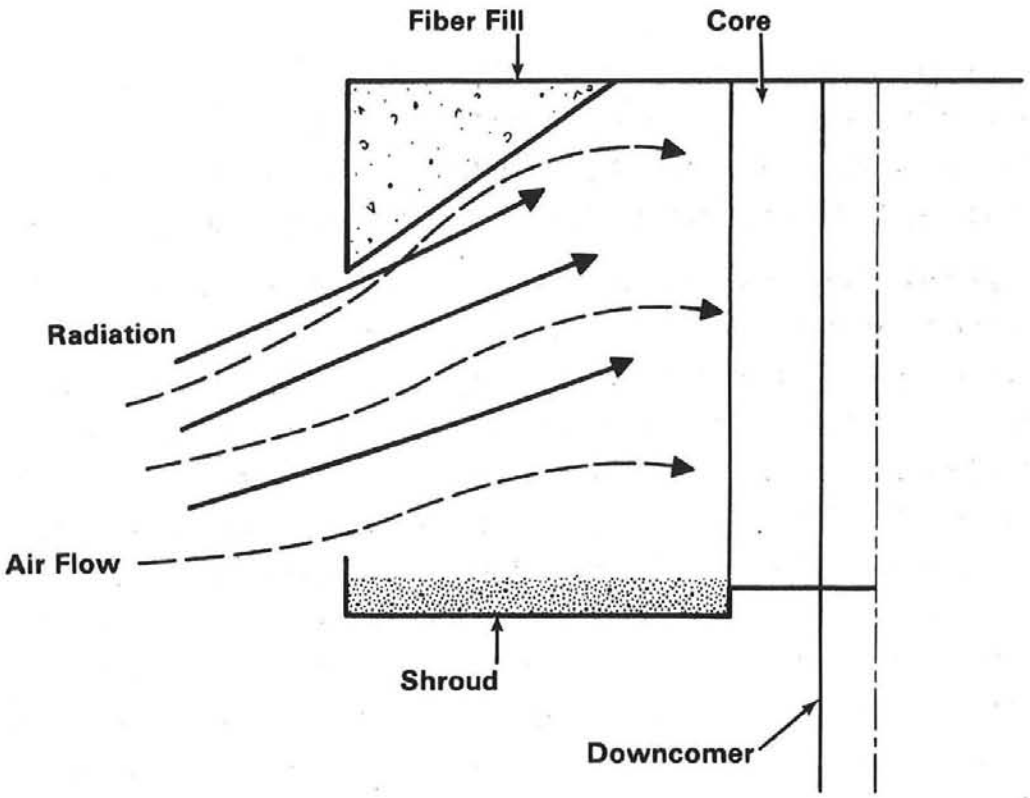

FIGURE 9.12. Shroud With Packing

TABLE 9.22. Impact of Fiber Packing on Receiver Performance

Packing Area Case	Heat Transfer Coefficient, W/m^2-K	Receiver Efficiency,(a) %	Minimum Flux Ratio	Fiber Packing Volume Fraction, %	Fiber Spacing, m	Fiber Mass, kg
Base Case	9.2	79.7	3.4	--	--	--
4000 m^2	20.4	83.9	3.7	0.55%	0.0677	20,000
8000 m^2	19.3	84.2	3.8	1.10%	0.0479	40,000

(a) Does not include convection or spillage losses.

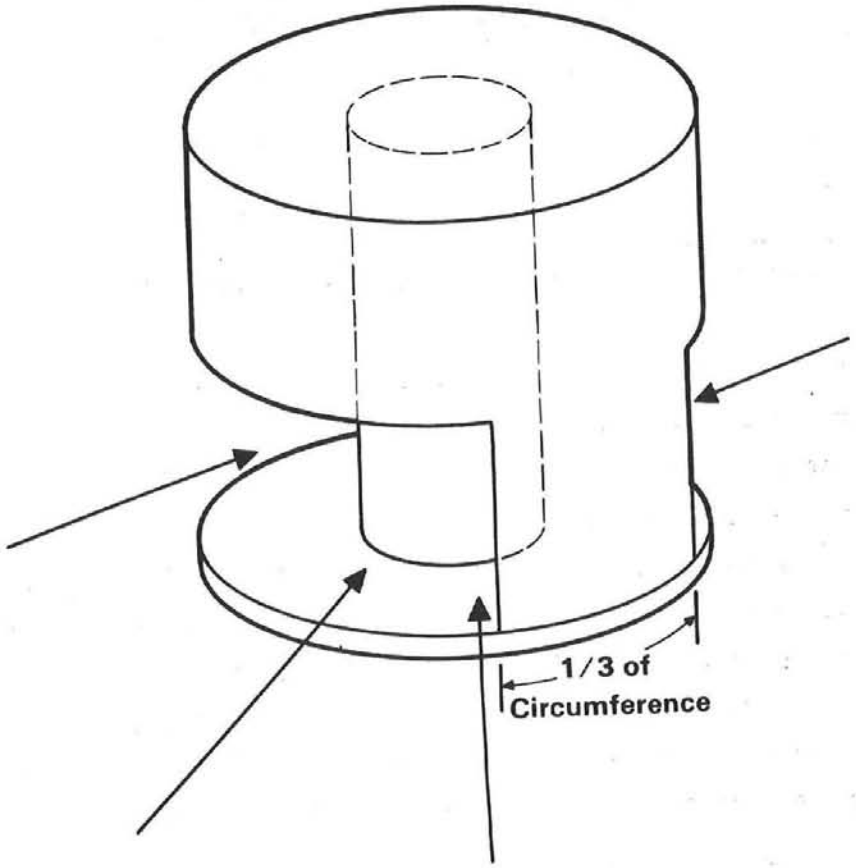

FIGURE 9.13. Shroud With Aperture Blocking

base case assumes that 5% of the aperture area is blocked. The blocked area is assumed to provide structural support for the roof. Two additional cases were considered; one involved aperture blocking 25% of the aperture area while the second involved blocking 50% of the aperture area.

The results, presented in Table 9.23, indicate that aperture blocking can increase the receiver efficiency, but at the cost of decreasing the flux ratio. This is caused by concentrating the flux, which is spread over the whole aperture area, into a smaller area. Consequently the average flux is increased by a factor equal to 1/(1.0-Aperture Blocking).

As indicated earlier, the distance between the absorbing core and the shroud can be reduced to where it equals the receiver height minus the aperture

TABLE 9.23. Impact of Aperture Blocking

Case	Aperture Blocking Fraction	Receiver Efficiency(a)	Flux Ratio
Base	0.05	0.797	3.4
Case 1	0.25	0.819	2.7
Case 2	0.50	0.857	1.8

(a) Does not inlcude convection or spillage losses.

height. This would still allow the image from the closest heliostat to strike the top of the absorbing area. The base case has a shroud spacing of 6.0 m, an aperture height of 6.0 m, and a receiver height of 10.0 m, so the minimum shroud spacing would be 4.0 m. Two cases in addition to the base case were considered: one with shroud spacing of 5.0 m and one with a shroud spacing of 4.0 m. The advantage of reducing the shroud spacing is that it results in a receiver with a smaller overall radius. This would result in lower shroud and tower cost, and reduced wind loading. The results presented in Table 9.24 indicate that over the range of shroud spacings considered the shroud spacing has a negligible impact on either efficiency or flux ratio.

The volumetric receiver may be used to produce hot air at temperatures other than 1367 K. To investigate the impact of product temperature on

TABLE 9.24. Impact of Shroud Spacing

Case	Shroud Spacing, m	Receiver Efficiency(a)	Minimum Flux Ratio
Base	6	0.799	3.4
Case 1	5	0.797	3.4
Case 2	4	0.797	3.4

(a) Does not include convection on spillage losses.

receiver efficiency, two additional cases were considered: one with a product temperature of 1089 K (1500°F) and one with 811 K (1000°F). The results are shown in Table 9.25. As expected, the lower product temperature results in a substantial improvement in efficiency and a minimum flux ratio. The high minimum flux ratio suggests that a substantial fraction of the aperture area can be blocked without exceeding a minimum flux ratio of 3.0. This would further improve the receiver efficiency. Case 2A in Table 9.25 is a design for producing 811 K air with a blocking factor of 0.5.

The most attractive shrouded fiber design would include shroud packing and aperture blocking. Aperture blocking can improve receiver efficiency but at the cost of decreasing flux ratio, so two situations were considered: one where the minimum flux ratio was 3.0 and one where the minimum flux ratio was 2.0. The base case design was included in each comparison. In addition, three other cases were included in the situation where the minimum flux ratio was limited to 2.0. The results are presented in Table 9.26.

The results indicate that if a minimum flux ratio of 3.0 is acceptable, then a receiver efficiency of 86.9% can be expected. If a minimum flux ratio of 2.0 is acceptable, then an efficiency of 88% to 89% can be expected. The four cases with a flux ratio of 2.2 show that a variety of different designs can obtain equivalent performance and minimum flux ratio. A selection between these four cases would have to be based on an economic evaluation of the receiver.

TABLE 9.25. Impact of Product Temperature

Case	Product Temperature, K	Air Mass Flow Rate, kg/s	Receiver Efficiency[(a)], %	Minimum Flux Ratio
Base	1367	42.8	0.797	3.4
Case 1	1089	58	0.906	5.4
Case 2A	811	92	0.948	6.2
Case 2	811	92	0.968	3.2

(a) Does not include convection or spillage losses.

TABLE 9.26. Impact of Aperture Blocking and Core Radius

Case	Core Radius, m	Receiver Height, m	Aperture Height, m	Aperture Blocking Fraction	Receiver Efficiency[a], %	Minimum Flux Ratio
Base	5	10	6	0.25	0.864	3.0
Base	5	10	6	0.45	0.890	2.2
Case 1	5	7.5	6	0.35	0.883	2.2
Case 2	3.75	10.0	6	0.30	0.887	2.2
Case 3	2.5	15.0	6	0.25	0.891	2.2

(a) Does not include convection or spillage losses.

9.5 FINAL VAHR DESIGN

As a result of the studies described in this chapter, we developed a final preconceptual design for the volumetric air heating receiver. This design consists of an array of ceramic fibers forming the interior absorbing surfaces of the receiver, a series of slotted pipes judiciously arranged around the perimeter of the receiver to induce a preswirl of air, and a shroud to house the core. The following list summarizes the characteristics of the preconceptual design for the VAHR.

Shroud Diameter (Nominal)	22 m
Receiver Height (Nominal)	10 m
Shroud Aperture	6 m
Absorbing Core Diameter	10 m
Downcomer Diameter	4.6 m
Fiber Diameter	0.6 mm
Fiber Packing Density (Average)	1140 Fibers/m^2
Maximum Air Tangential Velocity	30 m/s
Slotted Pipe Diameter	0.4 m
Number of Slotted Pipes	35

Table 9.27 summarizes the thermal performance for this design. The combined reflection and reradiation losses total 18%, leaving a thermal efficiency (disregarding convection and spillage losses) of 82%. The auxiliary power necessary to operate the fans is around 550 kW. Several performance quantities are not listed in the table. Without any capability for calculating heliostat field optical performance, we were unable to estimate spillage losses for this design. Although spillage loss estimates are available for cavity receivers, the shroud concept differs significantly from a cavity in that the aperture is circumferential. Therefore, cavity spillage estimates may not be a good indication of the spillage experienced with the VAHR design. Similarly, tools for evaluating convective losses for the shroud concept were not available, so estimates are not given. Finally, the theoretical power requirements of fans for providing the air jets are negligible.

TABLE 9.27. Thermal Performance of the 50-MWt VAHR Producing Air at 1367 K

Reflection Losses	1.5%
Reradiation Losses	17%
Convection Losses	(a)
Total Thermal Losses	(a)
Spillage Losses	(a)
Auxiliary Power Requirements	
Air Movers	550 kW
Inducing Preswirl	Negligible

(a) Estimation of these values was beyond the scope of this study.

9.6 PROBLEMS AND UNCERTAINTIES WITH THE VAHR

Several problem areas and areas of uncertainty exist with the VAHR. Most notably, these areas center around fiber integrity, preswirl generation, and the shroud design. In addition, during the design evolution of the VAHR the design concept was forced by design considerations away from the qualitative advantages that originally made the concept look so attractive. The problems with the VAHR are discussed in this section, while the issue of qualitative advantages is discussed in Section 2.

Fiber survivability is a major concern with any ceramic fiber VAHR design. Because of the intermittent nature of high-temperature solar energy systems and the relative velocity of air past the fibers, the fibers are subjected to a harsh environment and must withstand both mechanical stress from flow-induced vibration and thermal stress as a result of high fluxes and thermal cycling. These concerns have not been addressed in this study. Before fibers can be recommended for such an application, research is needed to establish the mechanical and thermal properties of these ceramic fibers under such harsh conditions to determine if they are suitable for this application.

One major uncertainty existing in the preswirl technique for convective enhancement deals with obtaining adequate velocities and suitable flow distributions. The theory of slotted jets is not well developed, and there is no theory or practical experience with jets in series. As a result, only a cursory analysis of the technique could be made, and the use of a slot model was extended well beyond the model's validity. Therefore, the velocities predicted for the preswirl are very rough estimates with a substantial uncertainty associated with them. As for flow distribution, the placement of the slotted pipes out of the direct flux from the heliostat field would add to the difficulties of obtaining a uniform swirl. Flow nonuniformities would occur, which might lead to hot spots in the receiver. To address the fluid mechanics problems, substantial experimental R&D will be required before reliable performance predictions can be made.

Two areas of uncertainty regarding the shroud design remain. As mentioned earlier, spillage and convection losses have not been estimated. As a result, the overall receiver performance of the VAHR design is subject to question.

Also, although Monte Carlo techniques were available to predict the distribution of insolation absorbed for the reflecting row receiver designs, no such capability exists for the shroud designs.

10.0 TRANSPORT SYSTEM DESIGN

The transport system starts with the downcomer at the base of the receiver and ends at the base of the receiver tower with an air-to-air heat exchanger (checker stove or recuperator) and air mover (fan, blower, or compressor). No overland transportation equipment is included past the the base of the tower. The task of moving 2000°F air presents several difficulties: 1) the high-temperature, low-pressure air stream created by the volumetric receiver is extremely voluminous, which requires very large air handling equipment; 2) even state-of-the art air moving equipment must be isolated from the hot product stream with a heat exchanger; and 3) the power requirements for moving large quantities of warm air at any significant pressure ratio are enormous.

The objective of the transport system design task was to develop a reasonable approach to transporting the air. The level of effort did not allow for optimization of the system, but several design tradeoffs were analyzed. Design tradeoffs evaluated included the approach temperature for the air-to-air heat exchanger, the use of a two-stove, checker stove system versus a recuperator for the air-to-air heat exchanger, and the use of a single air mover and intercooler versus two air movers. In all cases, the preferred design was chosen based on consideration of both cost and performance. Schematic drawings of the principal configurations considered are shown in Figures 10.1, 10.2 and 10.3.

An air-to-air heat exchanger is required to isolate the air mover (fan, blower, or compressor) from the hot gas product stream. A checker stove system, in which energy charging and discharging cycle from one stove to another, can meet this need, as can a recuperator. The checker stove system can help smooth out transients in energy delivery (which the recuperator cannot) but the system costs about twice as much as the recuperator. The size and cost of either heat exchanger will rise inversely proportional to heat exchanger approach temperature. A product air temperature of 1800°F (at the outlet of the transport system) was chosen as a design point for sizing and costing both types of heat exchangers.

The choice of air moving systems depends largely on the pressure drop of the system, which, in turn, is largely dependent on the pressure drop in the

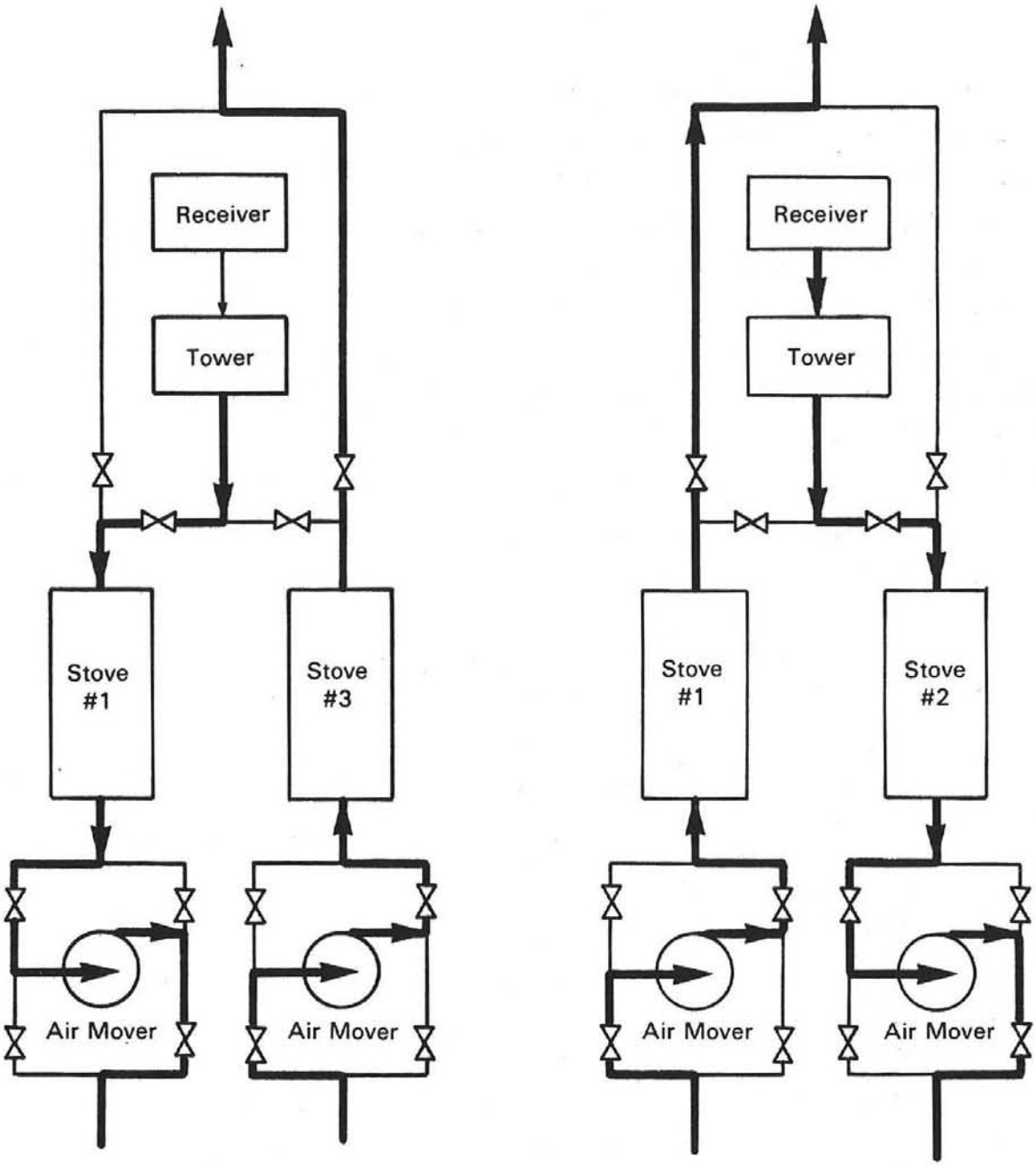

FIGURE 10.1. Transport System With Checker Stove and Two Air Movers

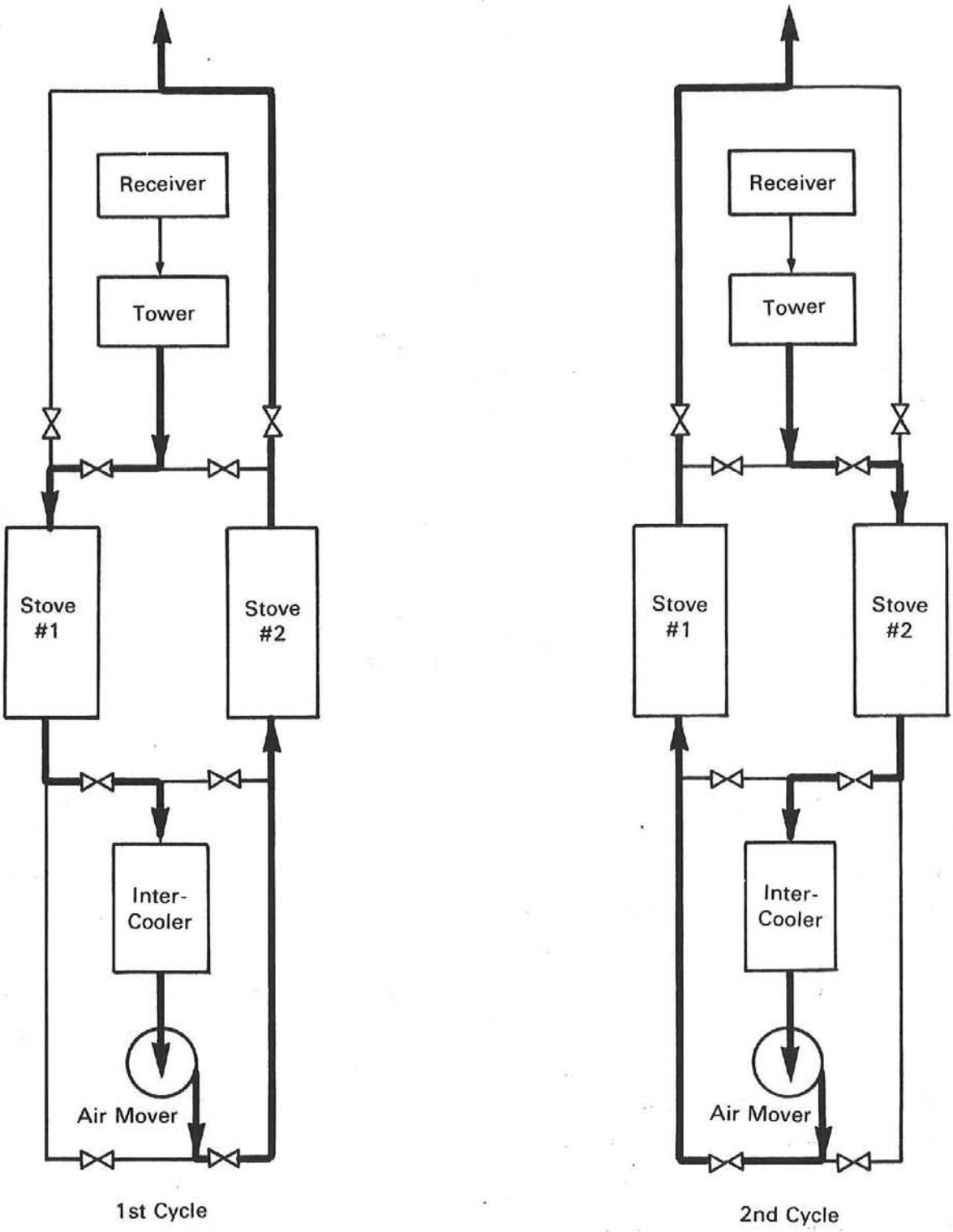

FIGURE 10.2. Transport System With Checker Stove, Intercooler, and One Air Mover

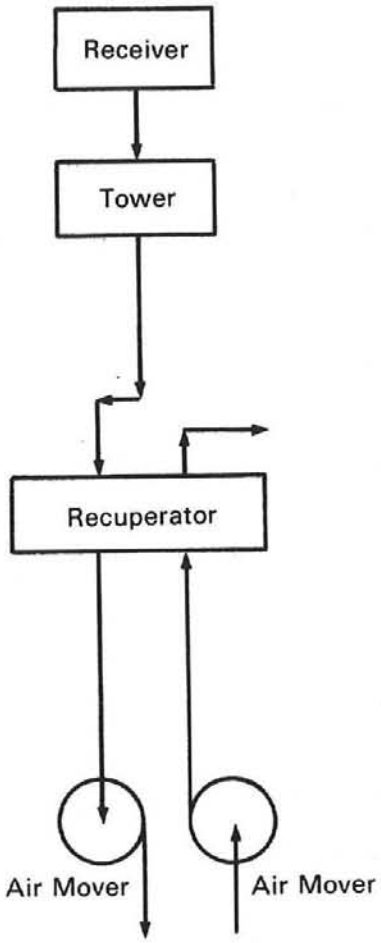

FIGURE 10.3. Transport System With Recuperator and Two Air Movers

receiver. The impact of higher pressure ratios is magnified by the fairly warm inlet temperatures encountered, even on the "cold" side of the air-to-air heat exchanger. At a certain pressure ratio, intercoolers become a cost effective way of reducing both the capital and operating costs of air movers. An intercooler system, as depicted in Figure 10.2, eliminates the need for one of the air movers. Alternatively, the inlet temperature to the "hot side" air mover could be reduced by adding heat transfer area to the air-to-air heat exchanger. While this would increase the overall effectiveness of heat transfer, it may be too expensive to remove this incremental amount of energy with the air-to-air heat exchanger rather than a water-cooled intercooler.

Receiver air flow modeling indicated that pressure losses would be minimal; therefore, the need to minimize air mover costs with an intercooler was

eliminated. The low pressure drop estimated for the volumetric receiver also indicated that a fan or blower would be adequate. Design details for the downcomer, air mover, and air-to-air heat exchangers are presented in the following subsections.

10.1 DOWNCOMER

The downcomer provides an air transport pathway from the receiver to the base of the tower. Downcomer design involves a tradeoff of capital costs versus performance. Larger diameters minimize pressure loss but increase heat transfer surface area and are more expensive. Smaller diameter downcomers are cheaper to build and have less heat transfer surface, but will increase the pressure loss. The four principal components of the downcomer are the structural shell, insulation, heat resistant liner, and expansion joints. The selected design is based loosely on information given in previous reports (Boeing; Gibbs and Hill 1981; De Laquil et al. 1983).

The structural shell forms the exterior of the downcomer and supports the other components. The shell is not subject to a significant pressure load; in fact, the interior pressure is slightly subatmospheric. A pipe could be used for the shell, but at the diameter required for the volumetric receiver (~15 feet), the pipe wall would have to be rather thick just to support its own weight. A multisided structural steel frame with a sheet metal skin is an alternative, if a large-diameter pipe proves infeasible. A detailed mechanical design would be necessary to establish the more appropriate of these two possibilities.

Insulation is required on the inside of the structural shell to minimize heat loss through the wall and to keep the structural members relatively cool. Thus, insulation serves both to improve transport system performance and allow the use of less costly metals for the structural shell. Alumina silica insulation was chosen for its high-temperature capabilities. One foot of alumina silica reduces heat loss to 0.39 MWt or a 0.78% loss rate. Downcomer design and thermal performance is summarized in Table 10.1.

An internal liner hangs inside the insulation and protects it from the fast flowing air stream. The liner is a thin, non-pressure-bearing mesh made

TABLE 10.1. Downcomer Design and Thermal Performance

Length	200 ft
Inside Diameter	15 ft
Insulation Thickness	1 ft
Inlet Air Temperature	2000 °F
Exit Air Temperature	1985 °F
Inside Wall Temperature	1900 °F
Outside Wall Temperature	150 °F
Heat Loss	0.39 MWt (0.78%)

from Inconel-617 or some similar high-nickel alloy. Five expansion joints are required over the 200-foot length of the tower. An expansion bellows is used for the structural shell, while the liner is fitted in several sections that can slide over each other.

10.2 AIR-TO-AIR HEAT EXCHANGER

Because currently available air movers cannot handle the combination of high temperature, flow rate, and pressure drop encountered in the volumetric receiver system, an air-to-air heat exchanger is required. A checker stove system or a recuperator were both considered. The checker stove system employs two vessels filled with "super duty" fireclay brick that are alternately charged and discharged on a cyclical basis. The recuperator is a continuous (non-cycling) air-to-air heat exchanger. Schematic flow diagrams of the two systems are shown in Figures 10.1 and 10.3. The principal advantage of the checker stove system is its ability to smooth out fluctuations in energy delivered from the receiver. The recuperator, while having no thermal buffering capabilities, is more simplistic and less expensive.

The design for the checker stoves is based on the methodology presented by Schofield et al. (1961). The design procedure is as follows:

1. Specify hot and cold inlet gas temperatures.
2. Select approach temperatures at hot and cold ends of the checker stove.
3. Calculate mean "gas" and "blast" temperatures.
4. Calculate "gas" and "blast" side heat transfer coefficients.

5. Calculate "unadjusted" overall heat transfer coefficient.
6. Adjust overall heat transfer coefficient for:
    a) transients associated with changeover from "gas" to "blast."
    b) end effects; the mean ΔT between the "gas" and "blast" sides is not fixed.
7. Solve for the total heat transfer area.
8. Calculate overall stove dimensions.
9. Check pressure drop through the stove.

The design conditions for the checker stove are presented in Table 10.2 and the resulting design is summarized in Table 10.3. Sizes, costs, and performance

TABLE 10.2. Checker Stove Design Conditions

Checker Type	Basket Weave
Checker Thickness	1.25 inches
Channel Flow Path	2 inches x 2 inches
Checker Material	"Super duty" fireclay
Cycle Time	1 hr "gas"; 1 hr "blast"
Gas-Blast Mean Temperature Difference	200°F
Inlet "gas" Temperature	2000°F
Exit "blast" Temperature	1800°F
Inlet "blast" Temperature	Depends on air mover pressure ratio; ~70°F
Exit "gas" Temperature	Inlet "blast" + 200°F
Air Velocity at Standard Conditions	4.5 ft/sec
Inlet Mass Flow Rate	93.3 lbm/s

TABLE 10.3. Checker Stove Design

Surface Area	3.65×10^5 ft^2
Stove Volume	8.04×10^4 ft^3
Brick Volume	3.06×10^4 ft^3
Stove Diameter	30 ft
Stove Length	116 ft
Pressure Drop	0.03 psi

data were acquired for the recuperator from equipment manufacturers. The recuperator was designed to yield the same heat transfer effectiveness as the checker stove system, i.e., yield a product stream temperature of 1800°F with an overall effectiveness of 90%.

10.3 AIR MOVER

The transport system air mover could be either a fan, blower, or compressor, depending on the system pressure loss. The ability of fans, blowers, and compressors to handle different pressure heads and pressure ratios overlaps. Fans are generally applicable to pressures less than 0.5 psi; compressors are applicable at pressure differentials greater than 0.5 psi; and blowers overlap into both ranges. The "hot" side air mover must overcome frictional losses in the receiver, downcomer, checker stove or recuperator, valving, and piping. The "cold" side air mover must overcome frictional losses in the checker stove or recuperator plus valving and piping. The "cold" side air mover has not been sized to include frictional losses in transport equipment beyond the checker stove or recuperator. Transport equipment beyond the vicinity of the bottom of the tower was excluded from consideration in this analysis.

A unique set of "hot" and "cold" side air movers was specified for the transport system depending on whether a checker stove or recuperator was used. A difference in the pressure drop across these two pieces of equipment necessitates the difference in air movers. The total pressure differential for both "hot" and "cold" side fans is specified in Table 10.4 for transport systems with either checker stoves or recuperators. Fan design and performance data are given in Table 10.5.

TABLE 10.4. Transport System Pressure Loss
(Pressure Loss in psi)

Loss Component	Checker Stove System		Recuperator System	
	"hot" fan	"cold" fan	"hot" fan	"cold" fan
Receiver	1.0	-	1.0	-
Downcomer	0.03	-	0.03	-
Air-to-Air Heat Exchanger	0.03	0.03	0.05	0.90
Valving and Piping	0.03	0.03	-	-

TABLE 10.5. Fan Design and Performance Specifications

Characteristic	Checker Stove System		Recuperator System	
	"hot" fan	"cold" fan	"hot" fan	"cold" fan
Inlet Temperature	270°F	70°F	285°F	70°F
Static Pressure	30.5" H_2O	1.6" H_2O	30" H_2O	25" H_2O
ACFM	102,785	74,620	104,755	74,620
Efficiency	70%	65%	70%	70%
Hp	705	28	705	419

11.0. COST ANALYSIS

The objective of the cost analysis task was to provide design guidance in developing a cost-effective receiver. Meeting this objective required consideration of the total system cost and resultant levelized energy cost in addition to estimating the cost of the receiver. Therefore, cost analysis subtasks included balance of system costs and system economics, as well as receiver costs.

The receiver was evaluated at a much greater level of detail than any of the other components. Receiver costs were estimated via a materials-take-off approach based on the designs developed during the project. Costs for balance of system components (heliostats, land, tower, transport, BOP, O&M) were based on data in previous solar thermal reports or, in the case of the transport system, based on more cursory designs developed during this study. Inputs to the levelized cost analysis, and the methodology itself, were taken from De Laquil et al. (1983). More specific information regarding the costing approach and results is presented in the following subsections.

11.1 RECEIVER COSTS

The total installed capital cost of the receiver was estimated from the designs developed during the study. The designs were broken down into individual components from which material, fabrication, and installation requirements were identified. The approach was intentionally patterned after that used by Bird et al. (1982) so that costs estimated in this study would be more readily comparable to costs for earlier configurations of the volumetric receiver. One difference in approach was the development of capital cost estimating equations that were functions of critical receiver design variables, rather than making individual cost estimates for a specific design. In this way, tradeoffs in design affecting cost and performance could more easily be evaluated.

The cost estimates presented in this report contain uncertainty that should not be ignored. The rapid evolution of the volumetric receiver design over the course of the study precluded the opportunity for developing detailed mechanical designs from which more precise estimates could be made. The

limitations in design detail automatically limit the precision possible for a cost estimate. In addition to cost uncertainties related to lack of design detail, uncertainty also exists because of the uniqueness of the volumetric receiver. The use of innovative materials in innovative applications adds to the uncertainty that would exist for a "bare bones" estimate of a conventional structure. In summary, the cost estimates should be used for preliminary, "ball park" comparisons only.

The installed cost includes charges for materials, manufacturing and fabrication, transportation, field assembly, and installation plus indirects. All costs are estimated in 1983 dollars for "overnight construction"; i.e., an allowance for interest or escalation during construction is not included. Charges are also not included for construction contingency or future expenditures for research and development required to bring the volumetric receiver to commercialization. Each of the cost components for the shrouded, pre-swirl receiver is identified in Table 11.1 along with its cost controlling variables, where applicable. Auxiliaries consist of receiver instrumentation and control, lightning protection, and a light-duty crane for periodic maintenance.

Material requirements were estimated directly from dimensions specified in the designs developed during the study. Labor requirements were based on the nature of the component and the degree of fabrication and assembly required to transform purchased materials into the components as designed. Fabrication, assembly, and installation activities are summarized in Table 11.2 for each of the principal components. Actual man-hours were estimated from productivity figures in industry production manuals such as Page and Nation (1976), Winslow (1972), and Wood (1971). Both material and labor requirements were estimated as a function of the design variables identified in Table 11.1. Quantity requirements for materials and labor were then converted into costs by multiplying by the appropriate unit cost for each material and labor type. Unit costs for the materials and labor used in construction of the volumetric receiver are shown in Table 11.3. Cost data were acquired from vendors, cost estimating manuals, periodicals, and in-house sources. The two field labor rates are "fully burdened" and include general contractor's overhead and

TABLE 11.1. Volumetric Receiver Components

Component	Cost Controlling Variables
Fibers	Fiber diameters, packing density, absorbing zone inside and outside radii, receiver height
Absorbing wedges	Wedge width, depth, and spacing; receiver height; downcomer radius
Orifice plate	Downcomer radius; receiver height; wedge spacing and width
Insulation	Receiver outside radius, absorbing zone inside radius, receiver height, shroud height
Spillage shields	Receiver outside radius; absorbing zone outside radius, receiver height, shroud height
Exterior skin	Receiver outside radius
Interior skin	Receiver height, shroud height, receiver outside radius, absorbing zone inside radius
Structural steel	Receiver weight
Pre-Swirl piping	Receiver outside radius, downcomer radius, receiver height
Pre-Swirl blower	Fixed
Shroud packing racks	Receiver outside radius, absorbing zone outside radius, receiver height; shroud height
Shroud packing	Shroud packing heat transfer area
Auxiliaries	Fixed
Transportation	Receiver weight
Misc. labor & materials	5% of direct material & labor
Indirects	10% of direct costs

TABLE 11.2. Fabrication, Assembly, and Installation Activities

Fibers	1) Cut to length and fuse both ends. 2) Drill holes through insulation at top and bottom of the absorbing zone. 3) Attach fibers at top and bottom. 4) Lift fibers to tower top.
Absorbing Wedge	1) Cut full-length notches for orifice plate on both sides of wedge. 2) Lift to tower top. 3) Erect and fasten.
Orifice Plate	1) Drill holes in plate. 2) Lift to tower top. 3) Slide into wedge notches.
Insulation	1) Lift to tower top. 2) Attach to insulation anchors on inside walls, ceiling, and floors (3 layers).
Spillage Shields	1) Lift to tower top. 2) Attach to anchors on outside of receiver in exposed areas.
Exterior Skin	1) Cut sheet to size. 2) Lift to tower top. 3) Handle and erect.
Interior Skin	1) Cut sheet to size. 2) Attach insulation anchors. 3) Attach fiber hooks. 4) Lift to tower top. 5) Handle and erect.
Structural Steel	1) Cut to size. 2) Lift to tower top. 3) Handle and erect.
Pre-Swirl Piping	1) Cut main, lateral, and jet piping to length. 2) Cut slots in jet piping. 3) Cut holes in laterals and main. 4) Lift piping to tower top. 5) Handle and erect piping. 6) Weld piping together.
Pre-Swirl Blower	1) Lift to tower top. 2) Handle and erect.
Shroud Packing Racks	1) Cut rack material from steel plate 2) Bend bars into racks. 3) Drill bolt holes in rack and interior skin. 4) Bolt rack to ceiling 5) Weld bracer bar to bottom of rack row.
Shroud Packing	1) Lift to tower top. 2) Lay packing into racks.

TABLE 11.3. Receiver Material and Labor Unit Costs

Item	Mid-1983 Unit Cost
Tower top labor	$33/hr
Field labor	$31/hr
Shop labor	$31/hr + 0.13 (materials cost)
Aluminum siding	$1.15/ft^2
Alumina silicate insulation	$14.30/ft^3
Calcium silicate insulation	$12.50/ft^3
Fiberglass insulation	$1.50/ft^3
Carbon steel plate	$0.30/lb
Carbon steel structural shapes	$0.40/lb
Carbon steel pipe, D < 24 in.	$0.40/lb
Carbon steel pipe, D > 24 in.	$0.50/lb
Stainless steel 316 plate	$2.70/lb
Stainless steel 316 pipe	$4.00/lb
Inconel 601 plate	$5.00/lb
Inconel 601 pipe	$9.00/lb
Inconel 612 plate	$11.00/lb
Inconel 617 pipe	$19.00/lb
Hastelloy x plate	$11.00/lb
Hastelloy x pipe	$19.00/lb
Silicon carbide wedges	$16/ft. + $10/lb
Ceramic fiber	$43/lb

profit as well as the employees' pay and fringe benefits. The differential among the two field rates reflects the extra difficulty of working at the tower top. The shop labor rate covers all business charges such as capital, O&M, and profit as well as employees' pay and fringes. Although the shop charge (including material markup) is more expensive per hour than field labor, productivity is much better in the shop.

Costs were estimated for a shrouded, preswirl receiver both with and without shroud packing in the preswirl zone. The design dimensions applicable for both receivers are given in Table 11.4. The shroud packing variables may be

TABLE 11.4. Volumetric Receiver Design Dimensions

Variable Name	Value
Downcomer Radius	6.28 ft
Inside radius of absorbing zone	7.55 ft
Outside radius of absorbing zone	16.41 ft
Outside radius of shroud cavity	36.09 ft
Height of absorbing zone	32.81 ft
Fiber packing density	106 fibers/ft^2
Fiber diameter	0.00197 ft
Orifice hole density	63 holes/ft^2
Shroud packing heat transfer area	76,700 ft^2
Shroud packing diameter	0.0164 ft
Absorbing wedge width	0.656 ft
Absorbing wedge thickness	0.410 ft
Absorbing wedge spacing	0.410 ft
Height of shroud opening	19.69 ft

ignored for the base case version of the receiver. A summary of costs by component is presented in Tables 11.5 and 11.6 for the two receivers.

The dominant cost components common to both designs are the fibers, absorbing wedges, orifice plates, and insulation. The preswirl piping is relatively important for the base case receiver, while the shroud packing becomes the secondmost costly component for the alternate design. The labor-intensive nature of the fibers stems from the cost of placing attachment points to the floor and ceiling for the thousands of fibers and then attaching the fibers themselves. The absorbing wedges are constructed of silicon carbide, as are the orifice plates. The drilling of holes through silicon carbide makes the orifice plates expensive, while the cost of the wedges is largely attributable to their bulk.

Shroud packing is designed to increase the heat transfer area and rate of heat transfer to the air in the preswirl zone. This not only increases the thermal performance of the receiver but also lowers the temperature of the outer zones to the point where carbon steel preswirl piping can be used rather

TABLE 11.5. Shrouded Preswirl Base Case Receiver Costs

Component	Material	Labor
Fibers	$ 24,000	$1,750,000
Absorbing wedges	770,000	140,000
Orifice plate	71,000	720,000
Insulation	195,000	460,000
Spillage shields	39,000	140,000
Exterior skin	3,000	3,000
Interior skin	18,000	15,000
Structural steel	5,000	4,000
Preswirl piping	290,000	240,000
Preswirl blower	45,000	45,000
Total direct M&L[(a)]	$1,460,000	$3,517,000
Auxiliaries		$250,000
Transportation		34,000
Misc. M&L[(a)]		249,000
Indirects		551,000
Total		$6,061,000
Rounded Total		$6,100,000

(a) Materials and Labor

than stainless steel. It should be noted that neither of the two cases represent cost-optimized designs. Specifically, the material cost for the shroud packing could be reduced substantially if a cheaper (non-ceramic) or more efficient (in terms of surface area/volume ratio) fiber were used. Cost estimates for either receiver would be subject to change as design uncertainties are clarified.

TABLE 11.6. Shrouded Preswirl Receiver Costs with Shroud Packing

Component	Material	Labor
Fibers	$ 24,000	$1,750,000
Absorbing wedges	770,000	140,000
Orifice plate	71,000	720,000
Insulation	195,000	460,000
Spillage shields	39,000	140,000
Exterior skin	3,000	3,000
Interior skin	18,000	15,000
Structural steel	5,000	4,000
Preswirl piping	29,000	130,000
Preswirl blower	45,000	45,000
Shroud packing racks	(a)	4,000
Shroud packing	940,000	80,000
Total direct M&L(b)	$2,139,000	$3,491,000

Auxiliaries	$250,000
Transportation	35,000
Misc M&L(b)	282,000
Indirects	620,000
Total	$6,817,000
Rounded Total	$6,800,000

(a) < $500
(b) Materials and Labor

11.2 BALANCE-OF-SYSTEM COSTS

In addition to the receiver, other solar plant cost components are heliostats, land, tower, downcomer, air mover, air-to-air heat exchanger, and the balance-of-plant. All of these components must be included to calculate a levelized energy cost (LEC). The cost estimating objective for the balance-of-system components is to allow determination of system impacts from changes in individual components. This requires balance-of-system estimates that are credible, but that need not be extremely accurate or detailed. Where possible,

system component estimates available from the literature were used in this study. Other components, such as the transport system, were estimated from more cursory design information than that available for the receiver. In general, the balance-of-system components were treated as functions of one or two variables rather than a host of variables, as was the case for the receiver.

Another objective of the system cost estimating and levelized energy calculations (see Section 11.3) was to allow an equitable comparison of the current estimated system costs with those estimated in De Laquil et al. (1983). Cost data for heliostats, land, tower, and balance-of-plant components were taken directly from De Laquil et al. (1983). Transport system costs were estimated independently.

An identical heliostat unit cost of $\$110/m^2$ (1981 dollars) was used for each of the systems analyzed. Differences in the total heliostat costs are attributable to differences in the expected performance of alternative receiver designs. Land costs were assumed to be proportional to heliostat area, while tower and balance of plant costs were set equal for all systems.

Transport system costs were based on designs developed in this study and described in Section 10. Design and cost data from Gibbs and Hill (1981), Boeing, and De Laquil et al. (1983) were considered in estimating the downcomer costs. Downcomer costs are summarized by component in Table 11.7.

TABLE 11.7. Volumetric Receiver Downcomer Cost

Component	Installed Cost
Structural steel	$480,000
Insulation	190,000
Liner	750,000
Expansion joints	520,000
	$2,040,000

Costs for the air-to-air heat exchangers were obtained from vendors and based on the designs discussed in Section 10.3. Checker stove costs were obtained from three vendors. Two vendors supplied cost estimates for the recuperator. The checker stove proved to be quite expensive ($10.5 million 1981 dollars) and nearly double the cost of the recuperator ($5.7 million 1981 dollars).

Both "hot and "cold" side fans were required for the checker stove and recuperator transport systems. The design conditions for these fans are given in Table 10.2. Fan costs were estimated from data in Guthrie (1974), Page and Nation (1976), and Richardson Engineering Services (1983) and are summarized in Table 11.8.

Capital costs were estimated for five different systems to allow comparisons of the impact of different receiver and transport designs. The systems include 1) the volumetric receiver design analyzed by De Laquil et al. (1983), 2) the base case shrouded, preswirl receiver with checker stove transport, 3) the base case with shroud packing in the receiver, 4) the base case with recuperator transport, and 5) the base case with no cost for an air-to-air heat exchanger included. This last case would be meaningful if the hot air application could be located at the base of the tower, with the air mover downstream of the application. The total direct capital costs for these systems are itemized by component in Table 11.9.

TABLE 11.8. Transport System Fan Costs (1981 dollars)

	"Hot" Fan	"Cold" Fan
Checker stove system	$100,000	$30,000
Recuperator system	$100,000	$60,000

TABLE 11.9. Volumetric Receiver System Capital Cost (millions of 1981 dollars)

Components	System Descriptions				
	Sandia/ De Laquil	Shroud Base	Base w/ Shroud Packing	Base w/ Recuperator	Base w/ No HX[a]
Heliostats	10.3	12.0	11.3	12.0	12.0
Land	1.2	1.4	1.3	1.4	1.4
Tower	0.5	0.5	0.5	0.5	0.5
Receiver	5.8	5.8	6.5	5.8	5.8
Downcomer	2.0	2.0	2.0	2.0	2.0
Air mover(s)	1.8	0.1	0.1	0.2	0.1
Air-to-air HX	3.3	10.5	10.5	5.7	--
Balance of plant	2.4	2.4	2.4	2.4	2.4
Total	27.3	34.7	34.6	30.0	34.2

(a) Base case with no air-to-air heat exchanger (HX) included.

11.3 SYSTEM ECONOMICS

A levelized energy cost (LEC) was calculated for each of the systems described in Section 11.2. The levelized energy cost allows a relative ranking of the attractiveness of the systems by encompassing capital costs, O&M costs, and system performance into a single figure of merit. The approach taken was to use the methodology and inputs employed by De Laquil et al. (1983) so that costs estimated for the systems developed in this study would be comparable to costs estimated in the De Laquil report.

A thorough review of the LEC methodology and inputs described by De Laquil et al. (1983) and the user's manual for DELSOL2 (Dellin 1981) did not yield a methodology that exactly duplicated the LECs calculated by De Laquil et al. The approach was modified to include a recalculation of the LEC for the volumetric receiver as envisioned by De Laquil et al. Thus, the LECs presented in this section are comparable among themselves, but not directly comparable to the figures presented by De Laquil et al.

The principal economic assumptions used in the analysis are presented in Table 11.10. In addition to the direct capital costs tabulated in Table 11.9, indirects, contingency, and spare parts add 28% which is further compounded by 5% for interest during construction. Table 11.11 summarizes the system capital and levelized energy costs for the five volumetric receiver systems analyzed.

Differences in the system LEC are primarily attributable to differences in the type of air-to-air heat exchanger. The capital cost figures of Table 11.9 identify the air-to-air heat exchanger as one of the top three capital cost components and the component which changes the most from system to system. The air mover cost and electricity charges are higher for the system described by De Laquil et al. (1983) because the air mover was sized for a pressure drop of ~7.4 psi compared to approximately 1.1 psi for the other systems. Heliostat costs are inversely proportional to receiver performance, as one might expect, and land costs parallel the heliostat costs.

TABLE 11.10. Principal Economic Assumptions

1st year of commercial operation	1990
Price year for cost information	1981
System operating lifetime	20
General rate of inflation	0.08
Capital escalation rate	0.08
Electric escalation rate	0.09
Discount rate	0.138
Capital recovery factor	0.149
Fixed charged rate	0.229

TABLE 11.11. System Capital and Levelized Energy Costs[a]

	System Descriptions				
	Sandia/ De Laquil	Shroud Base	Base w/ Shroud Packing	Base w/ Recuperator	Base w/ No HX[b]
Direct cost	27.3	34.7	34.6	30.0	24.2
Indirects, contingencies, spares, and IDC	36.7	46.6	46.5	40.3	32.5
1st yr. power charges	190,000	56,000	56,000	86,000	56,000
Levelized capital	8.40	10.68	10.65	9.23	7.45
Levelized O&M[c]	0.99	1.26	1.26	1.09	0.88
Levelized elec.	0.37	0.11	0.11	0.17	0.11
Annual power output, 10^6 kWht	122.2	122.2	122.2	122.2	122.2
LEC, $/kWht	0.080	0.099	0.098	0.086	0.069
LEC, $/MBtu	23.40	28.89	28.82	25.15	20.24

(a) All costs in millions of 1981 dollars except for first year power charges and levelized energy costs
(b) Base case with no air-to-air heat exchange (HX) included.
(c) Operation and Maintenance.

12.0 REFERENCES

Bejan, A., and D. Poulikokos, V. 1980. "Fin Geometry for Minimum Entropy Generation in Forced Convection." Journal of Heat Transfer. 104:616-623.

Bird, S. P., et al. 1982. Evaluation of Solar Air Heating Central Receiver Concepts. PNL-4003, Pacific Northwest Laboratory, Richland, Washington.

Corlett, R. C. 1966. "Direct Monte Carlo Calculations of Radiative Heat Transfer in Vaccum." Journal of Heat Transfer. 88(4):376-382.

Cur, N., and E. M. Sparrow. 1979. "Measurements of Developing and Fully Developed Heat Transfer Coefficients along a Periodically Interrupted Surface." Journal of Heat Transfer. 101:271.

De Laquil, P., III, C. L. Young and J. E. Noring. 1983. Solar Central Receiver High Temperature Process Air Systems. SAND82-8254, Sandia National Laboratories, Livermore, California.

Dellin, T. A., M. J. Fish and C. L. Young. 1981. A User's Manual for DELSOL2. SAND81-8237. Sandia National Laboratory, Livermore, California.

Drost, M. K. 1984. Volumetric Receiver Development. Ph.D. Thesis, Department of Mechanical Engineering, Oregon State University.

Drost, M. K., and L. L. Eyler. 1981. Preliminary Evaluation of the Volumetric Air Heating Receiver. Paper No. 81-WA/Sol-26, American Society of Mechanical Engineers Winter Annual Meeting, Washington D.C., November 1981.

Emery, A. F., C. J. Kippenhan, H. Mortazavi and R. Weiting. 1981. Computation of Radiation View Factors for Surfaces with Obstructed Views of Each Other. Paper No. 81-HT-57, In Proceedings from the 20th Joint ASME-AIChe National Heat Transfer Conference, Wisconsin, August 1981.

Gibbs and Hill. 1981. System Requirements for a Solar Central Receiver System Integrated with a Cogenerative Facility for Copper Smelting. Gibbs and Hill, Inc., New York, New York.

Guthrie, K. M. 1974. Process Plant Estimating, Evaluation, and Control. Craftsman Book Company, Solana Beach, California.

Halbleib, J. A. 1979. ACCEPT: A Three-Dimensional Electron/Photon Monte Carlo Transport Code Using Combinational Geometry. SAND79-0415, Sandia National Laboratories, Alburquerque, New Mexico.

Howell, J. R. 1968. "Monte Carlo Applications in Heat Transfer." In Advances in Heat Transfer. Vol. 5.

Howell, J. R., and R. R. Bannerot. 1974. The Evaluation of Surface Geometry Modification to Improve the Performance of Solar Energy Collectors. NSF/RANN/SE/GI-41003/TR/74/1. National Science Foundation.

Kays, W. M., and M. E. Crawford. 1980. Convective Heat and Mass Transfer, 2nd ed., McGraw-Hill, pp. 134-139.

King, D. L. 1982. Beam Quality and Tracking Accuracy Evaluation of Second-Generation and Barstow Production Heliostats. SAND82-0181, Sandia National Laboratories, Alburquerque, New Mexico.

Lee, C. P., and W. J. Yang. 1978. "Augmentation of Convective Heat Transfer from High-Porosity Perforated Surfaces." Heat Transfer. Toronto, 2:589.

Liang, C. Y., and W. J. Yang. 1975. "Heat Transfer and Friction Loss Performance of Perforated Heat Exchanger Surfaces." Journal of Heat Transfer. 95(1):9.

Los Alamos Scientific Laboratories. 1978. MCNP: A General Monte Carlo Code for Neutron and Photon Transport. Los Alamos Scientific Laboratory, NW(USA), July 1978.

Mishkin, M. and Kowalski, G. J. 1983. Application of Monte Carlo Techniques to Steady-State Radiative and Conductive Heat Transfer Problems Through a Participitating Medium. ASME Paper No. 83-WA/HT-27. American Society of Mechanical Engineers.

Modest, M. F. 1978. "Three Dimensional Radiative Exchange Factor for Non-Gray, Non-Diffuse Surfaces." Numerical Heat Transfer. 1:403-416.

Morgan, V. T. 1973. "The Heat Transfer from Bare Stranded Conductors by Natural and Forced Convection in Air." International Journal of Heat and Mass Transfer. 16:2023-2034.

Morgan, V. T. 1975. "The Overall Convection Heat Transfer from Smooth Circular Cylinders." In Advances in Heat Transfer. 8:199-264.

Page, J. S., and J. G. Nation. 1976. Estimator's Piping Man Hour Manual. 3rd ed, Gulf Publishing Company, Book Division, Houston, Texas.

Richardson Engineering Services. 1983. Process Plant Construction Estimating Standards. Richardson Engineering Services, Inc. San Marcos, California.

Schofield, J., P. Butterfield, and P. A. Young. 1961. "Hot Blast Stoves." J. of the Iron and Steel Institute. November, 1961.

Siegel, R. and J. R. Howell. 1972. Thermal Radiation Heat Transfer. McGraw-Hill, New York, New York.

Shah, R. K. 1975. Perforated Heat Exchanger Surfaces, Part 2 - Heat Transfer and Flow Friction Characteristics. ASME Paper No. 75-WA/HT-9. American Society of Mechanical Engineers.

Siebers, D. L., R. G. Schwind and R. J. Moffat. 1983. Experimental Mixed Convection Heat Transfer from a Large Vertical Surface and Horizontal Flow. HMT-36, Stanford University, California.

Sparrow, E. M., B. R. Baliga, and S. V. Patankar. 1977. "Heat Transfer and Fluid Flow Analysis of Interrupted-Wall Channels, with Application to Heat Exchangers." Journal of Heat Transfer. 99:4.

Tanasawa, I., S. Nishio, K. Takano and M. Taco. 1983. "Enhancement of Forced Convection Heat Transfer in Rectangular Channel Using Turbulence Promoters." In Proceedings from the ASME-JSME Thermal Engineering Joint Conf. Vol. 1, Honolulu, Hawaii.

Toor, J. S. 1967. Radiant Heat Transfer Analysis Among Surfaces Having Direction Dependent Properties by the Monte Carlo Method. M.S. Thesis, Purdue University.

Toor, J. S., and R. Viskanta. 1968. "A Numerical Experiment of Radiation Heat Interchange by the Monte Carlo Method." Journal of Heat and Mass Transfer. 11:883-897.

Viskanta, R., et al. 1978. "Radiation Characteristics of Multiple-Plate Glass Systems." International Journal of Heat and Mass Transfer. 21:815-818.

Weiner,M. M., et al. 1965. Radiative Interchange Factors by Monte Carlo. ASME Paper No. 65-WA/HT-51. American Society of Mechanical Engineers.

Welty, J. R., C. E. Wicks, and R. E. Wilson. 1976. Fundamentals of Momentum, Heat and Mass Transfer. John Wiley and Sons, Inc., New York.

Wieting, A. R. 1975. "Empirical Correlations for Heat Transfer and Flow Friction Characteristics of Rectangular Offset-Fin Plate-Fin Heat Exchangers." Journal of Heat Transfer, 97(3):488-490.

Winslow, T. F. 1972. Construction Industry Production Manual. Craftsman Book Company, Solana Beach, California.

Wood, C. S. 1971. Mechanical Estimator's Handbook. Craftsman Book Company, Solana Beach, California.

Yang, W. J. 1983. "Forced Convective Heat Transfer in Interrupted Compact Surfaces." In Proceedings from the ASME-JSME Thermal Engineering Joint Conference, Vol. 3, Honolulu, Hawaii.

Yang, R. S. 1981. Heat Transfer Throughout a Randomly Packed Bed of Spheres by the Monte Carlo Method. Ph.D. Thesis, University of Texas.

APPENDIX

DETAILS OF THE MONTE CARLO MODEL

APPENDIX

DETAILS OF THE MONTE CARLO MODEL

A typical two-dimensional receiver geometric arrangement is shown in Figure A.1 (axial variations are neglected). The outer two rows consist of wedge-shaped reflecting pins and the inner surfaces consist of fin-shaped pins. The receiver is now divided into zones and each zone is divided into cells. The cell boundary is either the edge of a fin-shaped pin or the centerline of a wedge-shaped pin. The photon bundle enters one cell of the external row and bounces around between the cell boundaries until it exits the cell, moving into the next cell. Zone characteristics such as pin spacing, wedge angle, and offset affect the movement of a photon bundle and are described in Figure A.1.

The normal procedure is to identify a symmetric section of a receiver design. For symmetry, The boundaries of the section are assumed to be perfect specular reflecting surfaces. Figures A.2 and A.3 illustrate this symmetric arrangement for both insolation distribution calculations and exchange factor calculations. Any photon bundle that reaches the section boundary is reflected back into the receiver with a reflection angle equal to the incident angle. The use of a specular section boundary can be justified by symmetry: for each photon bundle that passes through the boundary exiting the computational section, one photon bundle will enter the computational section from an adjoining section.

With the computational section defined, the emitting cell surface is identified. This will either be an external cell boundary for a typical cell in the external row if insolation distribution is required, or the surfaces of a typical fiber or fin if exchange factors are required. (To simplify the analysis, cylindrical fibers were modeled as square pillars, where the dimension of the square was specified to provide equivalent surface areas. While this simplification eased the analysis, its implication on accuracy is not certain. Further analysis is needed to verify that its impact would be minor.)

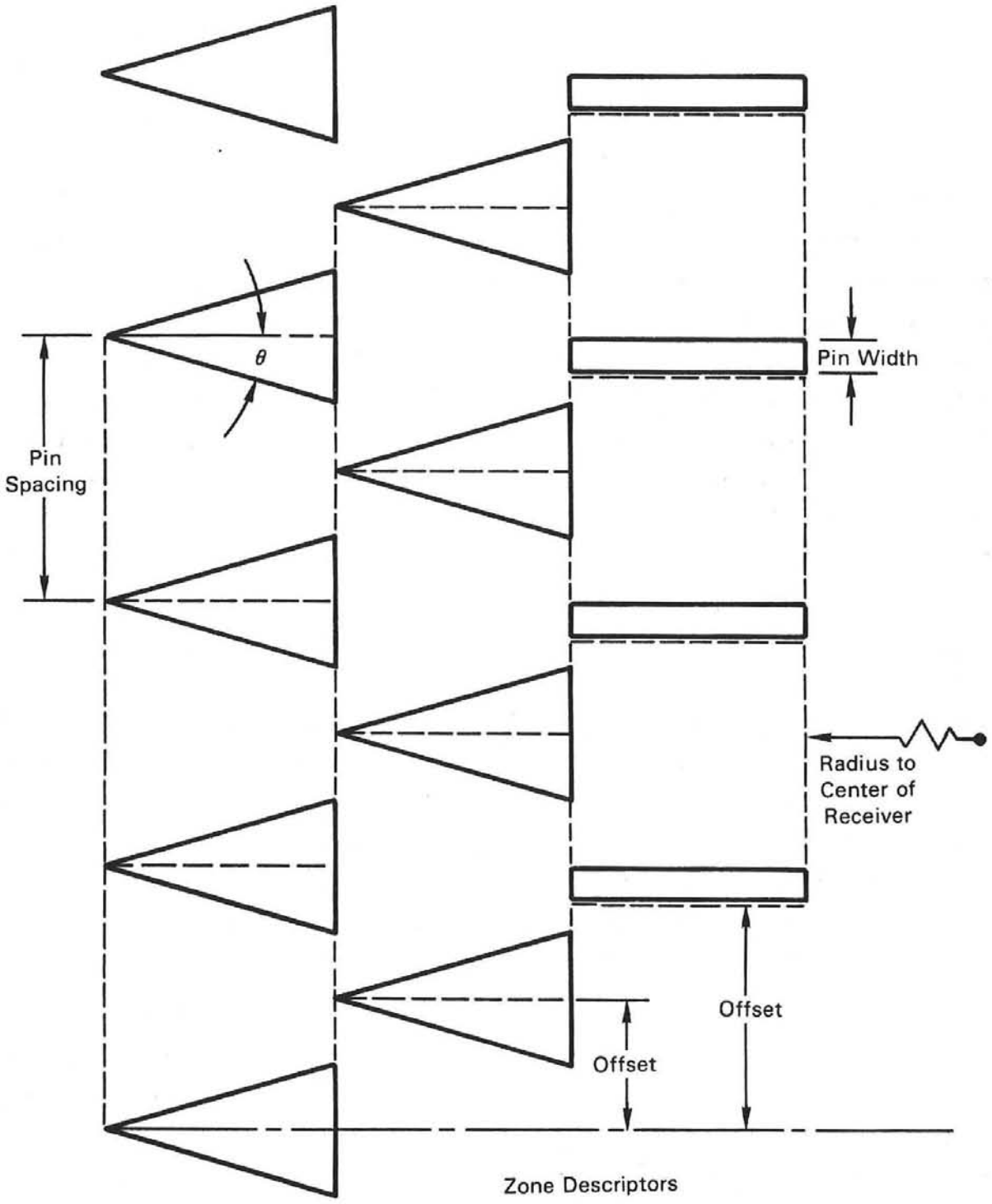

FIGURE A.1. Receiver Geometric Arrangement and Definition of Cell Parameters

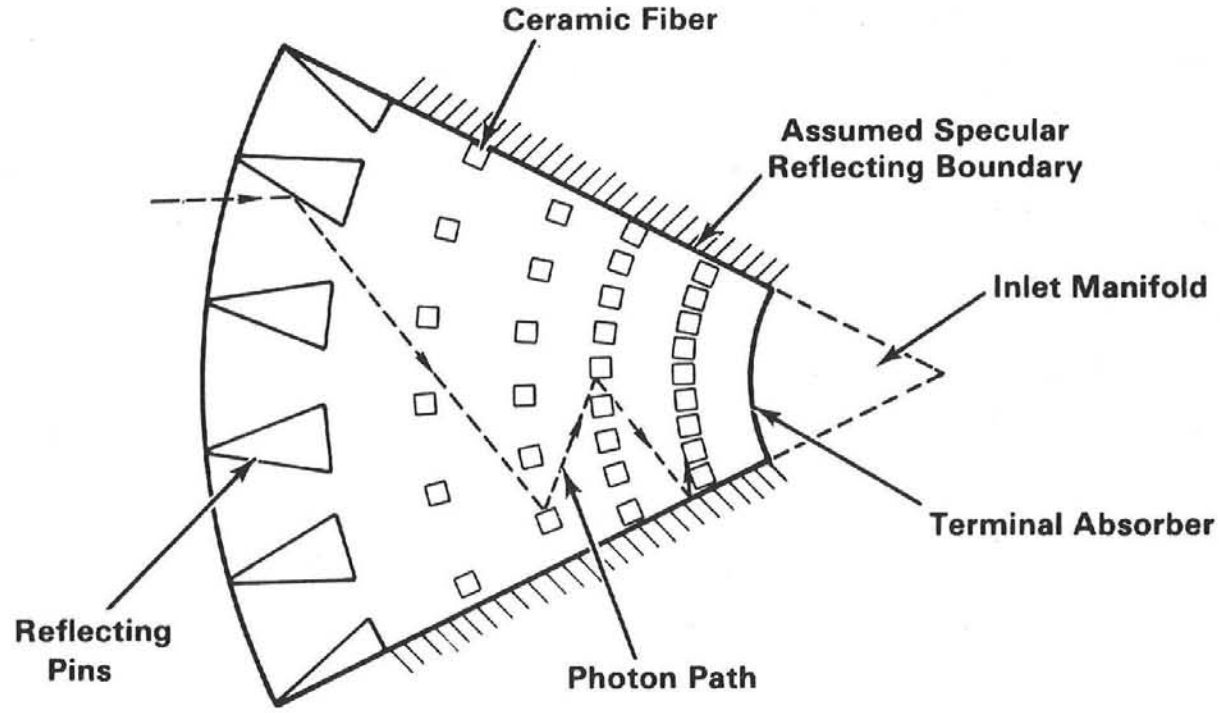

FIGURE A.2. Monte Carlo Model for Calculating Incident Radiation Absorption

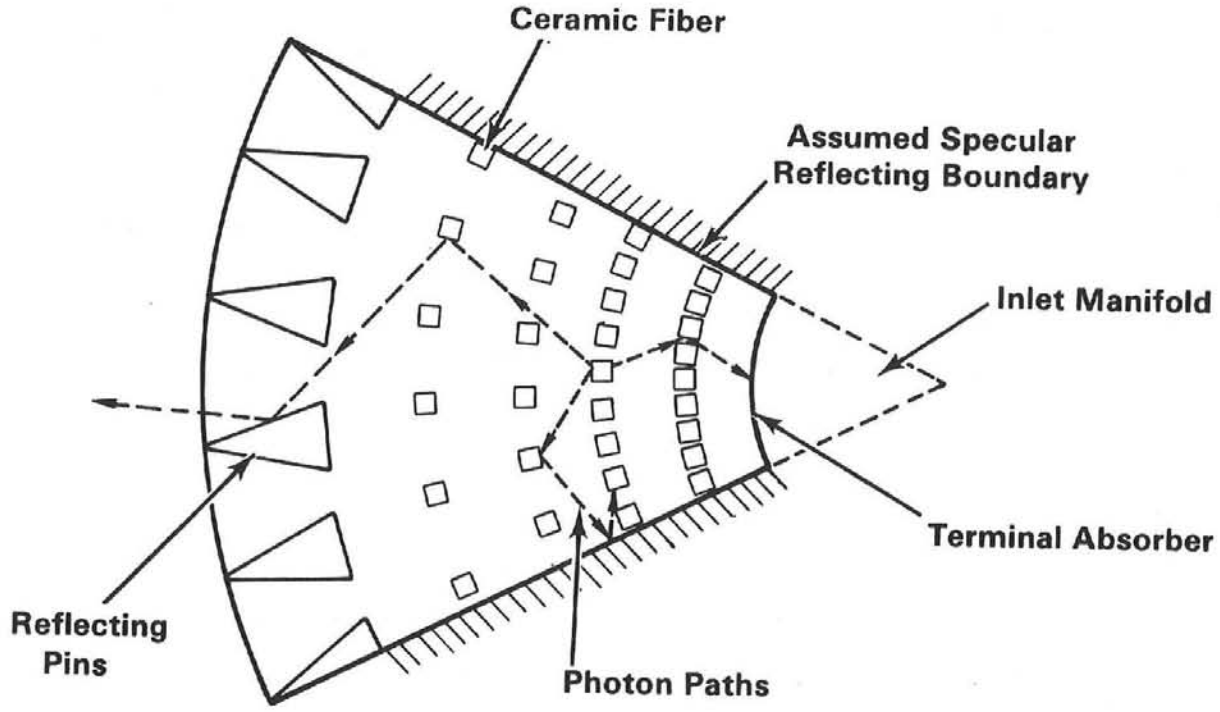

FIGURE A.3. Monte Carlo Model for Calculating Exchange Factors

In either case a large number of photon bundles are emitted from the surface of interest. The photon bundles are divided into NBATC batches, each of which contains NPHOT photons. After all the batches have been simulated, the mean and standard deviation of the NBATC results are calculated. The mean gives the nominal value for insolation distribution or exchange factor, and the standard deviation gives an indication of the statistical uncertainty in the mean value.

The Monte Carlo procedure can now be divided into three tasks: determination of the original location of photon emission, determination of the results of the interaction of a photon bundle and a cell, and calculation of cell-to-cell movement of a photon bundle.

PHOTON BUNDLE EMISSION

Photon bundles can be emitted at a variety of locations, depending on the required information. If the distribution of absorbed insolation is desired, then the photon bundles are originally emitted from the exterior cell boundary into an exterior cell. If the exchange factor is required from a surface, the photon bundles are emitted from the surface of interest. In either case the photon bundles are followed until either their energy drops below a minimum level or they exit the receiver. Figure A.2 presents the situation for calculation of insolation distribution, while Figure A.3 shows typical photon bundle histories for exchange factor calculations. Both figures show a typical fiber receiver layout with the fibers modeled as small rectangles with the same surface area as the cylindrical fiber. This section discusses photon bundle emission for insolation distribution calculation. Exchange factor calculations are discussed in Section 5.3 of the main report.

As discussed in Section 4.0, insolation will have an inlet angle distribution that is assumed to be Gaussian. The standard deviation of the insolation distribution can be calculated based on a heliostat image size and the radius of the receiver. The location of the point of emission is determined by dividing the emitting cell boundary into NICRM increments. For a total of NPHOT photon bundles, NPHOT/NICRM photons are emitted from the center of each increment. The emission angle is determined from (Yang 1981, p. 72)

$$\alpha = \sqrt{2}\ \sigma\ \text{erf}^{-1}\ (2R-1)$$

where α = emission angle

σ = standard deviation of incident angle distribution

R = random number from 0.0 to 1.0

erf^{-1} = inverse error function

This function insures that the distribution of a large number of emission angles will approximate a Gaussian distribution with a standard deviation of σ.

CELL/PHOTON INTERACTION

In this section the method of analyzing the path of one photon bundle through a computational cell is described. The algorithm for analyzing a single cell is applicable for a wide variety of cell shapes, but the approach used in the present analysis is limited to:

1. straight line cell boundary
2. $\theta > 0.0$ where θ is the cell boundary wedge half angle
3. θ right = θ left
4. Gray surfaces (optical properties are not wavelength dependent)
5. 2 dimensions (r,θ)
6. Regular fin or fiber spacing in a zone.

Once the emission point and angle are selected, one photon batch is emitted with an energy of 1.0, and the photon bundle history is determined until either the photon bundle leaves the cell or it is terminated because its energy drops below a minimum level. With the selection of the emission point, two angles are calculated: Beta-right and Beta-left (Figure A.4). If the emission angle is less than Beta-left, but greater than Beta-right, the photon bundle exits the cell through the opposing cell surface. If the emission angle exceeds Beta-left, the photon bundle strikes the left wall. A similar method was used by Howell and Bannerot (1974) in an evaluation of surface geometry modifications for the improvement of solar collectors.

Once the impacted surface has been determined, the location of the impact and the incident angle are determined by geometry. The appropriate equations are presented in Drost (1984). The energy of the photon is reduced by an

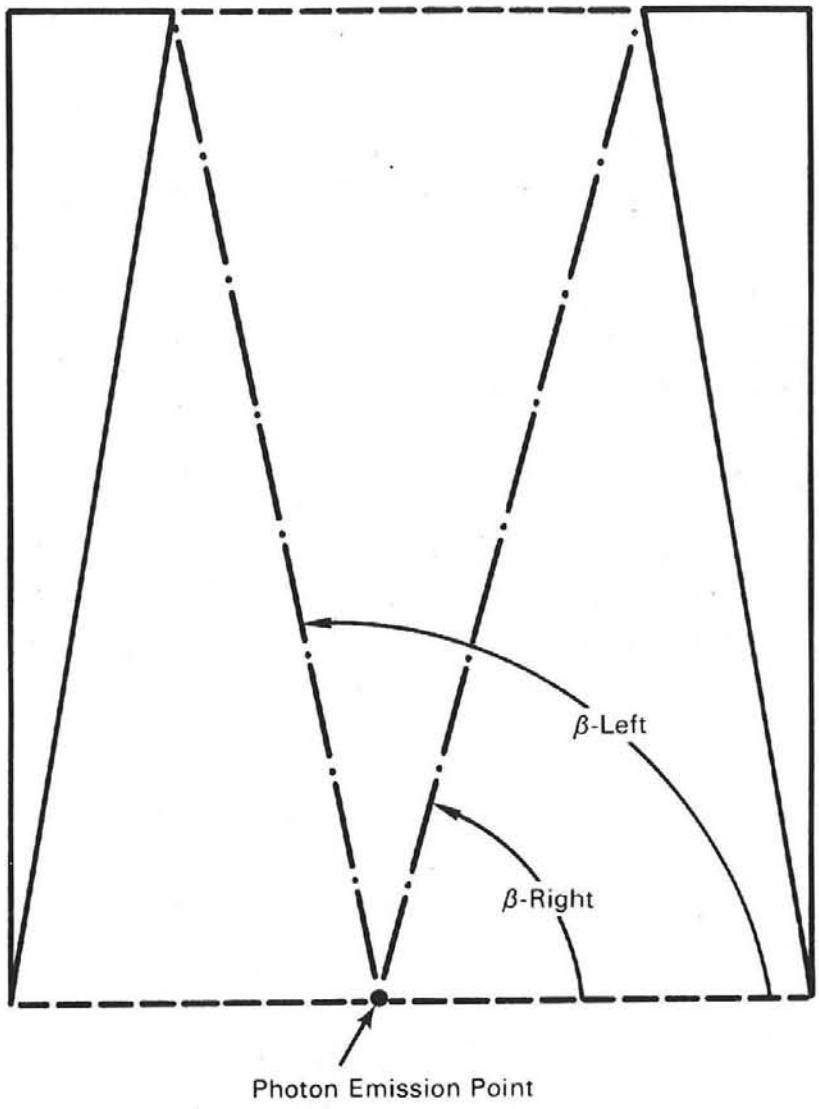

FIGURE A.4. Cell Angle Definitions

amount equal to the product of its current energy level and the surface emissivity. The energy given up by the photon bundle is absorbed by the impacted surface.

At this point, the process is repeated as the impacted surface becomes the emitting surface, and Beta-right and left are calculated based on the impact location. A random number is selected, and if that number is less than the surface specularity, the photon is reflected specularly (emission angle equals reflective angle). Otherwise the photon is reflected diffusely where the

emission angle (in radians) equals COS(-1 + 2R) where R is a random number between 0.0 and 1.0. With the new emission location and angle selected, the procedure is repeated until either the photon bundle energy drops below a minimum level or the photon bundle exits the cell. In either case the energy absorbed by each surface is recorded.

CELL-TO-CELL PHOTON TRANSPORT

Photon bundles are originally emitted into a cell located in the external row of pins (row 1). The procedure described in the last section is used to determine the photon history. If the photon history is not terminated because of absorption energy loss, the exiting surface, location, and angle are recorded. This information is used in a procedure which takes the exiting location, angle, and surface for the first cell and calculates an inlet location, angle, and surface for the next cell entered by the photon bundle. This process is repeated as the photon bundle moves from cell to cell through the receiver until the photon bundle either is terminated or exits the receiver (which is recorded as a reflection loss).

A row is described by the cell external pin spacing, the pin type (straight or wedge-shaped), pin thickness or wedge angle, offset, and radius of the row based on the centerline of the receiver. The offset indicates how the cells of one row are oriented relative to other rows. The significant parameters are shown in Figure A.1.

The location where an incoming bundle enters a cell is calculated from the exiting location of the adjacent donor cell. The total arc length from the datum to the exit location is calculated. This is used along with the appropriate dimension of the receiving cell to determine the inlet location. The inlet angle can be calculated directly from the outlet angle of the donor cell.

If the location calculation indicates that the photon bundle strikes a pin tip, a procedure similar to that described in Section 5.2 of the main report is followed. The photon bundle energy is reduced by an amount equal to the product of current photon bundle energy and the surface emissivity. If the current photon energy is still above the minimum level it will be reflected back into the donor cell. The entering location of the photon bundle will be the

same as the previous exiting location, but the angle of the photon bundle entering the original donor cell will depend on whether the pin is a specular or diffuse surface.

SURFACE PROPERTIES

It has been shown by previous investigators that direction-dependent properties can have a significant impact on radiation heat transfer (Toor, 1967). The volumetric receiver design is particularly sensitive to direction-dependent properties because many of the interactions take place at large incident angles. If the assumption of diffuse reflection is relaxed, it is necessary to provide information on the incident angle dependence of emissivity, reflectivity, absorptivity, and specularity. Modest (1978) makes the following assumptions concerning surface properties.

1. α'_λ, ε'_λ and ρ'_λ are independent of temperature
2. For solar radiation wavelengths (.1 μm < λ < 2.5 μm), spectral values for emissivity and absorptivity are correlated by

$$\varepsilon'_\lambda = \alpha'_\lambda = \varepsilon'_{\lambda,n}\left[1 - \left(\frac{2\beta}{\pi}\right)^8\right] + \left(\varepsilon'_{\lambda,msx} - \varepsilon'_{\lambda,n}\right) \exp\left[-\left(\frac{30\beta}{\pi} - 7\right)^2\right] \qquad (A.1)$$

3. For infrared wavelengths (λ > 2-5μm), spectral values for emissivity and absorptivity can be calculated from

$$\varepsilon'_\lambda = \alpha'_\lambda = \varepsilon'_{\lambda,n}\left[1 - \left(\frac{2\beta}{\pi}\right)^{10}\right] + \left(\varepsilon'_{\lambda,msx} - \varepsilon'_{\lambda,n}\right)\left(\frac{2\beta}{\pi}\right)^2\left[1 - \left(\frac{2\beta}{\pi}\right)^2\right] \qquad (A.2)$$

In addition, Modest suggests that the second term in Equation (A.1) can be omitted in order to decrease running time. He was concerned with metallic specular reflecting surfaces such as silver-teflon, which have the characteristic increase in emissivity with incident angle.

In this study, dielectric materials are predominant, suggesting that the second term in Equation (A.2) can be deleted. As a check on this assumption, a case with two reflecting rows was simulated using Equation (A.2) with and without the second term. The small variation in results was not significant; therefore the second term in Equation (A.2) was deleted. The VORRUM model,

which deals with insolation distribution, uses Equation (A.1). The VORVFM model, which deals with radiation exchange at infrared wavelengths, uses Equation (A.2).

Specularity is assumed to be independent of wavelength and incident angle. Reflectivity is assumed to consist of both a specular and a diffuse component.

REFERENCES

Drost, M. K. 1984. Volumetric Receiver Development. Ph.D. Thesis, Department of Mechanical Engineering, Oregon State University.

Howell, J. R., and R. R. Bannerot. 1974. The Evaluation of Surface Geometry Modification to Improve the Performance of Solar Energy Collectors. NSF/RANN/SE/GI-41003/TR/74/1, National Science Foundation.

Modest, M. F. 1978. "Three Dimensional Radiative Exchange Factor for Non-Gray, Non-Diffuse Surfaces." Numerical Heat Transfer. 1:403-416.

Yang, R. S. 1981. Heat Transfer Throughout a Randomly Packed Bed of Spheres by the Monte Carlo Method. Ph.D. Thesis, University of Texas.

UNLIMITED RELEASE
INITIAL DISTRIBUTION

U.S Department of Energy (7)
Forrestal Building
1000 Independence Avenue, S.W.
Washington, D.C. 20585
Attn: H. Coleman
C. Carwile
S. Gronich
C. Mangold
F. Morse
M. Scheve
F. Wilkins

U.S. Department of Energy (2)
1333 Broadway
Oakland, CA 94612
Attn: R. W. Hughey
M. Lopez

U. S. Department of Energy
Albuquerque Operations Office
P.O. Box 5800
Albuquerque, NM 87115
Attn: J. Weisiger

Arco Power Systems
9351 Deering
P. O. Box 2105
Chatsworth, CA 91313
Attn: F. A. Blake

Arco Power Systems
302 Nichols Drive
Hutchins, TX 75141
Attn: R. L. Henry

Arizona Public Service Company
P.O. Box 21666
Phoenix, AZ 85036
Attn: E. Weber

Arizona Solar Energy Commission
1700 W. Washington,Suite 502
Phoenix, AZ 85007
Attn: R. L. Sears

Babcock and Wilcox (3)
91 Stirling Avenue
Barberton, OH 44203
Attn: G. Grant
M. Seale
D. Smith

Battelle Pacific Northwest Laboratories (15)
P.O. Box 999
Richland, WA 99352
Attn: D. R. Brown
R. G. Cavola
D. E. DeBellis
M. K. Drost (10)
K. Drumheller
B. M. Johnson

Bechtel Group, Inc.
P.O. Box 3965
San Francisco, CA 94119
Attn: Dr. S. Fleming

Black and Veatch Consulting Engineers (2)
P.O. Box 8405
Kansas City, MO 64114
Attn: J. C. Grosskreutz
S. L. Levy

Boeing Aerospace Company
Energy Systems
P.O. Box 3999, MS87-63
Seattle, WA 98124
Attn: W. D. Beverly

Bureau of Reclamation
Code 1500E
Denver Federal Center
P.O. Box 25007
Denver, CO 80225
Attn: S. Hightower

California Energy Commission
1516 North St. M/S 40
Sacramento, CA 95814
Attn: A. Jenkins

Combustion Engineering, Inc.
1000 Prospect Hill Road
Windsor, CT 06095
Attn: C. R. Buzzuto

Department of Natural Resources
Energy Alternatives Administration
1302 State Office Building
Baltimore, MD 21201
Attn: R. S. Nietubicz

Department of Planning and Economic Development
P.O. Box 2359
Honolulu, HI 96804
Attn: E. Grabbe

Edison Electric Institute
1111 - 19th Street, N.W.
Washington, D.C. 20036
Attn: G. H. Lovin

El Paso Electric Company (2)
P.O. Box 982
El Paso, TX 79946
Attn. J. E. Brown
E. Wall

Electric Power Research Institute (3)
P.O. Box 10412
Palo Alto, CA 94303
Attn: J. Bigger
J. Cummings
E. DeMeo

Fluor Corporation
3333 Michelson Drive
Irvine, CA 92730
Attn: J. W. Mohlman

Foster Wheeler Development Corporation (2)
12 Peach Tree Hill Road
Livingston, NJ 07039
Attn: S. F. Wu
R. J. Zoschak

Garrett-AiResearch
402 S. 36th Street
Phoenix, AZ 85253
Attn: L. Six

G. A. Technologies
2021 K. Streen, N.W.
Washington, D.C. 20006
Attn: L. Green, Jr.

Georgia Institute of Technology (4)
Atlanta, GA 30332
Attn: C. Thomas Brown
D. H. Neale
N. Poulos
R. Williams

Gibbs and Hill, Inc. (2)
393 Seventh Avenue
New York, NY 10001
Attn: R. Prieto
G. Stern

Honeywell Energy Research Center
2600 Ridgway Parkway
Minneapolis, MN 55413

Institute of Gas Technology
IIT Center
3424 South State Street
Chicago, IL 60616
Attn: F. L. Kester

Jet Propulsion Laboratory
4800 Oak Grove Drive
Pasadena, CA 91103
Attn: M. Alper

Lawrence Berkeley National Laboratory (5)
University of California
Berkeley, CA 94720
Attn: R. Bailey
D. B. Evans
A. J. Hunt
M. Wahlig
R. Wolgast

Los Angeles Department of Water and Power
111 North Hope St.
Los Angeles, CA 90051
Attn: D. Chu

Martin Marietta Aerospace
P.O. Box 179, MS L0450
Denver, CO 80201
Attn: H. C. Wroton

McDonnell Douglas Astronatics Company (3)
5301 Bolsa Avenue
Huntington Beach, CA 92647
Attn: R. L. Gervais
J. Reatz
R. Riedesel

Modern Alloys, Inc. (4)
11172 Western Avenue
Stanton, CA 92669
Attn: J. E. Dressel
R. B. Grey
C. R. Mitchell
A. M. Peterson

National Bureau of Standards
Thermal Engineering Section
Washington, D.C. 20234
Attn: M. McCabe

New Mexico University
P.O. Box 3450
Las Cruces, NM 88003

Ohio Department of Energy
30 East Broad
Columbus, OH 43215
Attn: A. Rahim

Olin Chemical Co.
Metals Research Laboratory
91 Shelton Avenue
New Haven, CT 06511
Attn: E. F. Smith

Olin Chemical Company (2)
120 Long Ridge Road
Stamford, CT 06904
Attn: F. N. Christopher
L. C. Fioruccio

Pacific Gas and Electric Company
77 Beale Street
San Francisco, CA 94105
Attn: R. E. Price

Pacific Gas and Electric Company (2)
3400 Crow Canyon Road
San Ramon, CA 94526
Attn: C. Weinberg
G. Braun

The Ralph M. Parsons Company
100 West St.
Pasadena, CA 91124
Attn: N. W. Snyder

PFR Energy Systems, Inc.
P. O. Box 91890
Los Angeles, CA 90045
Attn: T. Rosenman

PRC Energy Analysis Company
7600 Old Springhouse Road
McLean, VA 22102
Attn: E. F. Shaver

Polydyne, Inc. (2)
1900 S. Norfolk St., Suite 209
San Mateo, CA 94403
Attn: P. B. Bos
J. M. Weingart

Rockwell International
Energy Systems Group
8900 De Soto Avenue
Canoga Park, CA 91304
Attn: T. Springer

Rockwell International
Rocketdyne Division
6633 Canoga Avenue
Canoga Park, CA 91304
Attn: J. M. Friefeld

San Diego Gas and Electric Company
Mechanical Engineering
P.O. Box 1831
San Diego, CA 92112
Attn: R. E. Potthoff

Solar Energy Industries Association
1140 19th St., N.W.
Suite 600
Washington, D.C. 20036
Attn: C. LaPorta

Solar Energy Research Institute (4)
1617 Cole Boulevard
Golden, CO 80401
Attn: B. Gupta
F. Krawiec
L. Murphy
J. Thorton

Southern California Edison
P.O. Box 325
Daggett, CA 92327
Attn: C. Lopez

Southern California Edison (2)
P.O. Box 800
Rosemead, CA 92807
Attn: J. N. Reeves
P. Skvarna

Standard Oil of California (2)
555 Market Street, Room 1104
San Francisco, CA 94119
Attn: S. G. Gibb
E. D. Lewis

Stanford University (3)
Department of Mechanical Engineering
Stanford, CA 94305
Attn: J. A. Erickson
J. P. Johnston
R. J. Moffat

Stearns Catalytic Corp.
P.O. Box 5888
Denver, CO 80217
Attn: W. R. Lang

United States Congress
Office of Technical Assessment
Washington, D.C. 20510
Attn: J. Furber

University of Houston (2)
Solar Energy Laboratory
3801 Cullen Blvd.
Houston, TX 77004
Attn: A. F. Hildebrandt
L. Vant-Hull

University of Illinois/EPRI
1206 W. Green Street
Urbana, IL 61820
Attn: A. M. Clausing

E. H. Beckner, 6000; Attn: V. Dugan, 6200
D. G. Schueler, 6220
J. V. Otts, 6222
E. C. Boes, 6226
J. A. Leonard, 6227

B. Granoff, 6254; Attn: J. D. Fish, 6254
D. C. Hawn, 6254
R. S. Claassen, 8000; Attn: D. M. Olson, 8100
A. N. Blackwell, 8200
D. L. Hartley, 8300
C. S. Selvage, 8000A
C. Hartwig, 8244
M. E. John, 8245
R. C. Wayne, 8400; Attn: L. D. Bertholf, 8430
H. Hanser, 8440

R. L. Rinne, 8470
A. C. Skinrood, 8471
J. C. Swearengen, 8473 (20)
R. L. Rinne, 8475 (Actg.)

Publications Division 8265, for TIC (30)
Publications Division 8265/Technical Library Processes Division, 3141
Technical Library Processes Division, 3141 (3)
M. A. Pound, 8024, for Central Technical Files (3)